DOCTOR OF PHILOSOPHY

The application of the ADCP variance method to turbulence measurements in a partially stratified estuary.

Williams, Eirwen

Award date:
2004

Awarding institution:
University of Wales, Bangor

The application of the ADCP variance method to turbulence measurements in a partially stratified estuary

A thesis submitted in accordance with the requirements of the University of Wales for the degree of Doctor of Philosophy

Eirwen Williams

University of Wales, Bangor

March 2004

Abstract

This thesis reports measurements of turbulent parameters based on the use of the variance method applied to the along beam velocities measured by an acoustic Doppler current profiler (ADCP). Estimates of Reynolds stress (τ), turbulent kinetic energy production rate (P) and eddy viscosity (N_z) are used to analyse the cycle of turbulence and its relationship to water column stratification in the partially stratified York River estuary, Virginia.

The estimates of Reynolds stress are validated by comparison with direct measurements from an acoustic Doppler velocimeter (ADV). The uncertainties in turbulence estimates using the variance method are analysed, as are improvements resulting from recent advances in ADCP technology which allow higher ping rates. For weak flows, the uncertainty in the measurements in τ and P arise mainly from instrument noise. For stronger flows, the principal determining parameter is the number of individual independent velocity measurements over which the variance is calculated. These results are validated by detailed statistical analyses of two data sets from a RDI 1200kHz Workhorse ADCP using different ping rates. While increasing ping rate generally reduces the effects of instrument noise, it does not alleviate the influence of flow related noise once the sampling interval is less than the autocovariance time scale of the turbulence.

The evolution of τ, P and N_z was observed over a spring-neap cycle, and the effect of tidal straining and stratification on these parameters is analysed for two shorter periods. At neaps, τ, P and N_z are significantly affected by the density structure: the highest values are restricted to a thin layer near the bed when the water column is stratified during the ebb, but high values propagate through the water column on the flood. At springs, increased stirring reduces stratification and results in a cycle of τ and P which resembles that observed in homogeneous conditions. Tidal straining has a marked influence on N_z: higher values occur on the flood with a mid-water column maximum; on the ebb, the maximum is much smaller and occurs nearer the bed.

In a test of the simplified dynamical balance of the York River estuary, τ is observed to covary with the other terms to give a first order balance, but there is a strong peak in τ at times of high flow speeds indicating the effect of higher order harmonics. The drag coefficient is estimated using a quadratic drag law, and the drag coefficient is found to increase significantly at higher current speeds.

Acknowledgements

Firstly, I would like to thank my supervisor, John Simpson, for all his help and patience in answering my questions, and for his willingness to share his extensive knowledge of oceanography.

I would also like to acknowledge the efforts of all the technical staff at the School of Ocean Sciences (SOS) at the University of Wales, Bangor who helped with various aspects of the data collection, including Alan Nield, Gwynne Parry Jones and Ray Wilton. Particular thanks go to Ben Powell, who accompanied John and me on the visit to the Virginia Institute of Marine Science (VIMS) and provided excellent technical support, as well as helping with the work at Vivian quarry.

The visit to VIMS was arranged with the assistance of Don Wright; the observational campaign in the York River was led by Carl Friedrichs and John Brubaker. Numerous members of the academic and technical staff at VIMS as well as several students helped with the data collection; in particular I would like to acknowledge the contribution made by Lorraine Brasseur, Grace Battisto, Todd Nelson and Bob Gammisch. Thanks also to Charles Machen, captain of the RV Langley, his crew, and the small boat operators.

The other members of my supervisory committee, Alan Davies, John Howarth and Tom Rippeth provided useful advice, help and encouragement and engaged in many interesting discussions.

Financial support was provided by a NERC studentship. The visit to VIMS was funded by the Drapers' Company.

CONTENTS

List of Figures

Chapter 5

Chapter 6

Appendix 6

List of Tables

List of Symbols

All units used are S.I.; where there may be confusion about the units, these are stated.

Latin alphabet

A	constant
A_0	constant vertical eddy viscosity for unstratified water column
a	amplitude of wave motions
B	rate of production of TKE by buoyancy (W kg^{-1} or W m^{-3}: units stated in text)
b	constant used in N_z parameterization
b_i	measured velocity along beam i
b_N	noise in along-beam velocity measurement
C	speed of sound
C_D	drag coefficient
c	dimensionless constant used in calculation of Ozmidov scale
D	ADCP depth cell size
$E(k)$	Energy contained in turbulent motions of wavenumber k
F_D	ADCP doppler shifted frequency
F_0	ADCP transmitted frequency
g	acceleration due to gravity
H, h	water depth
K	upper limit at which autocovariance of velocity fluctuations $\rightarrow 0$
K_z	vertical eddy diffusivity
k	wavenumber
k_s	surface drag coefficient
l_o	Ozmidov length scale of turbulent motions
m	number of measurements in ADCP depth cell = D/T_P
M	number of ADCP velocity measurements in averaging period
n	number of pings in pre-averaging of ADCP velocity data
N	buoyancy frequency (Brunt-Väisälä frequency) (rad s^{-1})
N_z	vertical eddy viscosity
P	rate of shear production of TKE (W kg^{-1} or W m^{-3}: units stated in text)
p	pressure
Q	parameter proportional to turbulent kinetic energy (J kg^{-1})
$q^2/2$	turbulent kinetic energy (J kg^{-1})

R ADCP correlation at lag T_L

Rf flux Richardson number

Ri gradient Richardson number

Ri_o overall Richardson number

Ri_x horizontal Richardson number

r correlation coefficient of regression

S salinity (psu)

$T(k)$ transfer of energy between turbulent motions with different wavenumbers k

T_L ADCP time lag between pulses

T_P ADCP pulse length

$\hat{U}$ depth mean velocity

$\hat{U}_2$ depth mean M_2 current amplitude

u horizontal velocity

$\overline{u}$ mean velocity in x-direction (ADCP beams 1 and 2)

u' turbulent fluctuation in velocity in x-direction

$\widetilde{u}$ velocity fluctuation in x-direction due to waves

u_* friction velocity

u_1 horizontal velocity in beam1 (similarly for beam 2)

u_A horizontal velocity (beams 1 and 2) in ADCP coordinate frame

u_i, u_j velocity in tensor notation $(i, j = 1, 2, 3)$

u_i velocity in x-direction along beam i in fixed coordinate system (Appendix 6)

u_{iT} velocity in x-direction along beam i in tilted coordinate system (Appendix 6)

u_N noise in along-beam velocity measurement

u_n horizontal velocity in depth cell n

u_R velocity along channel

V velocity of reflectors

V_a ambiguity velocity

$\overline{v}$ mean velocity in y-direction (ADCP beams 3 and 4)

v' turbulent fluctuation in velocity in y-direction

$\widetilde{v}$ velocity fluctuation in y-direction due to waves

v_3 horizontal velocity in beam 3 (similarly for beam 4)

v_A horizontal velocity (beams 3 and 4) in ADCP coordinate frame

v_i velocity in y-direction along beam i in fixed coordinate system (Appendix 6)

v_{iT} velocity in y-direction along beam *i* in tilted coordinate system (Appendix 6)

v_R velocity across channel

W wind speed

$\overline{w}$ mean velocity in z-direction (vertical)

w' turbulent fluctuation in velocity in z-direction

$\tilde{w}$ velocity fluctuation in z-direction due to waves

w_1 vertical velocity in beam1 (similarly for beams 2, 3, 4)

w_i velocity in z-direction along beam *i* in fixed coordinate system (Appendix 6)

w_{iT} velocity in z-direction along beam *i* in tilted coordinate system (Appendix 6)

x_A x-coordinate in ADCP coordinate frame (plane of beams 1 and 2)

x_i , x_j distance in tensor notation

x_R x-coordinate corrected to along-channel direction

y_A y-coordinate in ADCP coordinate frame (plane of beams 3 and 4)

y_R y-coordinate corrected to across-channel direction

$Z(k)$ total energy transfer between wavenumbers

Greek alphabet

α constant used in N_z parameterization

β constant used in N_z parameterization

γ angle of heading of ADCP relative to wave direction

γ_R factor to account for non-independence of velocity fluctuations in estimate of Reynolds stress

γ_S factor to account for non-independence of velocity fluctuations in shear calculation

δ efficiency factor of tidal mixing

δ_s efficiency factor of wind mixing

δ_{ij} Kronecker delta

ε rate of dissipation of TKE (W kg^{-1} or W m^{-3}: units stated in text)

ζ distance of displacement of fluid particle

η difference in height above datum of water level at two tide gauges

θ inclination of ADCP beam angle to vertical

θ_H angle of heading relative to tidal flow direction

κ von Kármán's constant

μ	dynamic molecular viscosity
μ_2	second moment
μ_4	fourth moment
ν	kinematic molecular viscosity
ξ	constant used in N_z parameterizations
ρ	density
ρ_0	reference density
ρ_i	ratio of autocovariance to variance of $b_i'^2$
ρ_s	density of air
σ	standard deviation
σ_H	horizontal velocity standard deviation
σ_N	along-beam velocity standard deviation
σ_P	standard deviation of TKE production estimate (W kg^{-1})
σ_R	standard deviation of Reynolds stress estimate (m^2 s^{-2})
σ_S	standard deviation of velocity shear estimate
σ_T	density – 1000 (kg m^{-3})
σ_ψ	standard deviation of phase shift ψ
τ	Reynolds stress $-\rho\overline{u'w'}$
τ_b	Reynolds stress at the bed
τ_x	Reynolds stress in plane of beams 1 and 2
τ_y	Reynolds stress in plane of beams 3 and 4
τ_v	Viscous shear stress
ϕ	Potential energy anomaly
χ_i	true velocity along beam i
ψ	ADCP phase shift
ψ_{12}	ADCP roll angle (+ for beam 2 higher than beam 1)
ψ_{34}	ADCP pitch angle (+ for beam 3 higher than beam 4)
ψ'_{34}	rotation about tilted x-axis (in ADCP tilt transformations)
ω	frequency of wave motions

CHAPTER 1

Introduction

1.1 The shelf sea and estuarine environment

Current environmental concerns indicate the need to study the physical processes which take place in shelf seas and estuaries. The coastal regions of shelf seas are increasingly subject to large influxes of pollutants: industrial, agricultural or domestic in origin, and the eventual fate of these pollutants must be known in order to ensure that they do not unduly degrade the marine environment. The welfare of the shelf sea environment therefore requires the implementation of effective coastal management procedures, informed by an understanding of the mechanisms governing the offshore transport of pollutants, as well as their distribution through the water column.

The discharge of pollutants into estuaries and shelf seas has a direct impact on aquaculture and fisheries. These industries are also affected by primary production in the water column, which, in turn, is affected by the physical forcing mechanisms controlling the distribution of both nutrients and phytoplankton through the water column (Sharples *et al.* 2001; Moore *et al.*, 2003). A greater understanding of the physical processes and their effect on the ecology and water quality of the marine environment is therefore of the utmost importance regarding the effective management of fisheries and aquaculture.

Further questions exist regarding the role of shelf seas in controlling atmospheric CO_2 and the effect of the processes taking place in these regions on climate change. The mechanism governing the air-sea exchange of CO_2 is still not well understood, although some observers have found certain regions of the shelf seas, such as the European shelf (Frankignoulle and Borges, 2001) and the East China Sea (Wang et al., 2000) to be a sink for CO_2. The picture is complicated by research in other regions: Cai *et al.* (2003) found the South Atlantic Bight to be a source of CO_2, while Borges and Frankignoulle (2003) observed that the waters of the English Channel appeared to have no net effect on atmospheric CO_2. It is acknowledged that the air-sea exchange of CO_2 is influenced by a number of physical factors, such as tidal mixing, wind speed and freshwater input (Bakker *et al.*, 1996), indicating that advancing our knowledge of the physical processes taking place in the shelf sea and

estuarine environments will give us a greater understanding of some of the factors involved in climate change.

The degree to which the shelf sea environment is exploited as an energy source has increased a great deal in the recent past: offshore oil and gas rigs have existed for many years, offshore wind turbines have recently begun to be constructed, and underwater turbines are now being designed to harness the energy in the tidal currents. The large forces which operate in the near-bed region as a result of tidal flow have important implications concerning the design of these offshore structures. It is imperative, therefore, to improve our understanding of these forces, and the associated erosion and deposition of sediments, in order to ensure both efficiency and safety in the design and construction of offshore structures.

The development of accurate models of water quality, ecosystems and sediment transport is an important goal of current research; these are necessary in order to predict the likely effects of such activities as waste disposal in estuaries and coastal regions. Such models require an underlying representation of the effects of turbulent mixing processes, in the form of a turbulence closure model. In order to test the performance of such models, it is necessary to measure the turbulent parameters directly and compare the measurements with the results of the model.

In this study, the observational work focuses on an estuarine system. This is an environment which has much in common with the coastal region of shelf seas, of which it is a simplified, quasi-two-dimensional case. An estuary can be thought of as a laboratory in which many of the physical processes which take place in the shelf seas can be observed and analysed in detail. Estuaries are generally more accessible than shelf seas for intensive field work, and observational work can easily be carried out using small boats making the work more economical in terms of both time and money than working in the deeper regions of the shelf seas which are more remote from land. Research in estuaries therefore makes an important contribution to the furthering of our understanding of shelf sea processes in general.

1.2 Mixing processes

Vertical mixing and horizontal transport of pollutants and particulate matter in the water column are controlled by tidal flow and turbulence. In the oceans and atmosphere, kinetic energy is transferred to the small scales, at which dissipation occurs, through the action of turbulence. A large proportion of the turbulent kinetic energy (TKE) in the marine environment is generated by the action of frictional stresses in the bottom boundary layer, which extract tidal energy from the mean flow and convert it into TKE; it has been estimated that over 90% of the TKE in the entire water column is generated in the 10% of the water column nearest the bed (Bowden, 1983).

Most TKE is eventually dissipated to heat, but a small proportion of the energy of the turbulent motions is used to mix the water column, increasing the potential energy of a stratified water column. Turbulent mixing erodes stratification and controls the vertical exchange of momentum, heat and salt (Soulsby, 1983; Grant and Madsen, 1986; Peters, 1997; Simpson, 1998) and is also important in determining the distribution through the water column of particles, including phytoplankton (Koseff *et al.*, 1993; Sharples *et al.*, 2001) and fine sediments, as well as pollutants, so therefore plays an important part in determining the biogeochemical nature of the water column.

The nature of turbulence in shelf seas and estuaries is quite distinct from that of the deep ocean. Tidal currents in the deep ocean are generally weak and the dissipation of energy is low. At the shelf edge, the abrupt reduction in the depth causes an increase in the current speed, which results in a higher dissipation rate of tidal energy in the shelf seas, although much of the energy from the astronomical tides which is eventually dissipated in this region has its origins in the deep oceans (Simpson, 1997). The analysis and prediction of tides has been well understood since the work of Lord Kelvin in the nineteenth century (e.g. Pugh, 1987). The manner in which the tidal currents interact with turbulent processes to transport dissolved and particulate matter through a combination of vertical mixing and transport due to the ebb and flood of the tide is less well understood, and it is only recently that instruments have been

developed which have the ability to record relatively long and accurate time series of turbulent processes in shelf seas.

The turbulence-generating frictional stresses in the bottom boundary layer slow down the rotation of the earth and cause a change in the orbit of the moon, which is required for the conservation of angular momentum of the earth-moon system (Simpson, 1997). Estimates of the global dissipation rate can therefore be made from measurements of the change in the orbit of the moon. Recent estimates (Munk and Wunsch, 1998) give the total lunar contribution to dissipation as 3.2TW with an additional solar contribution of 0.5TW. A total of 2.6 TW is estimated to be dissipated in the bottom boundary layer of shelf seas by the action of turbulence. The relative magnitude of the energy dissipation rate in the shelf seas indicates the importance of these regions as a major sink for tidal energy.

1.3 A brief history of the observation of marine turbulence

Finding an effective way of measuring turbulence in tidal flows is a difficult task; it is necessary to obtain profiles of the relevant parameters at high frequency in an environment in which large stresses operate. A major problem is that the instruments need to be robust in order to withstand the stresses: a tidal flow of 1 ms^{-1} produces a stress at the boundary of $\tau = \rho u_*^2 \approx 1025 \times 0.05^2 \approx 2.56 Pa$. In order to produce a similar stress on the ground due to atmospheric effects would require a wind of strength close to that of hurricane force of 32.7ms^{-1} (Simpson 1997). Large structures which are robust enough to withstand such stresses while moored on the sea bed are likely to be responsible for the production of some turbulence since they interfere with flow in the water column, and are therefore responsible for the creation of some of the turbulent effects they are required to measure.

Some of the earliest measurements of shelf sea turbulence were made by Bowden and Fairbairn (1952) who used rotating impeller current meters. However, the velocity measurements made using current meters are integrated over time, averaging out the turbulent fluctuations. This means that they are more suited to the measurement of mean flow rather than rapidly changing fluctuations.

Bowden and Howe (1963) investigated near-bed turbulence using an electromagnetic flow meter which works by producing a strong magnetic field using a coil in the flow meter head. The movement of the water through the magnetic field produces a voltage proportional to its velocity; the voltage is measured and the flow velocity calculated. This instrument can measure a vertical component of the flow as well as the horizontal component, hence a direct calculation of the Reynolds stresses can be made. Their measurements also enabled the calculation of the vertical scale of the turbulence as well as the turbulent intensity, but in common with all direct measuring techniques, the instrument required a large and robust mooring making it liable to induce turbulence in the water. It was also unable to detect some of the smaller scales of motion and measurements were limited to a few metres above the bed.

Hot wire anemometers have been used extensively by meteorologists to measure atmospheric boundary layer turbulence since the 1930s (Taylor, 1935; Sutton, 1953). These work on the principle that a wire heated by an electrical current will be cooled by fluid flowing past it, causing a decrease in its resistance proportional to the velocity of the fluid. Such an instrument has great advantages in the measurement of turbulence, being of small size (hence it induces little turbulence) and capable of measuring both large and small scale turbulent structures. Attempts to use a hot wire anemometer to measure turbulence in the ocean presented a number of difficulties, including problems due to the higher density and drag of sea water compared to air, the high conductivity of sea water and the problem that organic matter would often soon start to coat the wire (Grant *et al.*, 1962). The hot film probe is based on the same principles as the hot wire anemometer, but uses a platinum film around a glass cone, instead of the hot wire. This makes it more suited to use in the ocean, since it avoids the problems of drag and biological interference. Using this instrument, Grant *et al.* (1962) made extensive measurements of turbulent parameters in a tidal channel, including measurements of dissipation, and obtained results which appeared to prove experimentally the Kolmogorov –5/3 power law for the inertial subrange (see section 2.3), although these have recently been questioned (e.g. Long, 2003).

The next major step in the development of marine turbulence measurements occurred in the 1980s with the development of microstructure profilers, such as the Fast, Light, Yo-Yo (FLY) profiler (Dewey *et al.*, 1987). The FLY profiler is a free-falling

instrument which measures velocity shear, temperature, salinity and depth. The components of velocity shear can then be used to calculate the rate of dissipation of turbulent kinetic energy (see section 2.2). Successful measurements of turbulent dissipation have been made using such a profiler and some important results obtained regarding the evolution and the nature of turbulence in shelf seas (e.g. Dewey *et al.*, 1987; Dewey and Crawford, 1988; Simpson *et al.*, 1996; Simpson *et al.*, 2000; Rippeth *et al.*, 2001; Rippeth *et al.*, 2003), estuaries (Peters, 1997; Peters and Bokhorst, 2001), tidal channels (Lu *et al.*, 2000), coastal waters (Dewey *et al.*, 1987), on the continental slope (Lueck *et al.*, 1983) and in deeper oceanic regions (e.g. Gargett and Osborn, 1981). Some of these results will be discussed in section 1.4.

Laser methods such as particle image velocimetry (PIV) are also now being applied to the observation of marine turbulence (Bertuccioli *et al.*, 1999; Doron *et al.*, 2001). This technique, which measures two components of the instantaneous velocity distribution within a flow, thereby providing a time series of the velocity distribution over a sample area, can be used to test some of the commonly held assumptions regarding turbulent motions, such as the assumption of isotropy at the dissipation scale. Some of these results will be discussed further in chapter 2.

Averaging of the measured velocities has been widely used in the past in order to reduce uncertainties in velocity measurements, such as the current meter measurements described earlier. In order to use the velocities in turbulence analysis, they must be measured at high spatial and temporal resolution without averaging over more than a few seconds. Since the 1980s, instruments using acoustic Doppler technology to measure water flow velocities have improved to the extent that the raw data are accurate enough to be used to obtain turbulent parameters. Two instruments are currently available for obtaining these measurements: the acoustic Doppler velocimeter (ADV) and the acoustic Doppler current profiler (ADCP). The ADCP has the advantage of being a non-intrusive method which uses remote sensing: the flow velocities measured are at some distance from the instrument; therefore it does not directly influence the flow and the turbulence at the point of measurement. This is less true of the ADV, since the sampled volume is only a few centimetres from the probe, which must be mounted on a robust mooring to withstand the near-bed

stresses. An additional advantage of both instruments is that they can be left in situ to collect data over a period of days or even weeks.

The ADV is able to measure the three components of velocity, at extremely high frequency, typically of order 100 Hz, for a small volume of the water column, of order 1 cm^3. A direct estimate of the Reynolds stress can then be obtained from the measurements of the high frequency turbulent fluctuations (e.g. Voulgaris and Trowbridge, 1998). By contrast, the ADCP measures velocities throughout the water column with a spatial resolution ranging from a few centimetres to several metres.

The recent development of high frequency broadband ADCPs (described in detail in chapter 3) has enabled progress to be made in the study of turbulence in coastal waters and shelf seas. The main focus of this study is on ADCP measurements in which the variance method is used to calculate turbulent parameters from the variances of the along-beam velocities of opposing beams. The ADCP and the variance method are described in detail in chapter 3. This method originated in studies in atmospheric physics, where it was applied to measurements made using Doppler radar (Lhermitte, 1968; Vincent and Reid, 1983). It was first used in the marine environment by Lhermitte (1983) using Doppler sonar. As improved marine acoustic Doppler instruments became available in the 1980s and 1990s, the technique was developed further by Lohrmann *et al.* (1990), and later by other investigators (e.g. Gargett, 1994; Van Haren *et al.*, 1994; Stacey *et al.*, 1999a, b), who used it to calculate the Reynolds stress, rate of production of TKE (e.g. Lu *et al.*, 2000; Rippeth *et al.*, 2003) and eddy viscosity (Rippeth *et al.*, 2002). By using a modified ADCP, with one beam redirected vertically, estimates of the TKE and the TKE dissipation rate can also be made from the vertical turbulent velocity fluctuations (Gargett, 1994, 1999), using the assumption that the large scale turbulent fluctuations have one characteristic length scale (Taylor, 1935).

The ADCPs which are currently available can measure velocities at a rate of up to 20 Hz, although it is still not possible to record velocities at a frequency greater than about 2 Hz. This is, however, fast enough and spatially accurate enough for the eddies to be sampled at scales involved in the transfer of momentum. The estimates of the turbulent parameters from the ADCP measurements in homogeneous conditions

have been shown to agree well with the theory, using a model based on the law of the wall and the assumption of steady flow (Rippeth et al., 2002). Estimates of the rate of production of TKE from ADCP measurements have also been shown to be in good agreement with simultaneous microstructure measurements of the rate of dissipation of TKE (Lu *et al.*, 2000; Rippeth *et al.*, 2003).

1.4 Turbulence and mixing in different regimes

Water column structure in estuaries and shelf seas is largely controlled by turbulence forced by tidal and wind stirring. Variations in the intensity and distribution of these turbulent mixing processes combine with the dominant buoyancy source to define the characteristic regimes of these seas (Figure 1.1). A short description of each: the mixed, seasonally stratified, region of freshwater influence (ROFI) and estuarine regimes, will now be given.

1.4.1 Mixed and seasonally thermally stratified regimes

The mixed and seasonally thermally stratified regimes in shelf seas arise from the interaction of tidal stirring and buoyancy from surface heating (Simpson *et al.*, 1996; Simpson *et al.*, 2000; Sharples *et al.*, 2001). In the absence of a horizontal salinity gradient, a vertically mixed water column results when there is sufficient mixing due to tidal and wind stirring to overcome any stratification which arises from the input of surface buoyancy in the form of heat. Stratified and mixed regions of the shelf seas are separated by tidal mixing fronts, the position of which can be determined on the basis of the competition between heating and stirring. Assuming uniform heating and cooling over a large area, and the dominance of tidal over wind stirring effects, the stratification criterion is defined by a critical value of the parameter $H/\hat{U}_2^3$, (Simpson and Hunter, 1974), where H is the water depth and $\hat{U}_2$ is the M_2 current amplitude. Wind stirring can also affect the position of the tidal mixing front, with the effects of wind stirring becoming more important as the water depth decreases (Simpson *et al.*, 1978).

Recent studies in mixed waters using a free-falling TKE dissipation profiler show that the dissipation rate reaches a maximum near the bed, decreasing with height (Burgett

et al., 2001; Simpson *et al.*, 1996; Simpson *et al.*, 2000). There is a quarter diurnal variation in the turbulent dissipation, with maximum dissipation corresponding to maximum current speeds, and a phase lag which increases with height above the bed; it was demonstrated that this resulted from a phase lag in the TKE production term, which also appears to be responsible for a similar lag in the suspended sediment concentration (Simpson *et al.*, 2000).

Observations in a thermally stratified region of the Western Irish Sea, show dissipation rates which are generally lower than in the mixed region (Simpson *et al.*, 1996) with a quarter-diurnal variation which is only apparent in the lower part of the water column, well below the main seasonal thermocline.

In contrast with the Western Irish Sea, observations made in a thermally stratified region of the English Channel show higher dissipation rates and a measurable quarterdiurnal variability extending almost up to the base of the thermocline (Sharples *et al.*, 2001). In common with the mixed water column, the increasing phase lag with increasing height above the bed can be seen in both the Irish Sea and the English Channel observations.

1.4.2 Estuaries

An estuary can be defined as 'a semi-enclosed coastal body of water having a free connection with the open sea and within which the sea water is measurably diluted with fresh water deriving from land drainage' (Cameron and Pritchard, 1963).
The input of fresh water at the upper end of the estuary and the input of denser, saline water at the mouth, combined with vertical mixing, drive a gravitational circulation (Hansen and Rattray, 1965). In its simplest form, assuming the tidal flow is weak enough to be neglected, and that no mixing of the layers takes place, the circulation would reduce to a seaward flow of fresh water overlying a stationary layer of sea water. In order for a density-driven circulation to develop, there must be some mixing; in this simplified case, such mixing would take the form of entrainment, as the high current shear between the layers produces instabilities which allow some of the saline water to be entrained into the freshwater layer (Dyer, 1997). As the tidal flow increases, mixing will also take place due to the production of TKE near the bed.

The characteristics of a particular estuary are determined by the freshwater and tidal components of the flow, and modified by a wind stress component. They can be classified according to the degree of stratification (Cameron and Pritchard, 1963; Pritchard, 1967), into highly stratified, moderately (or partially) stratified and vertically homogeneous.

In estuaries in which the tidal flow is weak, the gravitational circulation dominates over the effects of the tide and a sharp halocline develops (Dyer, 1997), resulting in a highly stratified estuary, such as the Columbia River estuary, on the border between the states of Oregon and Washington (Kay and Jay, 2003). Conversely, when the tidal flow is strong and the tidal range great compared to the depth, the tidal flow dominates and the tidally induced turbulence is strong enough to ensure that the estuary remains well-mixed throughout the tidal cycle. An example of such a vertically homogeneous estuary is the Conwy in North Wales (Simpson *et al.*, 2001), although it has been argued that such an estuary may simply be an extreme case of a partially stratified estuary, in which the degree of stratification varies with tidal flow rates and variations in freshwater input (Pritchard, 1967).

In a partially stratified estuary, the water column stratifies on the ebb, when the current shear acts positively with the estuarine circulation to enhance stratification; with maximum stratification occurring around the end of the ebb (Simpson, 1997). On the flood, the current shear acts against the stratification, with minimum stratification occurring during the latter part of the flood when complete vertical mixing may occur. Towards the end of the flood, with the water column already vertically mixed, the effect of the current shear is to push heavier water over lighter, setting up instabilities in the water column which may induce convective overturns. This sequence of events is called Strain Induced Periodic Stratification (SIPS; Simpson *et al.*, 1990) and has been observed in a number of partially stratified estuaries, for example, the York River estuary, Virginia (Sharples *et al.*, 1994) and the Hudson River Estuary (Peters and Bokhorst, 2001). The SIPS mechanism and the resulting periodic mixing and stratification of the water column are shown schematically in Figure 1.2; the theory is covered in section 2.4.4. The gravitational circulation as defined by Hansen and Rattray (1965) may also be increased by tidal

straining, due to the flood-ebb asymmetry in eddy viscosity (Jay, 1991; Geyer *et al.*, 2000).

Partially stratified estuaries may alternate between periods of high vertical salinity stratification and vertical homogeneity, on a cycle which correlates closely with the spring-neap cycle. Such a cycle of stratification and mixing has been observed in the York and Rappahannock Rivers, Virginia (Haas, 1977), where well-mixed conditions are associated with high spring tides. The spring-neap cycle was found to have a greater influence on the degree of stratification than the variation in freshwater input to the estuary, although variations in river flow also affect the degree of stratification. A further variation in stratification can occur due to wind stirring, which can dominate tidal effects in shallow estuarine environments (Sharples *et al.*, 1994).

1.4.3 Coastal Regions of Freshwater Influence (ROFIs)

A region of freshwater influence (ROFI) arises in a coastal region when there is significant input of freshwater buoyancy at the boundary from one or more discrete coastal sources such as an estuary (Simpson *et al.*, 1990). The ROFI is not limited to the immediate vicinity of the estuary, however, and in some cases can extend up to several hundred kilometres from the mouth of the estuary. For example, a large area of the East China and Yellow Seas is influenced by the outflow of the Chiangjiang (Beardsley *et al.*, 1985), and a large area of the North Sea is influenced by the discharge from the Rhine (Simpson and Souza, 1995).

The freshwater input in a ROFI drives a gravitational circulation in which fresh water tends to move seaward over heavier, saline water moving landward (Simpson *et al.*, 1990), as in the simpler case of an estuary. The flow is also influenced by the effect of the earth's rotation which causes the low salinity water from the estuary to flow along the coast, with the land on its right in the Northern Hemisphere (Simpson, 1997). The competition between stratification and stirring is more complex in a ROFI than in either estuaries or regions in which the stratification results from seasonal thermal effects, due to the horizontal non-uniformity of the input of buoyancy which enters through a lateral boundary. This makes a ROFI more difficult to analyse and to reproduce in models than the other regions. It is, however, a very important area to

understand, since management of coastal areas is increasingly dependent on predictive models of the spreading of freshwater run-off (Rippeth *et al.*, 2001).

In ROFIs, as in estuaries, SIPS has been observed, for example, in Liverpool Bay (Rippeth *et al.*, 2001), the Rhine outflow region of the North Sea (Simpson and Souza, 1995) and San Francisco Bay (Stacey *et al.*, 1999b). Observations in ROFIs show a cycle of turbulent dissipation different from that of a mixed or thermally stratified water column (Rippeth *et al.*, 2001). The stratification which occurs on the ebb confines the dissipation to the lower part of the water column. On the flood, complete vertical mixing allows the strong dissipation to extend throughout the water column. The cycle of dissipation is therefore typically quarter-diurnal in the lower part of the water column, but semi-diurnal in the upper part of the water column.

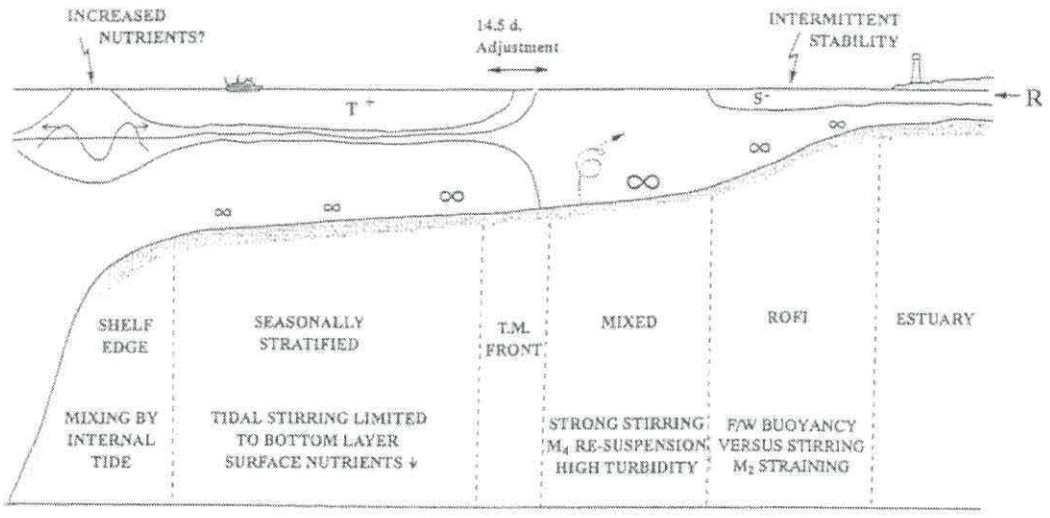

Figure 1.1: Tidal processes in the characteristic regimes of the shelf seas. Variations in the intensity of stirring are indicated by the size of the ∞ symbols. (Simpson, 1997)

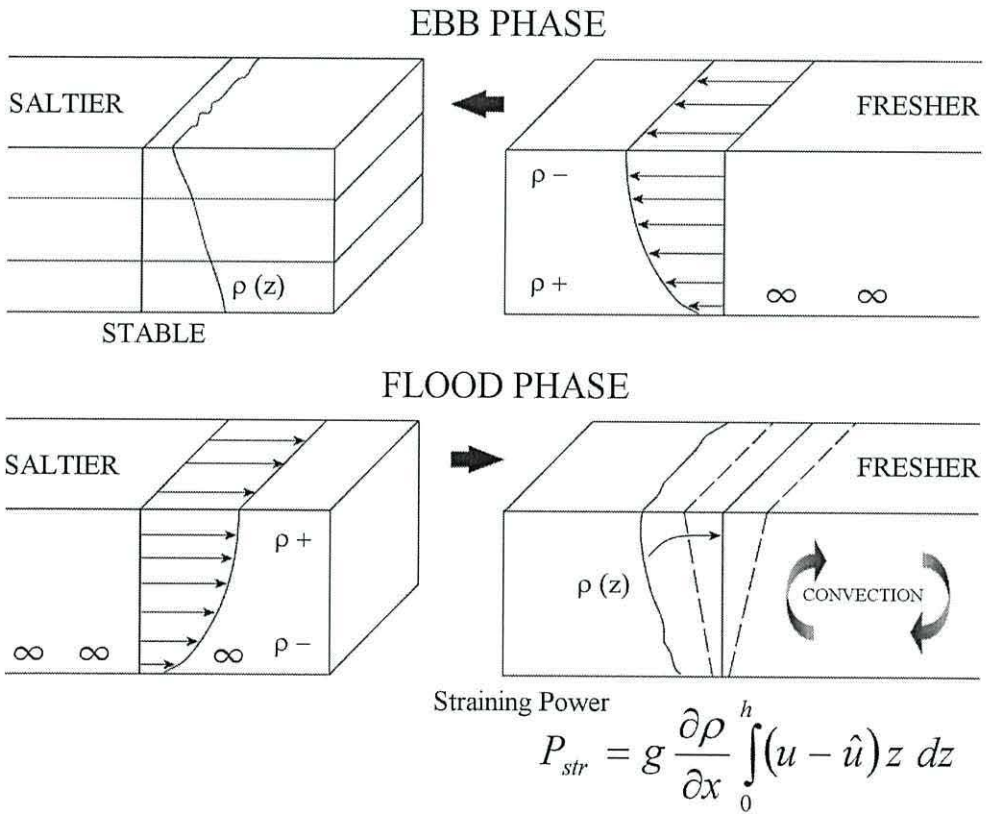

Figure 1.2: Schematic of tidal straining. During the ebb, the fresher surface water is moved seaward faster than underlying more saline water creating a stratified tidal column. On the flood, the shear acts to produce a reverse differential advection which tends to reduce stratification; complete vertical mixing may occur at the end of the flood. (Fisher, 2003)

1.5 Aims and Observational Strategy

In order to understand the physical processes which take place in the shelf seas, it is essential to understand the simpler case of an estuary. A partially stratified estuary is a simplified, quasi-two-dimensional representation of a ROFI, and as such can be used as a laboratory to explore many of the aspects of turbulent processes which occur in the shelf seas. A partially stratified estuary, the York River estuary in Virginia, USA, was therefore chosen to be the main study site. The broad aim of the observations at this location was to exploit the ADCP variance method and apply it to partially stratified conditions. The proposed observations were similar to some which had previously been made in a vertically mixed tidal channel (Rippeth *et al.*, 2002), and the results from this earlier study will be used to compare the turbulent parameters measured in the partially mixed York River estuary with those of a vertically mixed water column. They will also be used to demonstrate how recent advances in the ADCP technology have improved the quality of the data used in turbulence measurements. In particular, a new fast-sampling ADCP mode (detailed in chapter 3), which became available shortly before the planned observation period was used for the first time in the York River. The measurements were therefore expected to be of a higher quality than was previously possible.

The specific objectives of the observations were:

a) To test the capabilities and the limitations of the variance method, by analysing the noise characteristics of the ADCP measurements, and comparing Reynolds stresses estimated using the variance method with those from an ADV.
b) To examine the evolution of turbulence in detail over an entire spring-neap tidal period and analyse its interaction with the periodic stratification.
c) To test the measurements against the equations of motion in the form of an along-channel momentum balance.
d) To compare the drag coefficient obtained from the near-bed measurements of Reynolds stress and the along-channel velocity with a quadratic drag law.

There is a distinct difference in the York River estuary in the level of stratification not only between ebb and flood, but also between spring and neap tidal periods. Previous studies in this region (e.g. Haas, 1977; Sharples *et al.*, 1994) have examined the cycle

of stratification and mixing in some detail; a semi-diurnal cycle of stratification and mixing is observed during neap tides, with complete vertical mixing usually occurring at springs.

The time chosen for the study was in March-April, when the increase in run-off due to the snow melting on the hills and mountains above the York River meant that the stratification was likely to be more marked than at other times of the year. In addition to measurements of mean flow and turbulent parameters, measurements of the density field were made, as well as surface elevation and measurements of suspended sediment concentration; an analysis of the latter is being undertaken by colleagues at the University of Wales, Bangor and at the Virginia Institute of Marine Science (e.g. Scully and Friedrichs, 2003).

1.6 Summary of layout of thesis

Chapter 2 outlines the theory of turbulence and the application of the theory to tidal flows. In chapter 3 the ADCP is described in detail and the data analysis and error analysis methods used are introduced. Chapter 4 contains the results from the York River estuary observations. In chapter 5, the results are interpreted with reference to previous theoretical and empirical results. Chapter 6 contains a detailed analysis of the errors and uncertainties in the ADCP turbulence estimates with particular reference to the York River results; the Menai Strait and noise testing data are used for comparison purposes. In chapter 7 the results are discussed and summarised and some conclusions drawn from the work.

CHAPTER 2

The Theory of Turbulence

This chapter is concerned with the aspects of turbulence theory which are necessary for an understanding of the observations and their analysis. The terms and assumptions used will be discussed and the equations and parameters used in the data analysis will be derived and explained.

Turbulent flows are flows which contain random fluid motions. These flows occur at high Reynolds numbers, that is, when the ratio of inertial stress to viscous stress (ul/ν) is large. A direct analysis of turbulent motion would require measurement of each random fluctuation of each particle of fluid, which is clearly not possible. The only way in which turbulent motion can be analysed in detail, therefore, is to look at its statistical properties, such as the variance of the fluctuations. This statistical treatment of turbulence, first developed by Taylor (1935), requires certain assumptions to be made with respect to the turbulent motions. These assumptions will be used throughout this work.

2.1 Terms and Assumptions

The methods used here to analyse the turbulent processes can only be applied if it is assumed that the statistical properties of the turbulence do not change within the region in which measurements are averaged. This is the assumption of *statistical homogeneity*, which implies that the turbulence has the same structure and characteristics throughout the domain being considered (Hinze, 1959); if the flow is statistically homogeneous, it is reasonable to expect that the variance of the fluctuations is the same at all points in the domain.

A second assumption is that of *temporal stationarity*, which implies that the statistics of the flow do not change during the period of time over which the fluctuating quantities are averaged; both the mean flow and the variance of the fluctuations are assumed to be constant over this period.

It is appropriate to introduce here the concept of *isotropy*. Isotropic turbulence is turbulence in which the fluctuations in the x, y and z directions have the same

statistical properties; it is therefore turbulence which is independent of the position and orientation of the co-ordinate axes.

2.2 The Turbulent Kinetic Energy (TKE) Equation

In this section index notation will be used in order to make the equations more manageable, since it is necessary to consider all three dimensions simultaneously. In this notation, the velocities in the three directions (u, v, w) are denoted by u_i (or u_j) = u_1, u_2, u_3 respectively and the distances along the three co-ordinate (x, y, z) axes by x_i (or x_j) = x_1, x_2, x_3 respectively. Use of this notation implies summation over the three values of i (or j) whenever a subscript is repeated in a single term. The co-ordinate system used is one in which the x and y axes are in the horizontal plane and the z-axis is vertically upwards. In this section and throughout, the 'prime' symbol is used to indicate a fluctuating quantity and the overbar is used to indicate a mean quantity, in this case, a time average. Following the sign convention of other authors (e.g. Turner 1973), the acceleration due to gravity is represented here and throughout by $-g$.

As a tidal flow moves over the sea bed, the frictional stresses between the water and the sea bed and between adjacent layers of water give rise to random motions and the formation of eddies. If high frequency measurements of the water velocity at a fixed point are made over a period of time, these velocities can be split into a mean and a fluctuating part, using the Reynolds decomposition: $u_i = \overline{u}_i + u_i'$, the mean part representing the mean tidal velocity and the fluctuating part the turbulent velocity. The TKE is defined as the energy contained in the turbulent motions (u_i'), and can therefore be calculated from the variance of the velocities in each direction $\left(\overline{u_i'^2}\right)$. The TKE $q^2/2$, which is the amount of kinetic energy (in J kg^{-1}) which is contained in the turbulent motions, is then defined by:

$$\frac{q^2}{2} = \sum_{i=1}^{3} \frac{\overline{u_i'^2}}{2} \tag{2.1}$$

In a shear flow, the time average of the product of two fluctuations $\overline{u_i' u_j'}$ is non-zero, and the TKE is mainly derived from the mean flow through frictional effects

represented by the Reynolds stress or turbulent shear stress $\tau_{ij} = -\rho\overline{u_i' u_j'}$. τ_{ij} has the dimensions of a stress; in physical terms, τ_{ij} represents a momentum flux, that is, the rate at which momentum is exchanged from one layer of fluid to the adjacent layer due to turbulent motions. When the Reynolds stress is multiplied by the shear, the rate at which kinetic energy is transferred from the mean flow to the turbulent motions (P) is obtained.

The TKE equation is derived from the Navier-Stokes equation, given by (neglecting the effects of rotation):

$$\rho\left(\frac{\partial u_i}{\partial t} + u_j \frac{\partial u_i}{\partial x_j}\right) = -\frac{\partial p}{\partial x_i} - \rho g \delta_{i3} + \mu \frac{\partial^2 u_i}{\partial x_j \partial x_j} \tag{2.2}$$

where p is the pressure, μ is the molecular viscosity of the fluid and δ_{ij} is the Kronecker delta: $\delta_{ij} = 1$ for i = j; $\delta_{ij} = 0$ for i ≠ j.

The left hand side of equation (2.2) represents the momentum change of the fluid. The first term on the right hand side is a pressure term, the second term represents changes due to external forces (gravitational or buoyancy effects) and the third represents the viscous forces.

In time averaged form, equation (2.2) becomes (see Appendix 1 for details):

$$\frac{\partial \overline{u}_i}{\partial t} + \overline{u}_j \frac{\partial \overline{u}_i}{\partial x_j} = -\frac{1}{\rho_0}\frac{\partial \overline{p}}{\partial x_i} - \frac{\overline{\rho}}{\rho_0} g \delta_{i3} + \nu \frac{\partial^2 \overline{u}_i}{\partial x_j \partial x_j} - \frac{\partial \overline{u_i' u_j'}}{\partial x_j}$$

The extra term on the right hand side represents the frictional stress on the mean flow which is present in turbulent flow, and augments the viscous stress.

Changes in TKE are described by the TKE equation, which is derived by taking the product of u_i with the dynamical equations; a full derivation is given in Appendix 1. In simplified form, ignoring transport effects and assuming isotropy at the dissipation scale, this equation is:

$$\frac{1}{2}\frac{\partial\left(\overline{q^2}\right)}{\partial t} = -\overline{u_i' u_j'}\frac{\partial \overline{u}_j}{\partial x_i} - \frac{\overline{\rho' u'}_3}{\overline{\rho}} g - \nu\overline{\left(\frac{\partial u_i'}{\partial x_j}\right)^2} \tag{2.3}$$

where ν is the kinematic molecular viscosity. The left hand side of equation (2.3) represents the rate of change of TKE. The first term on the right hand side represents the rate of production of TKE (P) from the shear in the mean flow. The second term (B) represents the production or destruction of TKE via buoyancy effects. When the correlation $-\overline{\rho' u_3'}$ is positive, the effect of the buoyancy term is to produce TKE from gravitational potential energy via convection; when this correlation is negative, the buoyancy term represents the removal of TKE through its conversion to potential energy via mixing. The last term (ε) is the rate of viscous dissipation of TKE to heat. The equation can therefore be written: rate of change in TKE = $P + B - \varepsilon$.

A further simplification of the equation can be made in marine turbulence, since the buoyancy term can be neglected; even in stratified flows, only a small fraction of the turbulent kinetic energy is used to work against buoyancy forces (Gargett, 1994). If it is assumed that there is negligible change in the TKE $q^2/2$ over the averaging period, the production and dissipation terms can be considered to be in approximate balance, and the TKE equation simplifies to $P \approx \varepsilon$.

The dissipation term ε has nine components which are summed to get the total dissipation rate. Since isotropy is assumed:

$$\overline{\left(\frac{\partial u_1'}{\partial x_1}\right)^2} = \overline{\left(\frac{\partial u_2'}{\partial x_2}\right)^2} = \overline{\left(\frac{\partial u_3'}{\partial x_3}\right)^2}$$

It can also be shown that (e.g. Raudkivi and Callander, 1975):

$$\overline{\left(\frac{\partial u_i'}{\partial x_i}\right)^2} = \frac{1}{2}\overline{\left(\frac{\partial u_i'}{\partial x_j}\right)^2} \quad \text{for } i \neq j$$

The expression for the dissipation in equation (2.3) can then be written:

$$\varepsilon = 7.5\nu\overline{\left(\frac{\partial u_1'}{\partial x_3}\right)^2} \tag{2.4}$$

It is this expression for the rate of dissipation of TKE which is used in the analysis of the Fast Light Yo-yo (FLY) dissipation profiler measurements. The assumption of isotropy requires only one component of the dissipation rate to be measured.

However, significant errors in the dissipation estimate may occur should the assumption of isotropy be erroneous. The full dissipation term, if isotropy is not assumed, is (see Appendix 1):

$$\varepsilon = \nu \overline{\frac{\partial u_j'}{\partial x_i}\left(\frac{\partial u_i'}{\partial x_j} + \frac{\partial u_j'}{\partial x_i}\right)} \tag{2.5}$$

so there will be 12 terms in all. Recent work by Doron *et al.* (2001) in which five of the terms making up the dissipation term in equation (2.5) were measured directly using Particle Image Velocimetry (PIV), indicates that turbulence is clearly anisotropic even at dissipation scales. Their 'direct' measurements of the dissipation rate are consistent with locally axisymmetric turbulence (George and Hussein, 1991), that is, turbulence which is invariant with rotation around a preferred axis. The results of Doron *et al.* (2001) indicate that dissipation estimates which use measurements of $\partial u/\partial z$ or $\partial v/\partial z$ and assume isotropy at the dissipation scales, typically overestimate the dissipation rate by 30% to 100%.

2.3 The Energy Spectrum

Since the work of Kolmogorov (1941), it has been widely held that TKE is produced mainly at large scales, with the energy being transmitted to smaller and smaller eddies, until the length scale is small enough for viscous effects to be significant, at which point the energy is dissipated to heat. This is known as the energy cascade. All the TKE produced is eventually dissipated in this way, with most of the dissipation occurring at high wavenumbers. Neglecting the effects of transport and buoyancy, which in steady state turbulence are small compared to the dissipation and production terms, these last two take place at the same rate.

The distribution of TKE between different scales of wavenumber k is represented in the wave number spectrum $E(k)$ defined by (e.g. Tritton, 1977):

$$\frac{q^2}{2} = \int_0^\infty E(k)dk \tag{2.6}$$

The rate of change of energy associated with wavenumber k $\left(\partial E(k)/\partial t\right)$ can be expressed in terms of the transfer of energy between wavenumbers in the cascade

$T(k)$, and the energy dissipation $2\nu k^2 E(k)$ (e.g. Hinze, 1959; Raudkivi and Callander, 1975):

$$\frac{\partial E(k)}{\partial t} = T(k) - 2\nu k^2 E(k) \tag{2.7}$$

Another term $Z(k)$, which represents the total energy transferred from the range of wavenumbers between 0 and k to the range between k and infinity, can be defined (Raudkivi and Callander, 1975):

$$Z(k) = -\int_0^k T(k)\,dk \tag{2.8}$$

The four parameters described in equations (2.7) and (2.8) are plotted schematically in Figure 2.1. It is clear from this figure that most TKE is not contained in the largest eddies, but in those with a slightly higher wavenumber, that is, the region where the peak in the value of $E(k)$ occurs, although the production scale eddies may contain as much as 20% of the total TKE (Hinze, 1959). It is also apparent from the curves for $E(k)$ (the energy-containing eddies) and $k^2E(k)$ (the energy dissipation) that the peak value of $E(k)$ occurs at much lower wavenumbers than the peak value of $k^2E(k)$. In between these peaks there is a large range of wavenumbers associated with neither the energy-containing eddies nor the dissipation; this is the range at which the energy is transferred to smaller and smaller scales and contains the peak for the parameter $Z(k)$. This region is called the inertial subrange.

In a steady state, energy is transferred into the inertial subrange at the largest scales at the same rate as it is transferred out to the dissipation scales, so at these wavenumbers the energy spectrum is in equilibrium, that is $\frac{\partial}{\partial t} E(k) = 0$. Kolmogorov (1941) suggested that in this range of wavenumbers the parameter E should be independent of viscosity, so depends only on the wavenumber k and the dissipation rate ε. From equation (2.6), the dimensions of E are $[L^3T^{-2}]$, so using dimensional analysis the result $E(k,\varepsilon) = Ak^{-5/3}\varepsilon^{2/3}$ is obtained where A is a numerical constant. It follows that there should exist a range of wavenumbers in which a plot of E against $log_e(k)$ has a gradient of –5/3, as shown schematically in Figure 2.2. Experimental work (e.g.

Grant *et al.*, 1962) appeared to confirm that a range of wavenumbers with this power law exists in a tidal flow. However, this theory and the conclusions drawn from the experimental work are not universally accepted (Long, 2003).

The cascade theory states that as the eddies reduce in size, their anisotropy is lost, so that at the dissipation scales, the eddies have no directional preference. As the eddies reduce in size, the range of wavenumbers through which the energy has had to pass increases, and the original information about the direction of flow becomes lost. At very large wavenumbers, then, the turbulence is very close to isotropic, although, as mentioned in section 2.2, experimental results show that the turbulence does not conform to a true isotropic state even at the dissipation scales.

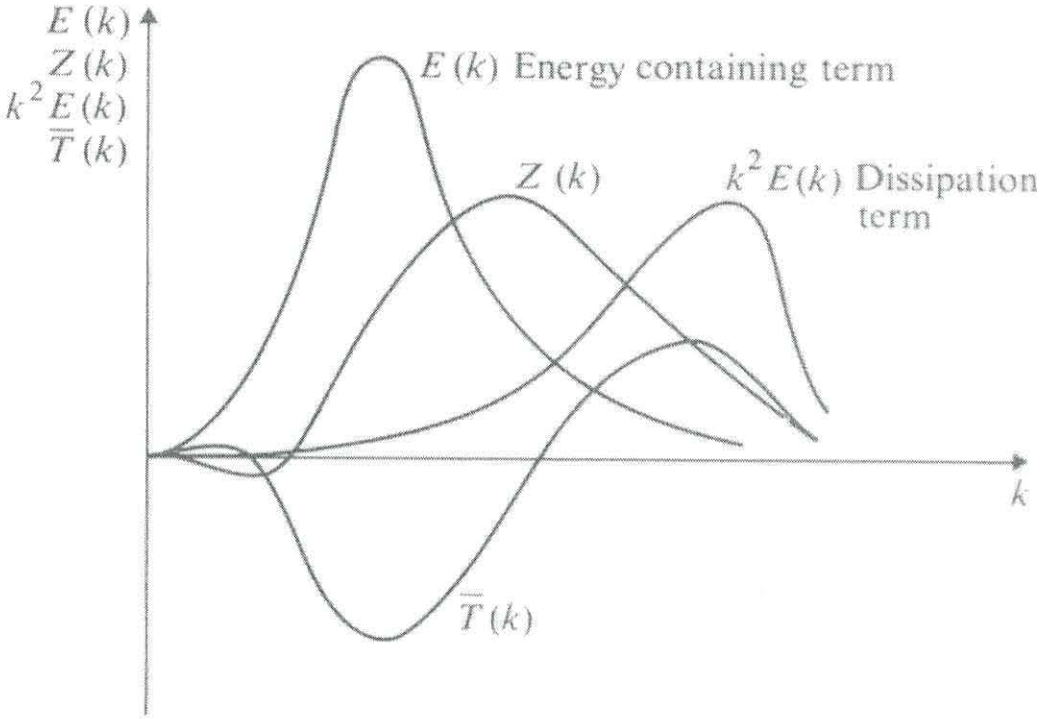

Figure 2.1: General forms of terms for energy $E(k)$, energy transfer $Z(k)$, energy dissipation $k^2E(k)$ and total rate of inertial energy transfer $T(k)$ (Raudkivi and Callander, 1975)

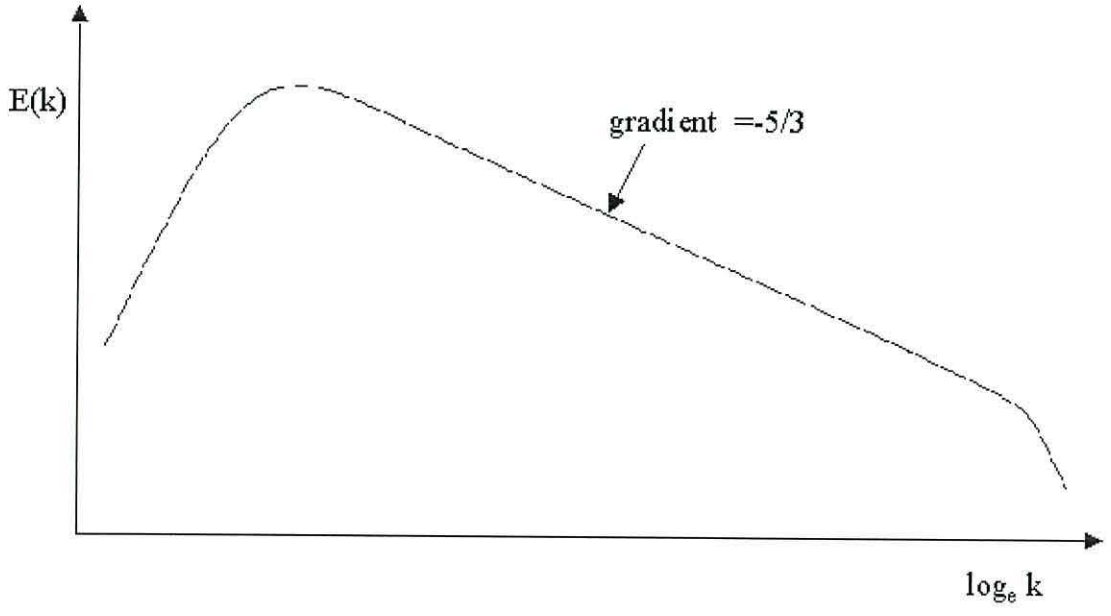

Figure 2.2: The energy cascade

2.4 Additional parameters

This section outlines the other parameters which will be used in the analysis of the York River observations; where appropriate, derivations are included.

2.4.1 Eddy Viscosity and Eddy Diffusivity

The momentum exchange of turbulence represented by the Reynolds stresses can be regarded as analogous to the molecular transport of momentum which is related to the kinematic molecular viscosity (Tennekes and Lumley, 1972). Using this analogy, the Reynolds stress is related to the eddy viscosity N_z by:

$$-\rho\overline{u'w'} = \rho N_z \frac{\partial \overline{u}}{\partial z} \tag{2.9}$$

just as the viscous stress τ_v is defined by the kinematic molecular viscosity ν:

$$\tau_v = \rho\nu\frac{\partial \overline{u}}{\partial z} \tag{2.10}$$

The Navier-Stokes equation (2.2) can then be written in terms of the eddy and molecular viscosities (see Appendix 1, equation 7):

$$\frac{\partial \overline{u}_i}{\partial t} + \overline{u}_j \frac{\partial \overline{u}_i}{\partial x_j} = -\frac{1}{\rho_0}\frac{\partial \overline{p}}{\partial x_i} - \frac{\overline{\rho}}{\rho_0} g\delta_{i3} + \frac{\partial}{\partial x_j}\left[(\nu + N_z)\frac{\partial \overline{u}_i}{\partial x_j}\right]$$

The eddy viscosity N_z, like ν, has dimensions [L^2T^{-1}]. However, unlike ν, it is a property of the flow, rather than the fluid. In a tidal flow, therefore, we expect to see temporal variation in the eddy viscosity, as well as variation with height above the bed. Using the ADCP measurements of Reynolds stress and shear, it is possible to make an estimate of the eddy viscosity throughout the water column and observe how it evolves over the tidal cycle.

The eddy diffusivity K_z is defined for a scalar quantity (e.g. density) in a similar way to the eddy viscosity:

$$-\overline{\rho'w'} = K_z \frac{\partial \rho_0}{\partial z} \tag{2.11}$$

In a stably stratified flow, $N_z > K_z$, since momentum transfer can still occur due to internal waves, but the transfer of scalars is inhibited by the stratification (Kundu, 1990). In a vertically mixed flow, $N_z \sim K_z$.

2.4.2 Brunt - Väisälä frequency

The Brunt-Väisälä (or buoyancy) frequency N is a measure of the degree of stratification of the water column and is defined as follows. If a small particle of fluid of density $\rho(z)$, in a stably stratified flow, is displaced vertically upwards by a distance ζ, the density of the surrounding fluid is $\rho(z)+\zeta\,\partial\rho/\partial z$, so the net gravitational force on the particle is $g\zeta\,\partial\rho/\partial z$. This force is in a negative (downward) direction, since $\partial\rho/\partial z$ is negative. Applying Newton's second law:

$$\rho\frac{\partial^2\zeta}{\partial t^2} = g\frac{\partial\rho}{\partial z}\zeta$$

which is the equation of a particle moving in simple harmonic motion with an angular frequency of $N = \left(-\frac{g}{\rho}\frac{\partial\rho}{\partial z}\right)^{1/2}$ rad s^{-1}.

2.4.3 Richardson number

The Richardson number, which has several forms, is a measure of the stability of a stratified flow. The flux Richardson number is the ratio of the rate of working against buoyancy forces to shear production of TKE:

$$Rf = \frac{B}{P} = -\frac{g\overline{\rho'w'}}{\rho\overline{u'w'}(\partial u/\partial z)} \tag{2.12}$$

This form of the flux Richardson number requires measurement of the high frequency vertical velocity and density fluctuations. It is easier to measure the parameters used in the gradient (or local) Richardson number (Ri), which can be obtained from the equation for Rf as follows. Substituting in (2.12) from equations (2.9) and (2.11):

$$Rf = -\frac{gK_z(\partial\rho/\partial z)}{\rho N_z(\partial u/\partial z)^2} = \frac{K_z}{N_z}\frac{N^2}{(\partial u/\partial z)^2} = \frac{K_z}{N_z}Ri \tag{2.13}$$

where $Ri = \dfrac{N^2}{(\partial u/\partial z)^2}$

It was conjectured by Taylor (1931) and proved theoretically by Miles (1961) that the critical value of the Richardson number for stability of a shear flow in an incompressible fluid of variable density is that the Richardson number must exceed 0.25 everywhere in the flow. Later observations in the laboratory (Scotti and Corcos, 1972) and in the ocean (Eriksen, 1978) demonstrated that the Richardson number must be less than 0.25 for instability to occur. This does not mean that the flow will definitely be unstable when $Ri < 0.25$, but that this is a necessary but not sufficient condition for instability. When this occurs, the turbulent motions mix the water column, converting TKE to potential energy and the buoyancy term in the TKE equation (2.3) is negative. A value of Ri above the critical level indicates that turbulent motions producing vertical mixing of the water column are inhibited by stratification. A negative value of Ri indicates that both buoyancy and shear work to produce TKE; that is, that convective motions are present.

2.4.4 Tidal straining

The potential energy anomaly φ (in units of J m^{-3}) represents the amount of work required to mix a stratified water column (Simpson *et al.*, 1990), and is therefore a measure of the degree of stratification of the water column:

$$\varphi = \frac{1}{h}\int_0^h (\overline{\rho} - \rho(z))gz \; dz \tag{2.14}$$

where h is the depth of the water column and $\overline{\rho}$ is the mean density at a given time.

The rate of change of φ due to tidal straining and the estuarine circulation can then be calculated from the horizontal density gradient and the shear in the mean flow:

$$\left(\frac{\partial \varphi}{\partial t}\right)_{strain} = \frac{g}{h}\frac{\partial \rho}{\partial x}\int_0^h \left(u(z) - \hat{U}\right) z \; dz \tag{2.15}$$

where $\hat{U}$ is the depth mean velocity.

The tidal straining competes with two mixing terms, one due to the tides and the other due to wind effects (Simpson and Bowers, 1981). The tidal stirring term can be obtained from the rate of production of TKE by integrating the ADCP production estimates over the entire water column. The mean value of the TKE production rate

throughout the water column in W m^{-3} is obtained by dividing by the total depth of the water column. Hence:

$$(\partial\varphi/\partial t)_{stir} = \delta P_{total}/h$$

where P_{total} is the total rate of production of TKE integrated over the water column and δ is a term representing the efficiency of mixing.

An alternative way of estimating the tidal stirring term is from the mean flow data by making two assumptions: (a) that the Reynolds stress profile is linear, and (b) that a quadratic drag law $u_*^2 = C_D\hat{U}^2$ holds. The depth integral of the TKE production rate, $\int_0^h \tau\frac{\partial u}{\partial z}dz$, then yields the simple relationship: $P_{total} = C_D\rho\hat{U}^3$ (W m^{-2}). This gives the tidal stirring term:

$$(\partial\varphi/\partial t)_{stir} = \delta C_D\rho\hat{U}^3/h$$

The wind stirring term is given by:

$$(\partial\varphi/\partial t)_{wind} = \delta_s k_s \rho_s W^3/h$$

where δ_s is the efficiency of wind mixing, k_s is the surface drag coefficient, W is the wind speed and ρ_s is the density of air.

2.5 Turbulent Length Scales

Length scales can be defined for different parts of the spectrum described in section 2.3. The largest length scale defines the size of the eddies in which the TKE is produced from the mean flow, the smallest is the scale at which dissipation takes place at the high wavenumber end of the spectrum.

2.5.1 The Kolmogorov microscale

Since dissipation occurs at approximately the same rate as production of TKE, it follows that the dissipation rate is independent of the viscosity of the fluid. It is only the size of the eddies in which dissipation occurs which is determined by the viscosity. Kolmogorov (1941) hypothesised that the size of the dissipating eddies is uniquely determined by the dissipation ε and viscosity ν of the fluid. Hence, using

dimensional analysis he defined a lengthscale l_K at which dissipation occurs:

$$l_K = \left(\frac{\nu^3}{\varepsilon} \right)^{1/4}$$

2.5.2 The Ozmidov Scale

Stratification restricts the growth of turbulent eddies in the vertical direction, since the eddies must overcome buoyancy effects. Ozmidov (1965) argued that the maximum size of the eddies, l_o, depends only on the dissipation rate ε and the degree of stratification, represented by the buoyancy frequency N. Therefore, by dimensional analysis: $l_O = c\varepsilon^{1/2} N^{-3/2}$ where c is a dimensionless constant, assumed to be ~1. The dependence here on ε and therefore P, the rate of TKE production, indicates that for a given degree of stratification, more energetic turbulence is able to produce eddies which have a larger length scale.

Assuming the relationship $P \approx \varepsilon$, the Ozmidov scale can be defined using the rate of production of TKE: $l_O = \left(P/N^3 \right)^{1/2}$ (Stacey *et al.*, 1999b). The quantities used in the calculation of this length scale take no account of the depth of the water column, simply the rate of production of turbulent kinetic energy and the degree of stratification present. Hence at times when the length scale reaches its maximum values, at times of peak flow and minimum stratification, it may exceed the total depth of the water. This simply indicates that the vertical motions are not being restricted in any way by the stratification. The Ozmidov scale therefore provides a useful measure of the maximum size of the vertical overturns in stratified tidal flow (Stacey *et al.*, 1999b).

2.6 Summary

The parameters described in this chapter will be used to analyse turbulence measurements in stratified and unstratified flows. The Reynolds stress, TKE production rate, eddy viscosity and TKE will be calculated directly from the ADCP measurements. An estimate of the gradient Richardson number and Ozmidov scale in a stratified water column will also be calculated using ADCP and CTD measurements; their relationship to variations in the turbulent parameters will be examined in detail.

CHAPTER 3

The Acoustic Doppler Current Profiler and the Variance Method

Turbulence measurements in the atmosphere have been made since the 1960s using Doppler radar techniques (Lhermitte, 1968; Vincent and Reid, 1983; Rottger and Larsen, 1990). Until the 1980s, it was not possible to apply such methods in a marine environment, since radar cannot travel through water. With the subsequent development of high frequency acoustic Doppler current profilers, it became possible to apply some of the methods derived from the use of radar in meteorological studies to the study of oceanic turbulence, but using acoustic signals instead of radar.

3.1 The ADCP

The ADCP (Figure 3.1) measures velocity through the water column by transmitting and receiving pulses of sound (Figure 3.2). The ADCP used in this study, the RD Instruments Workhorse, has four transmitter-receivers arranged in a Janus configuration (Figure 3.1); the velocity along three orthogonal axes (two horizontal, one vertical) can be calculated from the measurements taken along each of the four beams.

The transmitted pulse is reflected by small particles which are assumed to be moving with the current and the received signal is Doppler shifted according to the velocity of the reflector. This gives an estimate of the along-beam velocity vector, calculated using $b_i = (\Delta f)C/(2f_0)$ where f_0 is the frequency of the emitted sound pulse, Δf is the shift in frequency of the signal at the receiver, b_i is the along-beam velocity component of the water and C is the speed of sound. After a time t, a pulse of duration T_P returns to the transmitter-receiver from a distance of between $Ct/2$ and $C(t+T_P)/2$. The returning signal is range-gated, that is, recorded at different times t after the emission of the pulse. The length of time Δt between consecutive recording times t defines the distance over which returning signals are averaged, which are termed depth cells. The minimum value of Δt which can be used is governed by the frequency; higher frequencies allowing smaller values of Δt to be used, since there are more cycles per unit time from which to take an average of the frequency shift.

The scatterers which reflect the acoustic signal from the ADCP are predominantly planktonic organisms with sizes of order one millimetre (RDI, 1996). Other scatterers include suspended sediments and detritus; discontinuities in water density also supply a relatively weak reflected signal. The surface and bottom are strong reflectors of the acoustic signal; this can be exploited to find the water depth from the ADCP backscatter strength in an upward-looking ADCP if the instrument does not have a pressure sensor (Visbeck and Fischer, 1995). A low density of scatterers may reduce the nominal range of the ADCP, since the strength of the reflected signal (the echo intensity in dB) is inversely proportional to the distance from the transducer (RDI, 1996).

The size of the depth cells is chosen in order to obtain a good compromise between accuracy and spatial resolution. Larger depth cells have a lower uncertainty associated with the velocity measurement, since the measured frequency shift is averaged over a greater length of time, thus removing more errors. However, the accuracy may be compromised by using a greater depth cell size, since the frequency shift is also being measured over a greater depth of the water column. In a flow with characteristics which change rapidly with depth this will have a significant effect on the results. The velocity recorded by the ADCP for a given depth cell is a weighted average of the velocity measurement in that depth cell and those adjacent to it. This can cause a correlation of the measured velocities in adjacent depth cells of about 15% (RDI, 1996).

A short period of time is normally required between the transmission of the acoustic pulse and the processing of the reflected signal. Some energy from the transmitted signal remains after the pulse has finished (RDI, 1996); this effect is called ringing, and would contaminate the reflected signal if the ADCP started recording as soon as the transmit pulse had finished. When the velocities are recorded, this ringing time becomes a blanking distance between the ADCP transducers and the first depth cell (0.5m in a 1.2MHz ADCP). Combined with the fact that the velocities are a weighted average over a vertical distance which is approximately twice the nominal depth cell size, this means that the centre of the first depth cell in a 1.2MHz ADCP using 0.5m depth cells is located at a distance of about 1m from the transducers.

Different modes of operation and instrument specifications can be chosen depending on the characteristics of the location and the information required. The range of the ADCP varies inversely with the frequency, since the acoustic signal from high frequency instruments is absorbed more quickly. In deep water, then, a lower frequency instrument is necessary if the entire water column is to be profiled. The advantage of using a high frequency instrument is that the uncertainty in each individual velocity measurement decreases with increasing ADCP frequency, so in shallow coastal waters a high frequency instrument may be used to obtain high quality measurements. Due to the increased accuracy of the measurements, it may also be possible to use smaller depth cells with high frequency ADCPs; the increased uncertainty resulting from smaller depth cells being offset by the decrease in the uncertainty due to the instrument frequency.

One recent development in ADCP technology has enabled higher resolution data to be obtained than were obtained in previous studies. A fast-pinging mode (RDI mode 12: RDI, 2002), measures velocities at up to 20Hz, compared to a maximum possible rate of 3Hz with the standard RDI mode 1 (RDI, 2002). The fast-pinging mode was used in the York River estuary observations, with a ping rate of 10Hz. As will be seen in section 3.4 and chapter 6, the fast-pinging mode decreases considerably the uncertainty in the estimates of Reynolds stress, and makes possible the detection of stresses in lower energy environments.

Figure 3.1: The Acoustic Doppler Current Profiler

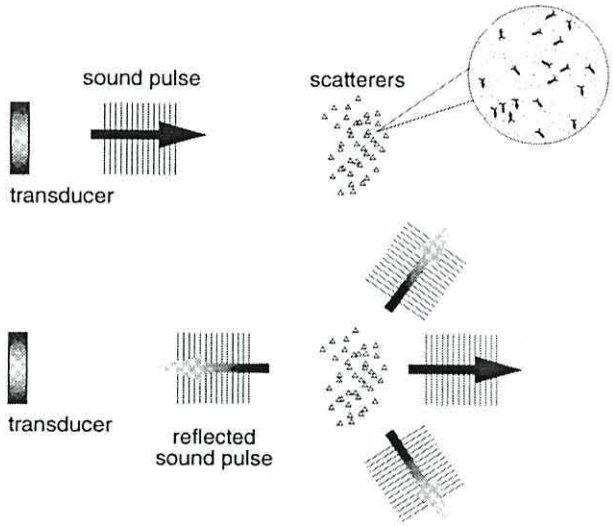

Figure 3.2: The ADCP emits a sound pulse which is reflected by scatterers in the water. (RDI, 1996)

3.2 Application of the variance method and its limitations

The method described here uses high frequency measurements of the along-beam velocities measured by the ADCP to estimate the Reynolds stresses, and hence the turbulent kinetic energy production rate, which is the product of the Reynolds stress and the shear in the mean flow. The ADCP's four beams measure the velocity of the flow at four different locations, separated by several metres. Since the beam separation may be larger than the size of the eddies, it is likely that the beams are each sampling different eddies at any given time (Stacey *et al.*, 1999a; Lu and Lueck, 1999a). This renders the direct correlation of the velocity fluctuations measured by two different beams meaningless. The data analysis method, therefore, uses only the statistical quantities (mean and variance) of the velocities measured along opposite beams, which means that there is an assumption that there is statistical homogeneity in the flow throughout the region under consideration.

3.2.1 Statistical Homogeneity

In order to estimate turbulent parameters, some assumptions must be made regarding the statistical homogeneity of the turbulence which are outlined by Lu and Lueck (1999a) and Stacey *et al.* (1999a). The method used for the calculation of the Reynolds stresses uses the assumption that the flow is statistically homogeneous in the horizontal plane over the distance of separation of the beams. Applying this assumption, the velocities measured by each beam can be separated into a mean and a fluctuating part and the variance for each beam can be calculated. The mean and variance of opposite beams can then be used to calculate the Reynolds stresses and the turbulent kinetic energy. The method of calculation is described in section 3.3.

If the beams are sampling from different eddies at any given time, this leads to another assumption (Tropea, 1983): the instantaneous velocity measurements from a beam are independent of those of another beam. Experimental work by Stacey *et al.* (1999a) confirmed this assumption since they found that the covariance between beams was more than an order of magnitude smaller than the variance of individual beams. It must also be assumed (Tropea, 1983) that the uncertainties in the along-beam measurements are the same for all beams. Again this was confirmed by Stacey *et al.* (1999a) from observations.

3.2.2 Temporal Stationarity

Since the mean and variance of the along-beam velocities are calculated over a period of several minutes, temporal stationarity must be assumed within that period (Stacey *et al.*, 1999a). It is therefore necessary to ensure that the time scale of the evolution of the flow is longer than the period over which the statistics are averaged, that is, there must be quasi-stationarity within the averaging period (Lohrmann *et al.*, 1990), but the time scale must be longer than that of the turbulent fluctuations (Hinze, 1959), in order to obtain statistically reliable estimates.

Averaging periods which have been used in previous studies are, for example, 10 minutes (Stacey *et al.,* 1999a; Rippeth *et al.*, 2002), 13.67 minutes (Lohrmann *et al.*, 1990) and 20 minutes (Lu and Lueck, 1999a, b). Analysis of stationarity periods in tidal flow indicates that the flow can usually be considered to be quasi-stationary for a period of between 8 and 12 minutes (Soulsby, 1980).

3.3 Data analysis methods

3.3.1 Calculation of the Reynolds stresses

The configuration of the ADCP beams is shown in Figure 3.3 and Figure 3.4. The method of calculating the Reynolds stresses uses the along beam velocities from pairs of opposite beams (beam 1 with beam 2; beam 3 with beam 4) , following the method of Lohrmann *et al.*, (1990). For each of the four beams, i =1,2,3,4, the velocity along beam i, b_i, can be split into mean and fluctuating components using the Reynolds decomposition:

$$b_i = \overline{b_i} + b_i' \tag{3.1}$$

The velocity along each beam can be written:

$$\begin{aligned} b_1 &= -u_1 \sin\theta - w_1 \cos\theta \\ b_2 &= u_2 \sin\theta - w_2 \cos\theta \\ b_3 &= -v_3 \sin\theta - w_3 \cos\theta \\ b_4 &= v_4 \sin\theta - w_4 \cos\theta \end{aligned} \tag{3.2}$$

where u_1, u_2, v_3, v_4, w_1, w_2, w_3, w_4 are the local horizontal and vertical velocity components along beams 1, 2, 3 and 4.

The mean horizontal velocity components are calculated as follows, assuming that the mean flow is homogeneous over the beam spread, that is, $\overline{u}_1 = \overline{u}_2 = \overline{u}$ and $\overline{v}_3 = \overline{v}_4 = \overline{v}$:

$$\overline{u} = \frac{\left(\overline{b}_2 - \overline{b}_1\right)}{2\sin\theta} \qquad \overline{v} = \frac{\left(\overline{b}_4 - \overline{b}_3\right)}{2\sin\theta} \tag{3.3}$$

Splitting the velocity along each beam given by equations (3.2) into a mean and a fluctuating part gives the fluctuating velocity components along each beam:

$$\begin{aligned} b_1' &= -u_1' \sin\theta - w_1' \cos\theta \\ b_2' &= u_2' \sin\theta - w_2' \cos\theta \\ b_3' &= -v_3' \sin\theta - w_3' \cos\theta \\ b_4' &= v_4' \sin\theta - w_4' \cos\theta \end{aligned} \tag{3.4}$$

Squaring each equation and taking a time average gives:

$$\begin{aligned} \overline{b_1'^2} &= \overline{u_1'^2}\sin^2\theta + 2\overline{u_1'w_1'}\sin\theta\cos\theta + \overline{w_1'^2}\cos^2\theta \\ \overline{b_2'^2} &= \overline{u_2'^2}\sin^2\theta - 2\overline{u_2'w_2'}\sin\theta\cos\theta + \overline{w_2'^2}\cos^2\theta \\ \overline{b_3'^2} &= \overline{v_3'^2}\sin^2\theta + 2\overline{v_3'w_3'}\sin\theta\cos\theta + \overline{w_3'^2}\cos^2\theta \\ \overline{b_4'^2} &= \overline{v_4'^2}\sin^2\theta - 2\overline{v_4'w_4'}\sin\theta\cos\theta + \overline{w_4'^2}\cos^2\theta \end{aligned} \tag{3.5}$$

For statistically homogeneous turbulence,

$$\begin{aligned} \overline{u_1'^2} &= \overline{u_2'^2} = \overline{u'^2} \\ \overline{v_3'^2} &= \overline{v_4'^2} = \overline{v'^2} \\ \overline{w_1'^2} &= \overline{w_2'^2} = \overline{w_3'^2} = \overline{w_4'^2} = \overline{w'^2} \\ \overline{u_1'w_1'} &= \overline{u_2'w_2'} = \overline{u'w'} \\ \overline{v_3'w_3'} &= \overline{v_4'w_4'} = \overline{v'w'} \end{aligned} \tag{3.6}$$

Subtracting pairs of equations (3.5) gives:

$$\begin{aligned} \overline{b_2'^2} - \overline{b_1'^2} &= -4\overline{u'w'}\sin\theta\cos\theta \\ \overline{b_4'^2} - \overline{b_3'^2} &= -4\overline{v'w'}\sin\theta\cos\theta \end{aligned} \tag{3.7}$$

Adding the pairs of equations gives:

$$\overline{b_1'^2} + \overline{b_2'^2} = 2\overline{u'^2}\sin^2\theta + 2\overline{w'^2}\cos^2\theta$$
$$\overline{b_3'^2} + \overline{b_4'^2} = 2\overline{v'^2}\sin^2\theta + 2\overline{w'^2}\cos^2\theta \qquad (3.8)$$

Rearranging equations (3.7) gives the Reynolds stresses:

$$-\overline{u'w'} = \frac{\overline{b_2'^2} - \overline{b_1'^2}}{4\sin\theta\cos\theta}$$
$$(3.9)$$
$$-\overline{v'w'} = \frac{\overline{b_4'^2} - \overline{b_3'^2}}{4\sin\theta\cos\theta}$$

The rate of production of TKE (P) can then be calculated using the equation:

$$P = -\overline{u'w'}\frac{\partial\overline{u}}{\partial z} - \overline{v'w'}\frac{\partial\overline{v}}{\partial z} \qquad (3.10)$$

The equations used to estimate the Reynolds stresses from the ADCP measurements assume no tilt in the head of the instrument. The effect of tilt on the Reynolds stress estimates is examined in detail in section 3.4.5.

There is not quite enough information available to calculate the turbulent kinetic energy density $q^2/2 = \left(\overline{u'^2} + \overline{v'^2} + \overline{w'^2}\right)/2$ (equation 2.1) since in the four equations (3.7) and (3.8) there are 5 unknowns, so a fifth equation is required. Two solutions to this problem are available. Firstly, Stacey *et al.* (1999b) calculated anisotropy ratios of the turbulent field using the results of Nezu and Nakagawa (1993) for vertical distributions of turbulence statistics assuming a local balance of production and dissipation:

$$\frac{\overline{v'^2}}{\overline{u'^2}} = 0.50 \qquad \frac{\overline{w'^2}}{\overline{u'^2}} = 0.30 \qquad (3.11)$$

Using equations (3.8) and (3.11) it is now possible to obtain two estimates for $q^2/2$. Alternatively, it has been suggested that an ADCP with a fifth, vertical beam could be

used (Lu and Lueck, 1999b). This would provide a direct measurement of the vertical velocity vector and its variance and hence produce a fifth equation which could be used to obtain an estimate of $q^2/2$. It would also help in the estimation of turbulent parameters in the presence of waves and in the resolution of problems arising from measurements made in the presence of non-zero tilt angles (Lohrmann *et al.*, 1990).

Using only the data available, and without making assumptions about the anisotropy of the flow, it is possible to obtain upper and lower bounds for the value of $q^2/2$ (Lohrmann *et al.*, 1990). If a parameter Q is defined, such that:

$$Q = \frac{1}{4\sin^2\theta}\sum_{i=1}^{4}\overline{b_i'^2} \tag{3.12}$$

Then it follows that:

$$\frac{3Q}{2\left(1+\cot^2\theta\right)} < \frac{q^2}{2} < Q$$

$$\frac{3}{8}\sum_{i=1}^{4}\overline{b_i'^2} < \frac{q^2}{2} < \frac{1}{4\sin^2\theta}\sum_{i=1}^{4}\overline{b_i'^2}$$

$\frac{3}{8}\sum\overline{b_i'^2}$ represents the minimum value of $q^2/2$ which occurs when the turbulence is close to isotropic; $\frac{1}{4\sin^2\theta}\sum\overline{b_i'^2}$ represents the maximum value of $q^2/2$ which occurs when the vertical motions have their minimum value.

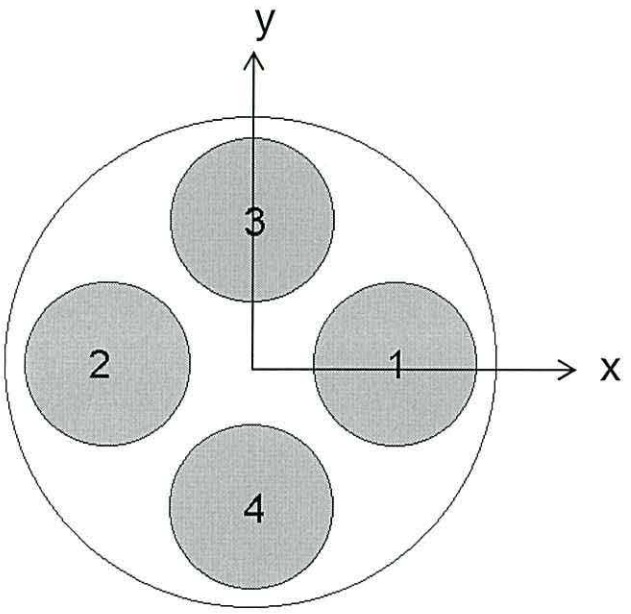

Figure 3.3: The configuration of the beams in the RDI Workhorse ADCP

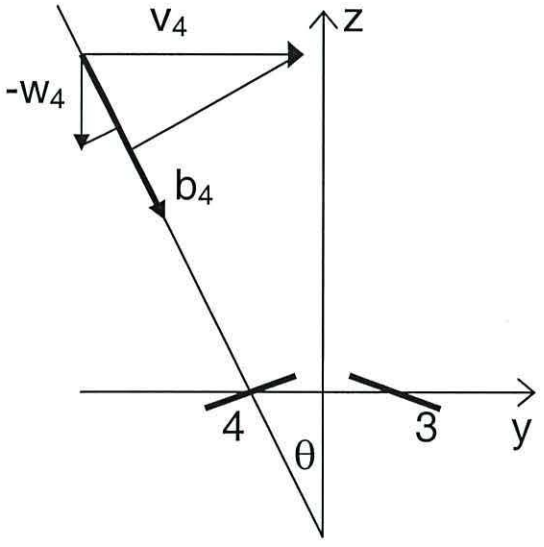

Figure 3.4: The configuration of the ADCP beams showing the along-beam velocity derived from the horizontal and vertical components of the flow

3.3.2 Rotation of velocities and Reynolds stresses from ADCP data

It is not always possible to deploy the ADCP such that a pair of beams is oriented in the direction of the mean flow. It will therefore usually be necessary to rotate the velocities and Reynolds stresses obtained from the two pairs of beams into components in the mean flow direction and perpendicular to the mean flow. Setting the direction of beam 1 as x_A, and the direction of beam 3 as y_A, the mean flow direction as x_R and the direction perpendicular to the mean flow as y_R, where x_R is positive in the flood (upstream) direction, the horizontal velocities in the mean flow direction and perpendicular to it can be calculated using the equations:

$$u_R = u_A \cos\theta_H - v_A \sin\theta_H$$
$$v_R = u_A \sin\theta_H + v_A \cos\theta_H$$

where u_A, v_A, u_R and v_R are the horizontal velocities in the x_A, y_A, x_R and y_R directions respectively and θ_H is the angle through which the x_A-axis must be rotated clockwise to coincide with the x_R-axis. The rotation of the co-ordinates is shown schematically in Figure 3.5.

The Reynolds stresses can be rotated to components in the mean flow direction and perpendicular to it, using the same method as that used for the velocities:

$$\frac{\tau_x}{\rho} = -\overline{u'w'}_R = -\overline{u'w'}\cos\theta_H + \overline{v'w'}\sin\theta_H$$

$$\frac{\tau_y}{\rho} = -\overline{v'w'}_R = -\overline{u'w'}\sin\theta_H - \overline{v'w'}\cos\theta_H$$

The sign convention used throughout is $\tau = -\rho\overline{u'w'}$, so that the Reynolds stress τ is positive on the flood.

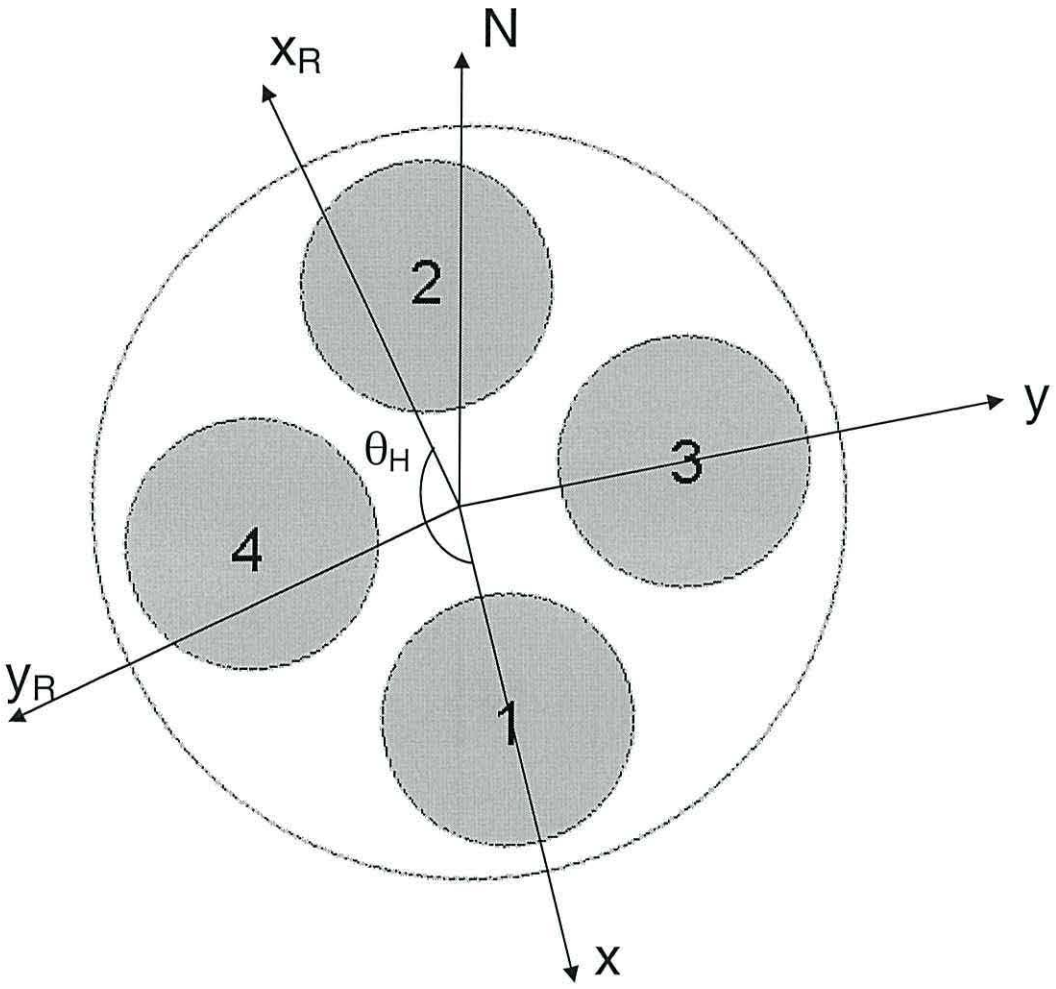

Figure 3.5: The rotation of the ADCP co-ordinates. The angle θ_H is the angle through which the x-axis (direction in which beam 1 is pointing) must be rotated clockwise to coincide with the x_R-axis (upstream, or flood direction).

3.4 Analysis of Uncertainties and Errors

3.4.1 Analysis of Uncertainties in Velocity Measurements

The velocity of a flow measured by an ADCP is subject to uncertainties which result from both instrument noise, which is present even if the true flow speed is zero and a flow-related uncertainty, which increases with the flow speed. The variation of the standard deviation of the velocity measurements in still water for different configurations is documented by the instrument manufacturers (RDI, 1996); a summary of the method by which this uncertainty is calculated by the instrument software is included in Appendix 2. The standard deviation increases from these values for non-zero flow speeds, but no indication is given in the information supplied by RDI of the effect of the flow speed on the standard deviation of the measured velocities. The uncertainty can, therefore, only be determined empirically.

The analyses presented in the following sections 3.4.2 to 3.4.4 consist of an extract from a published paper (Williams and Simpson, 2004).

3.4.2 Analysis of Uncertainties in Reynolds Stress Estimates

Since the uncertainties in the Reynolds stress estimates are due to uncertainties in the measured along-beam velocities, it is possible to calculate the former from the latter, although this requires some assumptions to be made about the statistical properties of the velocity fluctuations and the characteristics of the mean flow.

If the x axis is selected to be along the main direction of the flow, the variance of the principal Reynolds stress components, following Stacey *et al.* (1999a), is given by (see Appendix 3 for details of derivation):

$$Var\left(-\overline{u'w'}\right) = \sigma_R{}^2 = \frac{1}{16\sin^2\theta\cos^2\theta}\left[Var\left(\overline{b_2'^2} - \overline{b_1'^2}\right)\right] \tag{3.13}$$

The magnitude of the uncertainty can be calculated directly from the data if the components are rewritten as follows, using M ensembles to calculate the variances:

$$\sigma_R{}^2 = \frac{1}{16\sin^2\theta\cos^2\theta} Var\left(\frac{1}{M}\sum_{m=1}^{M} b_2'^2(m) - \frac{1}{M}\sum_{m=1}^{M} b_1'^2(m)\right) \tag{3.14}$$

This can be expanded to give (see Appendix 4 for details):

$$\sigma_R^{\,2} = \frac{\left[\sum_{i=1}^{2}\sum_{m=1}^{M} Var\left(b_i'^2(m)\right) + 2\sum_{i=1}^{2}\sum_{m=1}^{M-1}\sum_{n=m+1}^{M} Cov\left(b_i'^2(m), b_i'^2(n)\right) - 2\sum_{m=1}^{M}\sum_{n=1}^{M} Cov\left(b_1'^2(m), b_2'^2(n)\right)\right]}{16M^2 \sin^2\theta \cos^2\theta} \tag{3.15}$$

In the two data sets considered here, the last term on the right hand side of equation (3.15), representing the sum of the covariance of the squares of the fluctuations in opposite beams, was found to be an order of magnitude smaller than the first term, which represents the sum of the variances of the squares of the fluctuations in each of the two beams, hence the last term will be neglected. The second term represents the correlation between the square of each velocity fluctuation and subsequent measurements. This correlation can be expressed in terms of the normalized autocovariance function, ρ, given by:

$$\rho_i(m,n) = \frac{Cov\left[b_i'^2(m), b_i'^2(n)\right]}{\left[Var\left(b_i'^2(m)\right)\, Var\left(b_i'^2(n)\right)\right]^{1/2}}$$

In stationary flow, the correlation should be a constant for the period of the M ensembles used in the variance calculations, hence $Var\left[b_i'^2(m)\right] = Var\left[b_i'^2(n)\right]$ and $\rho(1,n) = \rho(m,m+n-1)$. An upper limit ($n = K$) can be defined, above which the covariance terms become negligibly small. K is small compared to M since the correlation effects of velocity fluctuations only extend over periods of the order of 20 seconds or less (Stacey et al. 1999a; Lu and Lueck, 1999b), so the sum of the covariances can be simplified (Heathershaw and Simpson, 1978):

$$\sum_{m=1}^{M-1}\sum_{n=m+1}^{M} Cov\left(b_i'^2(m), b_i'^2(n)\right) \approx M\sum_{n=2}^{K} Cov\left(b_i'^2(1), b_i'^2(n)\right) \tag{3.16}$$

The sum of the covariances for lags greater than zero is then given by:

$$\sum_{n=2}^{K} \rho_i(1,n) \approx \frac{\sum_{m=1}^{M-1}\sum_{n=m+1}^{M} Cov\left(b_i'^2(m), b_i'^2(n)\right)}{\sum_{m=1}^{M} Var\left(b_i'^2(m)\right)} \tag{3.17}$$

For large M, $(M-1)/M \rightarrow 1$, so equation (3.15) becomes:

$$\sigma_R{}^2 = \frac{\sum_{i=1}^{2}\sum_{m=1}^{M}\left[Var\left(b_i'^2(m)\right)\left(1+2\sum_{n=2}^{K}\rho_i(1,n)\right)\right]}{16M^2\sin^2\theta\cos^2\theta} \tag{3.18}$$

Using the stationarity condition,

$$\sum_{m=1}^{M} Var\left(b_i'^2(m)\right) = M\left(Var\left(b_i'^2\right)\right)$$

we can write:

$$\sigma_R{}^2 = \frac{\sum_{i=1}^{2}\left[Var\left(b_i'^2\right)\left(1+2\sum_{n=2}^{K}\rho_i(1,n)\right)\right]}{16M\sin^2\theta\cos^2\theta} = \frac{\gamma_R\left(Var\left(b_1'^2\right)+Var\left(b_2'^2\right)\right)}{16M\sin^2\theta\cos^2\theta} \tag{3.19}$$

where:

$$\gamma_R = 1+2\sum_{n=2}^{K}\rho(1,n) \tag{3.20}$$

The factor γ_R is therefore a correction factor to account for non-independence of consecutive measurements of velocity fluctuations. When adjacent velocity fluctuations are independent, the sum of the autocorrelations is zero, and $\gamma_R = 1$. Conversely, as adjacent velocity fluctuations become increasingly covariant, γ_R increases, with a consequent increase in σ_R which offsets the decrease in σ_R obtained through the increase in M. It is assumed here that the autocovariance time scales of the squares of the fluctuations, and hence the factor γ_R, are the same for two opposite beams.

In order to analyse the noise characteristics of the Reynolds stress estimates, a relationship between $Var\left(b_i'^2\right)$ and the along-beam velocity measurements is required. First we obtain an expression for $Var\left(b_i'^2\right)$ in terms of the second and fourth moments (μ_2 and μ_4 respectively) of the measured along-beam velocities:

$$Var\left(b_i'^2\right) = \frac{1}{M}\sum_{1}^{M}\left(b_i'^2 - \overline{b_i'^2}\right)^2 = \mu_4 - {\mu_2}^2 \tag{3.21}$$

If the distribution is Gaussian, then $\mu_4 = 3{\mu_2}^2$, hence:

$$Var\left(b_i'^2\right) = 2\left(\overline{b_i'^2}\right)^2 \tag{3.22}$$

This gives a value for the variance of the Reynolds stress estimates:

$${\sigma_R}^2 = \frac{\gamma_R\left[\left(\overline{b_1'^2}\right)^2 + \left(\overline{b_2'^2}\right)^2\right]}{2M\sin^2 2\theta} \tag{3.23}$$

The calculated along-beam variance comprises the true variance and the instrument noise (Stacey *et al.* 1999a):

$$\overline{b_i'^2} = \overline{\chi_i'^2} + {\sigma_N}^2 + Cov(\chi_i, b_N) \tag{3.24}$$

where $\overline{\chi_i'^2}$ is the variance of the along-beam velocity due to turbulent fluctuations, b_N is the uncertainty in the along-beam velocity measurements due to instrument noise and ${\sigma_N}^2$ is the variance of the along beam velocity due to instrument noise. Hence:

$${\sigma_R}^2 = \frac{\gamma_R\left[\left(\overline{\chi_1'^2} + {\sigma_N}^2 + Cov(\chi_1, b_N)\right)^2 + \left(\overline{\chi_2'^2} + {\sigma_N}^2 + Cov(\chi_2, b_N)\right)^2\right]}{2M\sin^2 2\theta} \tag{3.25}$$

As $\chi_i \to 0$ and $\overline{\chi_i'^2} \to 0$, ${\sigma_R}^2 \to \frac{\gamma_R {\sigma_N}^4}{M\sin^2 2\theta}$. If the variance is due to noise alone, there is no correlation between one measurement and the next and $\gamma_R = 1$, giving:

$${\sigma_R}^2 = \frac{{\sigma_N}^4}{M\sin^2 2\theta} \tag{3.26}$$

This sets the minimum measurable value of τ, which is dependent solely on the instrument noise.

The implications of equation (3.25) are as follows. For low flow situations, when the value of $\overline{\chi_i'^2}$ is small compared to ${\sigma_N}^2$, ${\sigma_R}^2$ can be lowered by reducing the instrument noise. Further reductions in ${\sigma_R}^2$ can be obtained if the number of

ensembles (M) used to calculate the variance is increased. For stronger flows, when $\overline{\chi_i'^2}$ dominates over $\sigma_N{}^2$, the only way in which $\sigma_R{}^2$ can be reduced appreciably, is to increase the value of M.

3.4.3 Uncertainty in Shear Estimates

The uncertainty in the estimate of the shear is readily obtained from the uncertainty in the velocity measurements. The variance in the shear is given by:

$$Var\left(\frac{\partial u_n}{\partial z}\right)=\frac{1}{(\Delta z)^2}Var(u_{n+1}-u_{n-1}) \tag{3.27}$$

where u is the horizontal velocity in the x-direction. The variance in the horizontal velocity $Var(u)$, is calculated using the instantaneous horizontal velocity obtained from two opposite beams, assuming the measured vertical velocity is the same in both beams:

$$u=\frac{(b_2-b_1)}{2\sin\theta} \tag{3.28}$$

Hence when M ensembles are used to obtain the final shear estimate, again incorporating a factor γ_S to account for the correlation between one shear estimate and the next, we have:

$$Var\left(\frac{\partial u_n}{\partial z}\right)=\sigma_S{}^2\cdot\frac{\gamma_S\left(Var\left(b_{2(n+1)}\cdot b_{1(n+1)}\cdot b_{2(n-1)}\cdot b_{1(n-1)}\right)\right)}{\cdot M\left(\cdot z\right)^2{}_{\cdot\cdot}{}^2\theta} \tag{3.29}$$

The assumption that the vertical velocity is the same in both beams will increase the calculated variance if the two vertical velocities are not the same, hence equation (3.29) will tend to overestimate the variance of the shear. It is readily seen from this equation that the uncertainty in the shear can be reduced by increasing the number of ensembles to be averaged. It can also be reduced by increasing the depth cell size, at the expense of the vertical resolution.

In still water, equation (3.29) can be used to find the uncertainty in the shear measurements due to instrument noise alone:

$$\sigma_S{}^2=\frac{\sigma_N{}^2}{M(\Delta z)^2\sin^2\theta} \tag{3.30}$$

3.4.4 Analysis of Uncertainties in TKE Production Rate Estimates

The uncertainty in the estimates of rate of shear production of TKE can be determined using the formula for the variance of a product (Goodman 1960). For two independent variables, this is:

$$Var(xy) = \bar{x}^2 Var(y) + \bar{y}^2 Var(x) + Var(x)Var(y)$$

So in terms of our present notation, where we are interested in the variance of $P = -\overline{u'w'}(\partial\bar{u}/\partial z)$:

$$\sigma_P{}^2 = \overline{u'w'}^2 \sigma_S{}^2 + \left(\frac{\partial\bar{u}}{\partial z}\right)^2 \sigma_R{}^2 + \sigma_R{}^2 \sigma_S{}^2 \tag{3.31}$$

For the low flow case, $\overline{u'w'} \to 0$ and $\frac{\partial\bar{u}}{\partial z} \to 0$, so it is expected that the last term will dominate. The other two terms are expected to dominate at times of higher flow. In chapter 6, the effect of the other two terms will be examined using data from the York River Estuary and the Menai Strait; strategies for reducing the uncertainties will also be discussed. A further discussion of the justification for assuming independence, and the derivation of the formula for the variance of a product is given in Appendix 5.

3.4.5 Errors due to tilt in the ADCP

A detailed derivation of the method of calculation of tilt errors is given in Appendix 6. These errors are given by (Lu and Lueck, 1999b):

$$-\overline{u'w'} = \frac{\overline{b_2'^2} - \overline{b_1'^2}}{2\sin 2\theta} + \psi_{12}\left(\overline{u'^2} - \overline{w'^2}\right) - \psi_{34}\overline{u'v'}$$

$$-\overline{v'w'} = \frac{\overline{b_4'^2} - \overline{b_3'^2}}{2\sin 2\theta} - \psi_{34}\left(\overline{v'^2} - \overline{w'^2}\right) + \psi_{12}\overline{u'v'} \tag{3.32}$$

where: ψ_{12} = ADCP roll (beam 2 higher than beam 1) and ψ_{34} = ADCP pitch (beam 3 higher than beam 4). The angles ψ_{12} and ψ_{34} are measured in radians.

In the case of a four-beam ADCP, as used in the present study, no method exists for estimating the true value of the terms containing $\overline{u'v'}$. Lohrmann *et al.* (1990) state

that the correlation terms $-\psi_{34}\overline{u'v'}$ and $\psi_{12}\overline{u'v'}$ can be ignored if the tilt angles are less than $\pm 8°$ (or ~ 0.14 radians), since $\overline{u'v'}$ is usually smaller than the Reynolds stresses $-\overline{u'w'}$ and $-\overline{v'w'}$, and even if $\overline{u'v'}$ were of the same order as the Reynolds stresses, the contribution of these terms would be small. However, for strongly anisotropic turbulence, it has been suggested that these terms could produce a significant bias (Lu and Lueck, 1999b).

The amount of error due to the terms involving the differences of the variances, $\psi_{12}\left(\overline{u'^2} - \overline{w'^2}\right)$ and $\psi_{34}\left(\overline{v'^2} - \overline{w'^2}\right)$ can be estimated using some assumptions about the anisotropy of the flow. For steady, unstratified flow in an open channel, and assuming a local balance of production and dissipation, the variances can be defined in terms of the friction velocity (Nezu and Nakagawa, 1993):

$$\begin{aligned}\overline{u'^2} &= 5.29u_*^2 \exp\left(-2\frac{z}{H}\right)\\ \overline{v'^2} &= 2.66u_*^2 \exp\left(-2\frac{z}{H}\right)\\ \overline{w'^2} &= 1.61u_*^2 \exp\left(-2\frac{z}{H}\right)\end{aligned} \tag{3.33}$$

Hence, near the bed, where $u_*^2 \approx \left|\overline{u'w'}\right|$ and z ≈ 0, the differences in the variances in the along-channel and cross-channel directions are given by:

$$\begin{aligned}\overline{u'^2} - \overline{w'^2} &= 3.68\overline{u'w'}\\ \overline{v'^2} - \overline{w'^2} &= 1.05\overline{u'w'}\end{aligned} \tag{3.34}$$

This indicates that the difference of the horizontal and vertical variances can be expected to be greater than the Reynolds stresses. Therefore, even when the tilt angle (ψ_{12} or ψ_{34}) is small, the value of $\psi_{12}\left(\overline{u'^2} - \overline{w'^2}\right)$ is significant; about 6.4% of $\overline{u'w'}$ per degree of tilt. This estimate is supported by those from other studies: Lu and Lueck (1999b) estimate that the error due to $\psi_{12}\left(\overline{u'^2} - \overline{w'^2}\right)$ is a maximum of $0.17\overline{u'w'}$ for $\psi_{12} = 2°$. Heathershaw (1976) estimated Reynolds stresses from measurements made using electromagnetic current meters. For small errors (< 5°) in the alignment of the sensors with the plane of the measured components, he estimated that there would be an error of the order 10% per degree of misalignment.

3.4.6 Errors due to waves

Equations for the bias due to waves can be obtained using the tilt data in a similar manner to the derivations of equations (3.32). The equations for each component of velocity, u_i, can be rewritten to include variations due to wave action: $u_i = \overline{u} + \tilde{u} + u'$ where $\overline{u}$ = mean velocity, $\tilde{u}$ = wave induced velocity fluctuation, u' = turbulent fluctuation.

If it is assumed that the turbulent and wave-induced fluctuations are uncorrelated, then all terms $\overline{u_i'\tilde{u}_j} = 0$ for any i and j (Trowbridge, 1998). Hence the terms for wave bias are similar to the terms for tilt errors, and appear as extra terms in the equations for the Reynolds stress estimates:

$$-\overline{u'w'} = \frac{\overline{b_2'^2} - \overline{b_1'^2}}{2\sin 2\theta} + \psi_{12}\left(\overline{u'^2} - \overline{w'^2}\right) - \psi_{34}\overline{u'v'} + \overline{\tilde{u}\tilde{w}} + \psi_{12}\left(\overline{\tilde{u}^2} - \overline{\tilde{w}^2}\right) - \psi_{34}\overline{\tilde{u}\tilde{v}}$$

$$-\overline{v'w'} = \frac{\overline{b_4'^2} - \overline{b_3'^2}}{2\sin 2\theta} - \psi_{34}\left(\overline{v'^2} - \overline{w'^2}\right) + \psi_{12}\overline{u'v'} + \overline{\tilde{v}\tilde{w}} - \psi_{34}\left(\overline{\tilde{v}^2} - \overline{\tilde{w}^2}\right) + \psi_{12}\overline{\tilde{u}\tilde{v}}$$

An order of magnitude estimate can be obtained for each of the wave-induced terms in the Reynolds stress equations (Trowbridge, 1998).

For small tilt angles: $\psi_{12}, \psi_{34} = \mathrm{O}\ (10^{-2}\ \text{radians})$

Typical shelf sea values are: $\overline{\tilde{v}^2} = \mathrm{O}\left(\overline{\tilde{u}\tilde{v}}\right) = \mathrm{O}\ (10^{-1}\ \mathrm{m^2 s^{-2}})$

$\partial h/\partial x = \mathrm{O}\ \left(\partial h/\partial y\right) = \mathrm{O}\ (10^{-2})$

where h is the water depth. The kinematic boundary condition at the bed requires that $\overline{\tilde{v}\tilde{w}} \approx -\left(\partial h/\partial x\right)\overline{\tilde{u}\tilde{v}} - \left(\partial h/\partial y\right)\overline{\tilde{v}^2}$

Using these estimates, the magnitude of the wave-induced terms is O (10^{-3} $\mathrm{m^2 s^{-2}}$). Improved estimates of the wave-induced terms $\overline{\tilde{u}_i\tilde{u}_j}$ can be obtained using the equations for particle orbits in forward-travelling waves; when combined with the observed wavenumber, frequency and amplitude of the waves, the bias due to waves can be estimated (Rippeth *et al.*, 2003).

3.5 Summary

Measurements of turbulent parameters such as Reynolds stress, TKE production rate and eddy viscosity can be made from the application of the variance method to the along-beam velocities of a moored ADCP. A method for calculating the magnitude of the uncertainties in such measurements has been outlined; this method will be applied to the data from the York River estuary in chapter 6. Whilst it is possible to quantify the uncertainties due to instrument noise, the bias due to misalignment of the nominal vertical of the ADCP with the local normal to the mean flow cannot be accurately estimated without some knowledge of the anisotropy of the flow. Similarly, measurements of wavelength, frequency and amplitude of surface waves are required if accurate estimates of the bias due to these waves are to be obtained.

CHAPTER 4

The York River Estuary: Results

The York River estuary is a partially stratified estuary, which tends to stratify at neaps but often experiences complete vertical mixing during springs. The strong horizontal density gradient between the freshwater input at the head of the estuary and the point at which it discharges into Chesapeake Bay indicates that tidal straining is expected to have a significant effect on the cycle of turbulence and mixing along the estuary. It was therefore hoped that the data collected would yield useful information regarding the cycle of turbulence and stratification in the estuary, and the part played in this cycle by the tidal straining mechanism. The timing of the observations, in March and April, was chosen to coincide with the time of year when the horizontal density gradient was expected to be at its strongest, after the snow had melted and increased the freshwater input to the estuary.

The School of Ocean Sciences at the University of Wales, Bangor has strong links with the Virginia Institute of Marine Science (VIMS), whose laboratories are located at Gloucester Point, where the York River estuary meets Chesapeake Bay. This campaign therefore represented a useful opportunity for a collaborative study with the object of obtaining observations of the dynamics of the estuary over a spring-neap cycle.

4.1 Instruments, Methods and Location

The position and depth details of the instruments used are given in Table 4.1; the instrument layout is shown in Figure 4.1 and Figure 4.2. The ADCPs and the tripod on which the ADV was mounted were located at the main study site at Clay Bank, shown in detail in the lower plot in Figure 4.2 (note that chart depths in this figure are in feet). One S4 current meter mooring was also deployed at Clay Bank, the other about 6.8 km upstream. The *RV Langley* was used to take hourly conductivity-temperature-depth (CTD) profiles at approximately half-hourly intervals during two intensive periods of study. The vessel was anchored fore and aft approximately mid-way between the two ADCPs and close to the ADV tripod. Tide gauges were situated at Clay Bank, Gloucester Point (south) and Taskinas Creek (north). The calibration and processing of the data from the S4 current meter moorings, the CTD, the ADV

and the tide gauges at Taskinas Creek and Clay Bank were carried out by personnel from the Virginia Institute of Marine Science.

The ADCPs were deployed over a spring-neap cycle, a total of approximately 16 days. There were two short breaks in the data of a few hours when the instruments were removed from the water for downloading of the data. The breaks were necessary because of the large memory requirements for such an intensive data set. The observation period for each instrument is shown in Figure 4.3(a) along with the surface elevation record from the Taskinas Creek tide gauge, located 12.8 km upstream from the location of the 1.2MHz ADCP. The first intensive study period, in which the *RV Langley* was used to make CTD measurements close to the site of the ADCPs, lasted just under 24 hours and took place close to the neap tide. This study period had been planned to extend over 48 hours, but was terminated prematurely due to the arrival of a storm, which forced the *RV Langley* to move from her anchored position. The second intensive period extended to a full 48 hours and took place around the time of the spring tide.

The ADCPs were, in each case, set up to record ensembles composed of 10 sub-pings which were averaged by the instruments' software to give one along-beam velocity measurement every second. The depth cell size was 0.5m, with a blanking interval of 0.44m for the 1.2 MHz ADCP and 0.88m for the 600 kHz. The blanking distances used are the default values for these instruments, set by the RDI software, and are designed to ensure that the first depth cell (closest to the ADCP transducer) will record usable data. The lowest depth cell was therefore centred at 1.3m above the bed in the case of the 1.2 MHz, and 1.8m above the bed in the case of the 600 kHz. The ADCPs were moored on the bed in pyramid frames; the frame used for the 600 kHz ADCP (Figure 4.4) had a gimballed mounting for the instrument, the one used for the 1.2 MHz did not. The purpose of the use of two ADCPs was twofold: one was in order that there should be continuous data, should one ADCP fail. The other was to attempt to obtain continuous data, when allowing for the removal of the ADCPs at different times for downloading and replacement of batteries.

In practice, the 600 kHz ADCP only recorded good data for one of its three deployments; the others were compromised by tilt effects. Additionally, the 1.2 MHz

ADCP was overturned when the anchors were recovered on the RV Langley at the end of the second intensive period. This meant that the continuity of data was broken for two periods of approximately 5 hours on day 84 and 7 hours on day 90, and the only data for the 61 hours from day 87 at 20:44 to day 90 at 9:58 was from the 600 kHz ADCP. The overlap of 15 hours in the times of deployment of the 600 kHz and 1.2 MHz ADCPs on day 87 enables direct comparisons of data quality from the two instruments to be made.

The Sontek ADV was mounted on a tripod moored on the bed. It was set to record the three orthogonal components of velocity at 1.12 m above the bed for a 5-minute burst every hour with sampling rate of 5Hz. The data from the ADV will be used in this study to compare the Reynolds stress calculated from directly measured velocity fluctuations with those estimated from the ADCP using the variance method.

The two S4 current meter moorings, were set to record conductivity, temperature and current velocity data at 3m and 6m above the bed. 10-minute mean values were recorded every 30 minutes throughout the observation period. Unfortunately, the near-bed instrument on the mooring at Clay Bank failed, so only the surface salinity and temperature record was available for the calculation of the horizontal density gradient.

The three tide gauges, at Taskinas Creek (upstream), Gloucester Point (downstream) and Clay Bank (adjacent to the main observation site), recorded water levels throughout the period of the observations. However, there was a short period between days 81 and 85 when the water level at Clay Bank fell below expected levels due to high atmospheric pressure, resulting in data from this tide gauge for this period not being available.

Additional data of wind speed and direction and river discharge were also available. The wind data are from the VIMS meteorological station on the main campus at Gloucester Point. Wind data from the airport at Newport News, approximately 20 km south of Gloucester Point, on the James river, were used to check the VIMS data. No significant discrepancies were found between the two data sets. The river discharge data were collected by the US Geological Survey and represent the daily mean

discharge from the Mattaponi and Pamunkey rivers, the two main tributaries of the York river; the northernmost end of the York river estuary is the confluence of these two rivers. The wind and discharge records are shown in Figure 4.3 (b) and (c). The winds were generally light (< 8 m s^{-1}), apart from the period of very strong winds on days 79-80, when the wind speeds reached about 12 m s^{-1} and the first intensive period was terminated. Some heavy rainfall early in March 2002 had increased the runoff to a similar level to that seen during the storm of days 79-80 for several days, which might be expected to increase the stratification observed at the start of the campaign.

Table 4.1: Instrument locations for the York River observations

Instrument	Latitude	Longitude	Mean Depth (m)	Distance from 1.2MHz ADCP
1.2 MHz ADCP	37° 20.24′ N	76° 36.47′ W	6.5	
600 kHz ADCP	37° 20.15′ N	76° 36.42′ W	7.5	178 m downstream
ADV	37° 20.19′N	76° 36.48′W	5.0	95 m downstream
S4 mooring	37° 20.23′N	76° 36.50′W	6.7	45 m downstream
S4 mooring	37° 23.08′N	76° 39.45′W	6.4	6.8 km upstream
RV Langley	37°20.20′N	76°36.44′W	7.0	89 m downstream
Tide Gauge	37°24.90′N	76°42.86′W		12.7 km upstream
Tide Gauge	37°14.70′N	76°30.00′W		14 km downstream
Tide Gauge	37°20.86′N	76°36.63′W		1.18 km upstream

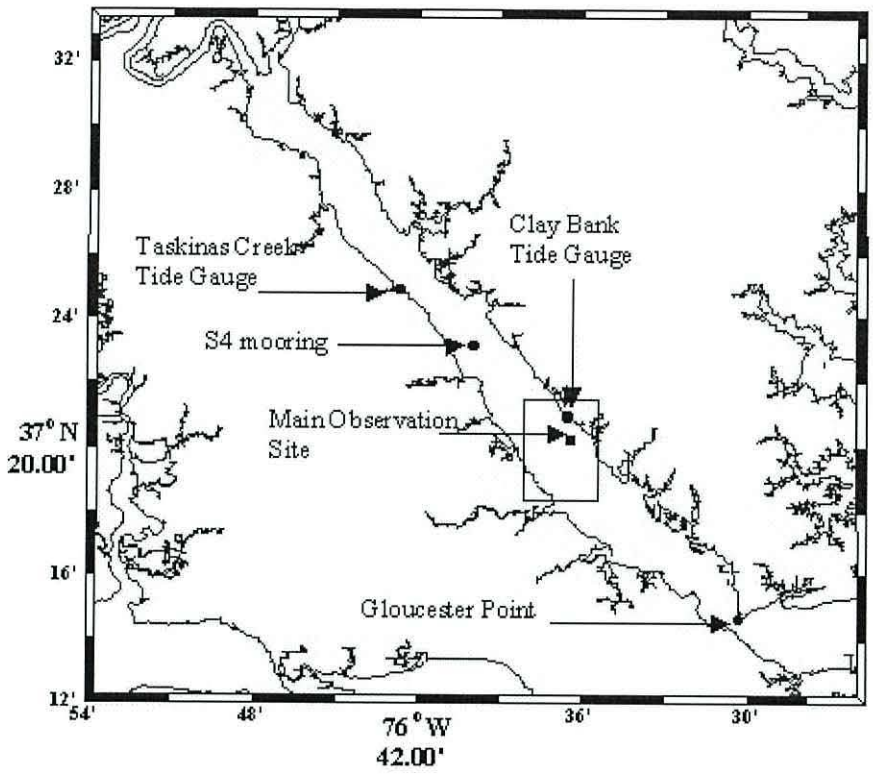

Figure 4.1: Location of instruments in the York River Estuary observations. At the location marked 'Main Observation Site' were moored the two ADCPs and the tripod on which the ADVs were mounted. The RV Langley, which was used to obtain the CTD measurements during the two intensive periods, was also located at this point. The rectangle around the site shows the extent of the map in Figure 4.2.

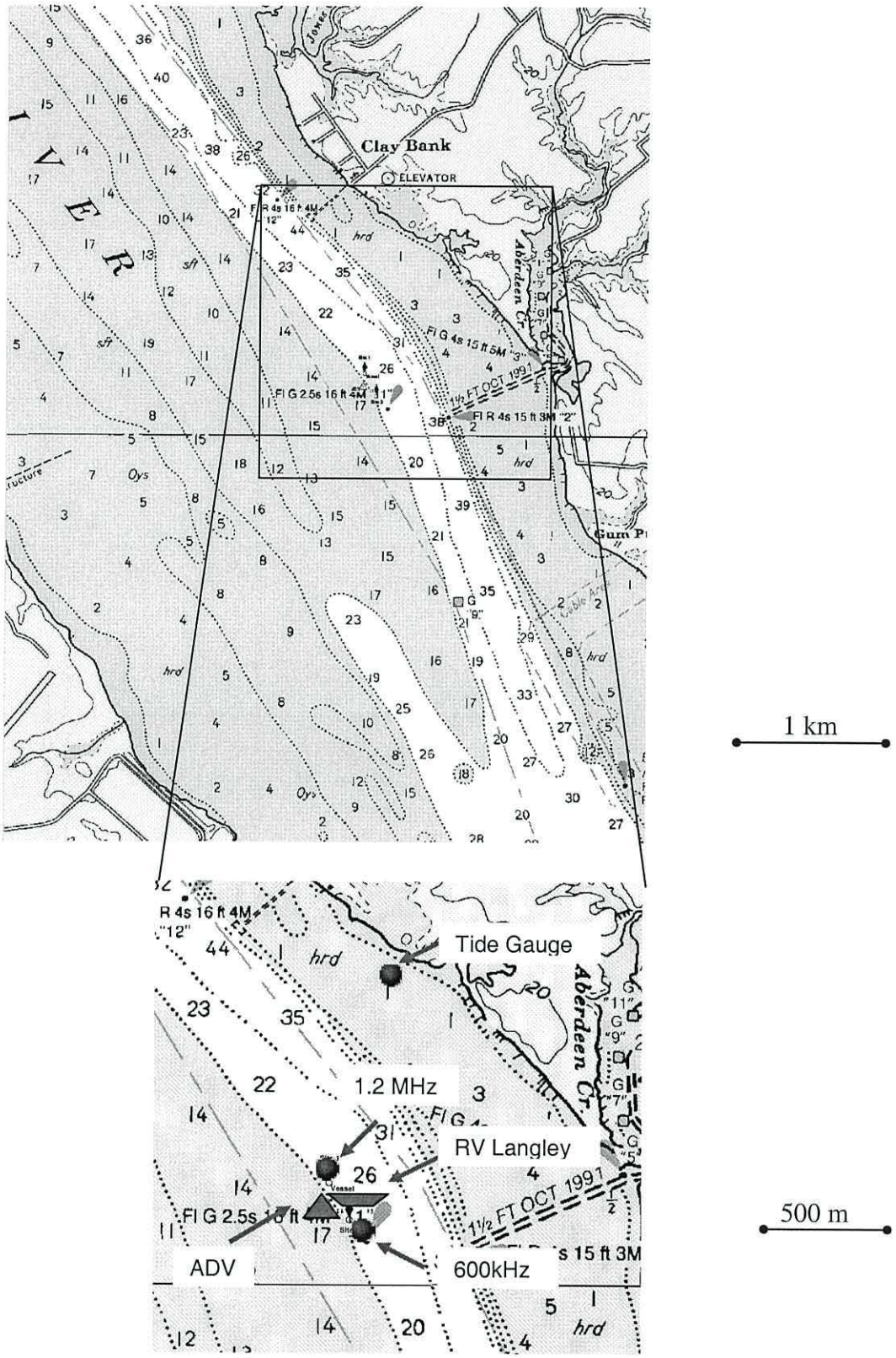

Figure 4.2: Map showing bathymetry of the observation site at Clay Bank and location of the two ADCPs, the ADV, the RV Langley and the adjacent tide gauge. All depths are in feet.

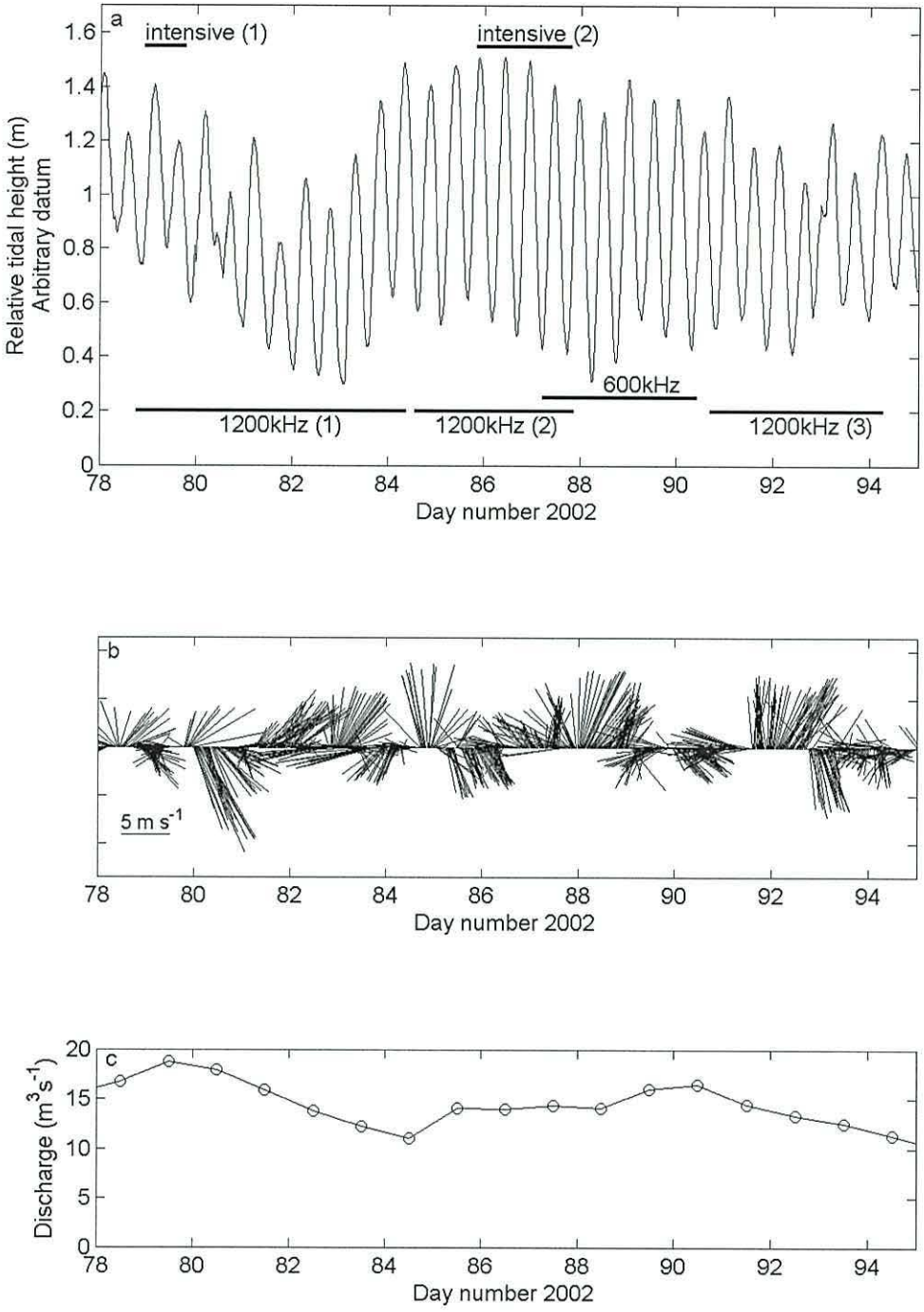

Figure 4.3: Observation Period in the York River Estuary showing (a) the relative tidal height, (b) the wind speed and direction at Gloucester Point: a stick pointing vertically upwards represents wind blowing towards north and (c) the combined discharge from the Mattaponi and Pamunkey rivers (daily mean).

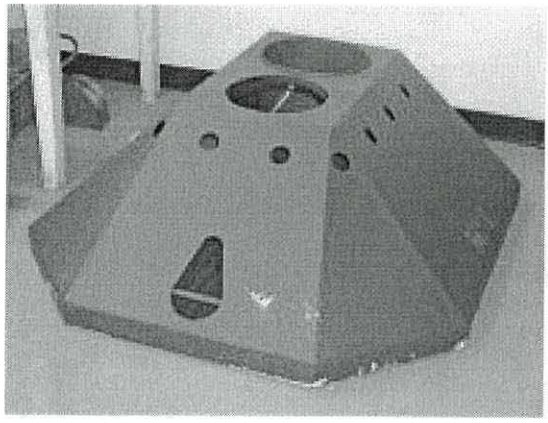

Figure 4.4: The mooring used for the deployment of the 600 kHz ADCP. The ADCP is mounted in one of the large holes on the top, using a gimballed mount.

4.2 Data Analysis

The mean horizontal velocities were obtained from the ADCP data by averaging over a 10-minute period. When rotating the co-ordinate system as described in section 3.3.2, the main direction of flow was estimated from the whole ADCP record as the mean direction at peak flood and peak ebb, and was assumed to be constant.

The Reynolds stresses were obtained from the ADCP along-beam velocities using equation 3.9 (chapter 3). Before this calculation was made, the data were first filtered in order to remove any spurious high fluctuations, which could have a great effect on the estimated Reynolds stresses and the other parameters to be calculated. This was achieved by fitting a third order polynomial to each 10-minute block of data. The fluctuations were then calculated as the deviations from the value of the polynomial at each time step, and the standard deviation calculated. Any fluctuations which had a magnitude greater than three standard deviations from the line were discarded. The variances of the remaining data points were used to calculate the Reynolds stresses. When the Reynolds stresses were calculated without the initial filtering, they differed little from those calculated from the filtered data, indicating high data quality as well as stationarity of the mean flow over the 10-minute averaging period. A further check on the stationarity over the 10-minute averaging period was made by using a run test (Bendat and Piersol, 1971), which indicated that the flow was quasi-stationary except for short periods at slack water, when high accelerations were present.

4.2.1 Overview of data

The surface elevation at the 1.2MHz ADCP is plotted in panel (a) of Figure 4.5, along with (b) the along-channel velocity, (c) Reynolds stress (τ), (d) the rate of production of TKE (P) and (e) a parameter Q related to the TKE $q^2/2$ (see equation 3.12) for the entire period of the ADCP deployments. The velocity, τ and P are shown for 1.8m above the bed, and Q for 4.8m above the bed. Q is proportional to q^2 and indicates the cycle of TKE over the period of the observations. It should be noted here that the cycle of Q can only be considered to be accurate if it is assumed that the anisotropy is constant at all heights above the bed and over the tidal cycle.

In panels (a) to (d), the variation over the spring-neap cycle is apparent: the lowest values are seen around day 80 and the highest around day 87. At neaps, although the velocity is well resolved, τ and P are so small as to be almost indistinguishable from noise on this scale; at springs, the tidal elevation, velocity, stress and production rate all show a clear semi-diurnal tidal variation. This is less clear in the time series of Q, but the strong wind event on day 80 (see Figure 4.3(b)), which has very little effect on the mean velocity, and only slightly more on the Reynolds stress, has a very marked effect on Q. This effect will be examined in detail in section 4.4. For days 88-90, the only ADCP data obtained were from the 600 kHz ADCP. Although the same sampling rate, depth cell size and averaging period were used in both the 600 kHz and the 1.2 MHz ADCPs, there is a much greater uncertainty in all parameters other than the mean velocity in the lower frequency instrument. In panel (e), which is calculated from the sum of the variances, there is a bias in the values; the lowest value of Q from the 600 kHz ADCP is 0.016 $m^2 s^{-2}$ compared with 0.0024 $m^2 s^{-2}$ from the 1.2 MHz. The higher uncertainty can also be seen in panels (c) and (d) as a noisier signal in both τ and P, as well as a greater tendency to negative values of P. The negative values are due mainly to the higher uncertainties in the velocity measurements in lower frequency instruments. However, in this deployment, additional measurement errors may be due to the ADCP being tilted at a greater angle than in any of the 1.2 MHz ADCP deployments; the higher tilt angle tends to induce higher errors in the Reynolds stress estimates in the form of a bias, and therefore also in the TKE production rate and eddy viscosity (see section 3.4.5 and Appendix 6).

The times at which the detailed observations of the density structure were made are labelled (1) and (2) in Figure 4.5. The interaction of the velocity, Reynolds stress, TKE production rate and eddy viscosity with the density structure during these periods will be analysed in more detail in section 4.3.

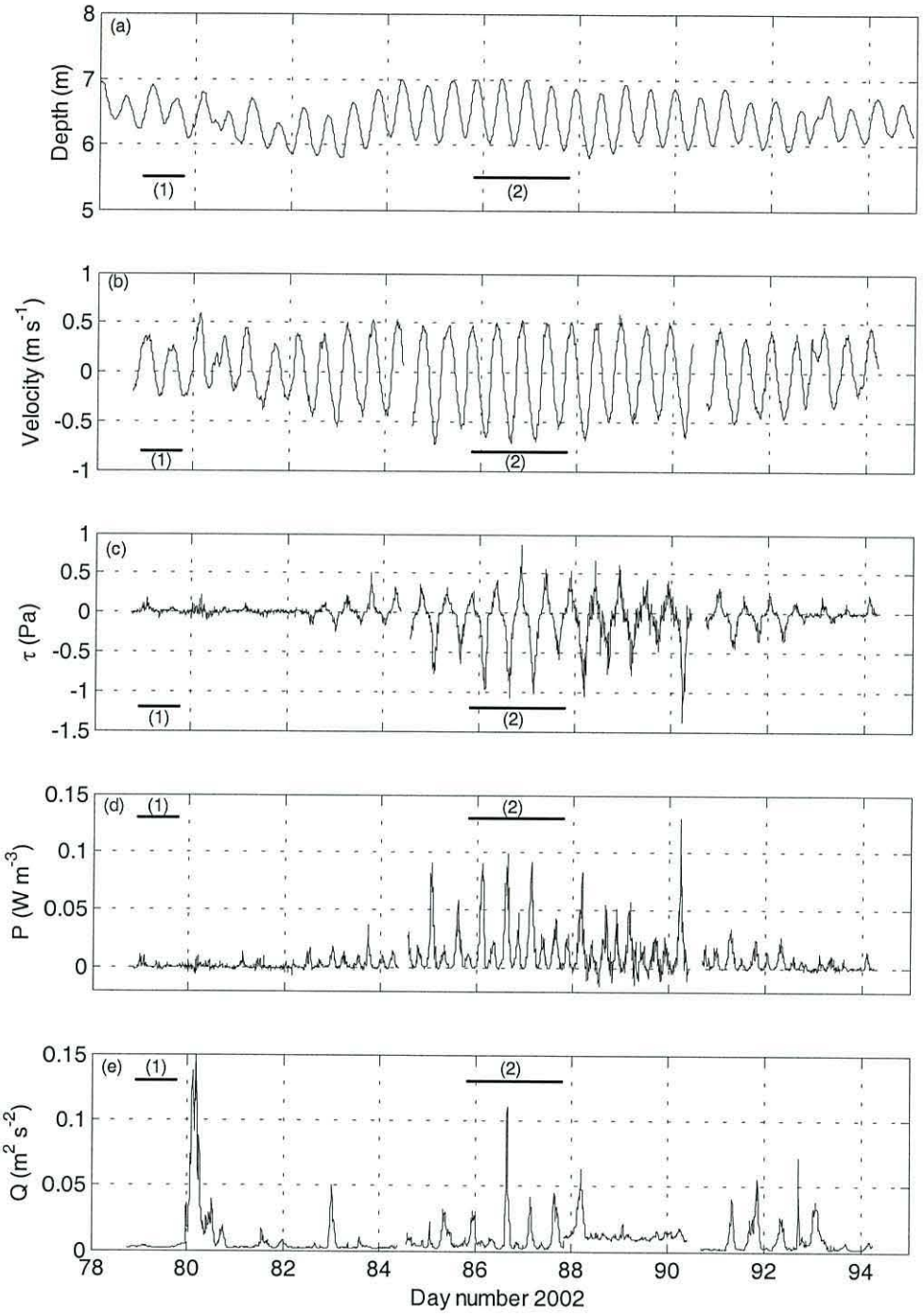

Figure 4.5: Overview of results from York River observations: (a) Depth at 1.2MHz ADCP estimated from the tide gauge at Taskinas Creek, (b) Along channel velocity (ms^{-1}), (c) Reynolds stress (Pa) and (d) TKE production rate (Wm^{-3}) at 1.8m above the bed, (e) the parameter Q ($m^2\ s^{-2}$), which is proportional to the TKE per unit mass ($q^2/2$) at 4.8m above the bed. 10-minute averaging was used for panels (b) to (e). The two periods at which detailed observations of the density structure were obtained are marked (1) and (2) on each panel.

4.2.2 Comparison of data from ADCP and ADV

The Reynolds stresses were calculated directly from the ADV measurements, which made possible a comparison with those estimated from the ADCP. The ADV measured the three orthogonal velocity components at 1.12 m above the bed at a distance of 175 m downstream from the ADCP. A comparison of Reynolds stresses from the two instruments is shown in Figure 4.6 for the springs deployment of the 1.2MHz ADCP. In general there is good agreement; the linear regression shown as a solid line indicates a correlation coefficient R^2 of 0.89 (77 degrees of freedom). The gradient of the regression line is 0.747 ± 0.059 with an intercept of -0.035; this gradient indicates that the stress estimated by the ADCP is only about 75% of that estimated from the ADV data. Forcing the regression line through the origin makes little difference; the gradient of the line is then 0.762. It is possible that the stress is underestimated by the ADCP due to the relatively large spatial averaging which is used. For a depth cell centred at 1.3 m above the bed, the ADCP calculates the velocities using a weighted average of the velocities measured between 0.8 m and 1.8 m above the bed. If there is a great deal of shear in the water column in this region, it is not certain that the velocity and hence the stress in this depth cell is representative of the true stress at 1.3 m above the bed, which may also be significantly different from the stress at the point of measurement of the ADV at 1.12 m above the bed.

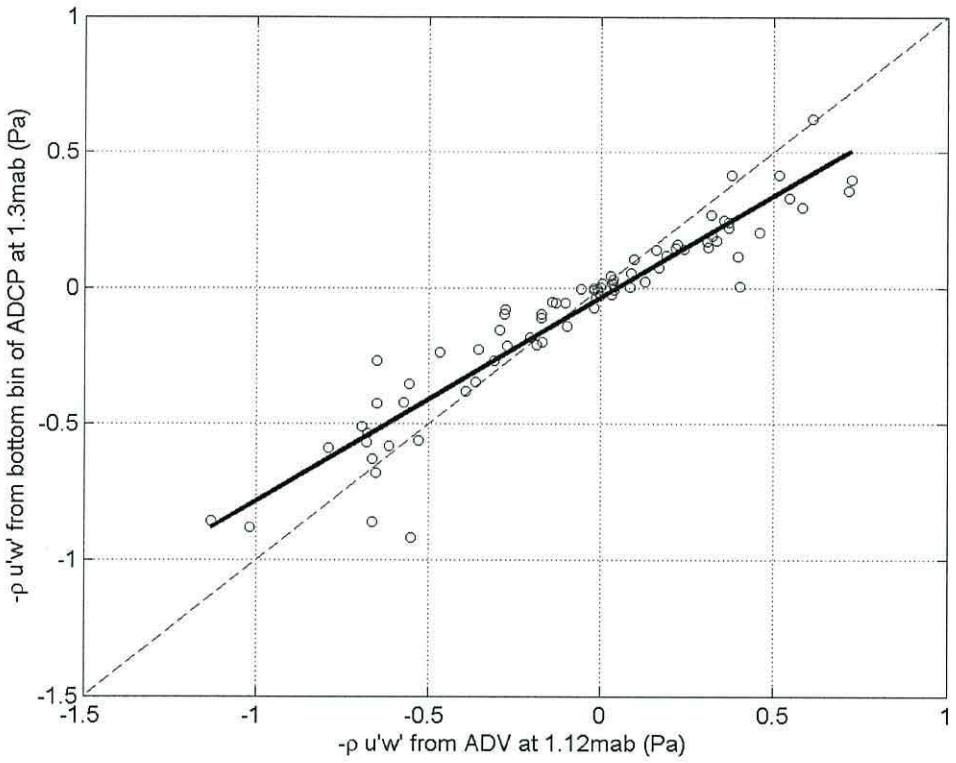

Figure 4.6: The estimated Reynolds stress from the 1.2 MHz ADCP plotted against τ from the ADV for the second deployment of the 1.2 MHz ADCP at springs. The solid line shows the regression of τ from the ADCP on τ from the ADV. The dashed line shows equality of the two estimated values of τ.

4.3 Structure of the Water Column

4.3.1 Density Profiles

CTD profiles were made during the two short periods of about 24 hours at neaps and 48 hours at springs. Due to a problem with the instrument, data from the first 16 hours of the springs period are not considered reliable, hence those data are disregarded and only the final 32 hours used.

The density profiles are shown in Figure 4.7 and Figure 4.8 for the spring and neap intensive periods respectively. During both neap and spring periods, the thermal stratification is weak, with only a small amount of solar heating seen during the latter part of each day (day number 79.6 in Figure 4.7; day numbers 86.8 and 87.6 in Figure 4.8). During the flood, the influx of colder water from Chesapeake Bay cools the entire water column (day number 79.2 (Figure 4.7); 87.1 and 87.4 in (Figure 4.8)).

In the cases of both neap and spring periods, the haline stratification increases towards the end of the ebb (day numbers 78.9 and 79.4 in Figure 4.7; 86.7, 87.25 and 87.75 in Figure 4.8). The stratification during the neap period is much stronger than during the spring tidal period, with a difference in salinity of over two between top and bottom at day number 79.4 (Figure 4.7) compared with a maximum top-bottom salinity difference of only one during the spring tidal period (day numbers 86.8, 87.3 and 87.7 (Figure 4.8)). The salinity structure is also strongly affected by tidal advection; this is particularly noticeable during the spring tidal period, when the near-bed salinity is about 23 on the flood compared with about 20 on the ebb. Compare the near-bed salinity (Figure 4.8) on day numbers 86.7, 87.2, 87.7 (ebb) with 86.5, 87, 87.5 (flood).

The overall density structure mainly follows the salinity structure, since this is the major component controlling the density. The temperature structure does have a slight effect, however, which is more apparent during the spring tidal period: the stratification is slightly stronger on day numbers 86.7 and 87.7 compared with 87.2 due to solar heating of the surface during the day. The strongest stratification is coincident with the strongest shear in the mean along-channel flow; this feature is seen more clearly during the neap tidal period (day numbers 78.9 and 79.4 (Figure 4.7)).

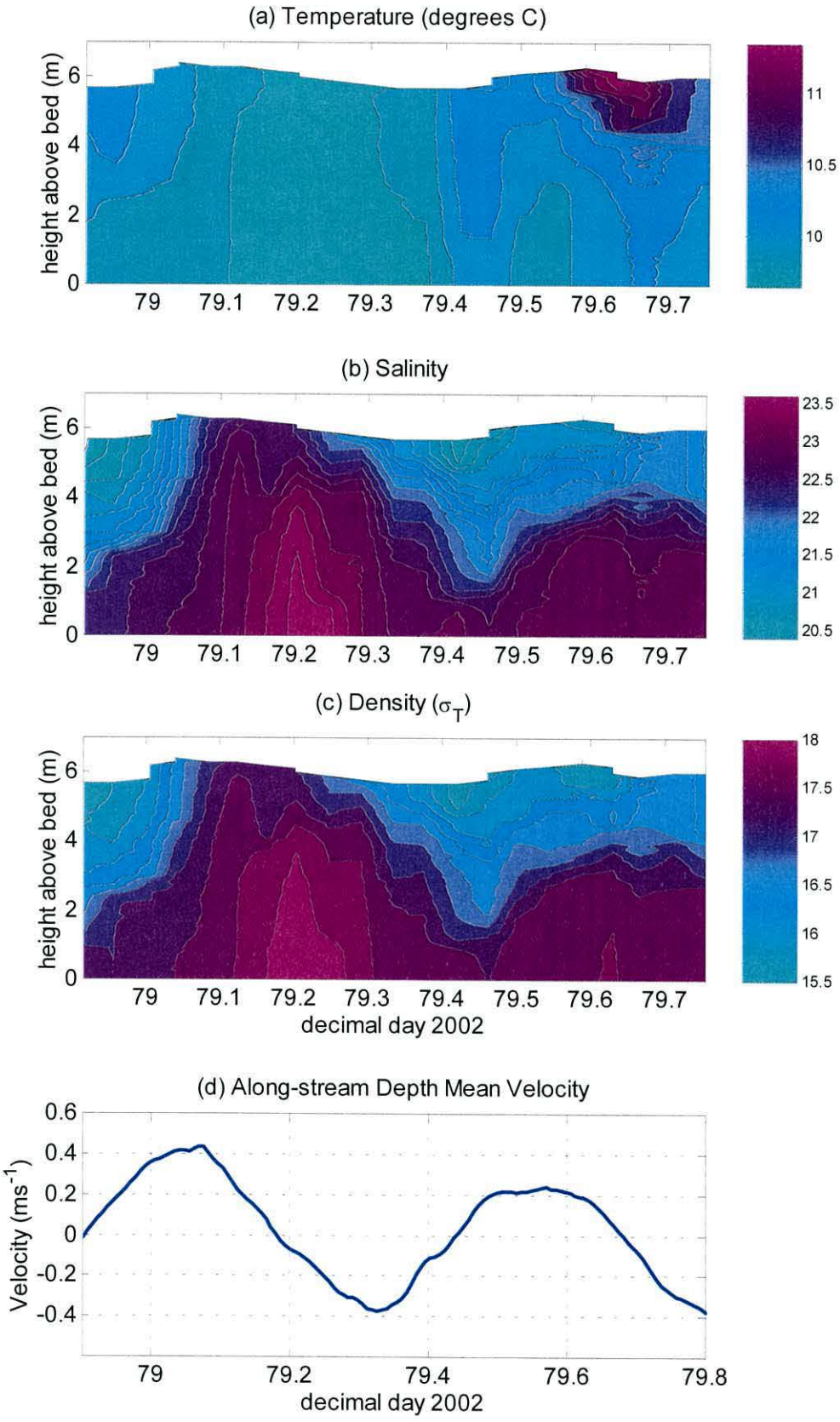

Figure 4.7: (a) Temperature, (b) Salinity, (c) Density and (d) Velocity (averaged over 30 minutes) for the first (neap) intensive period

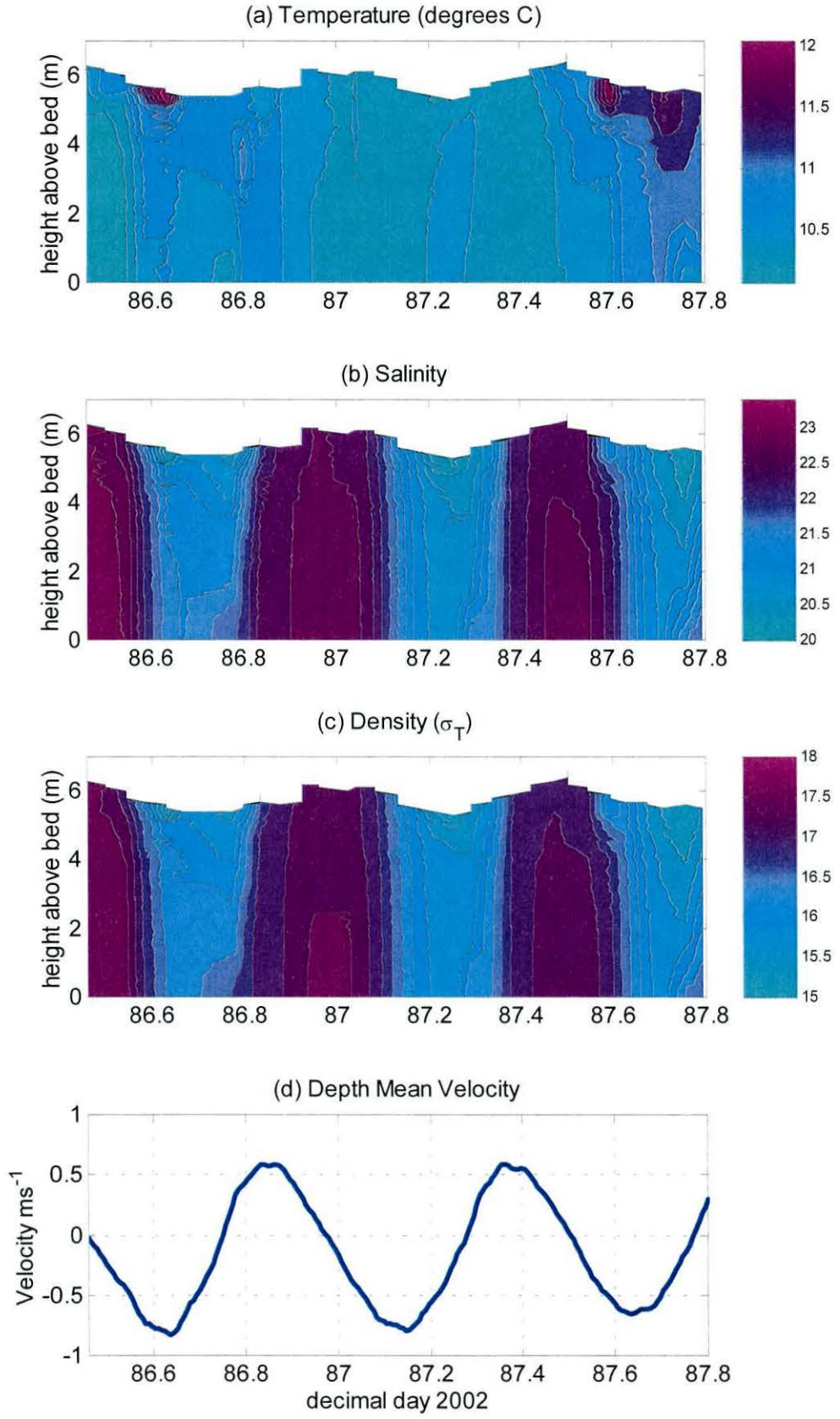

Figure 4.8: (a) Temperature, (b) Salinity, (c) Density and (d) Velocity (averaged over 30 minutes) for the second (spring) intensive period

4.3.2 Flow and turbulence at neaps

During the neap period, the along-stream near surface current speeds reach a maximum of about 0.6 m s^{-1} on the ebb and 0.5 m s^{-1} on the flood (Figure 4.9(a) and Figure 4.10(a)). The near surface peak flow is delayed by about 1.2 hours compared to the near bed peak flow on both ebb and flood.

As the flow changes direction, there is a marked difference between low and high water slack. The flow in each case changes direction first near the bed. As the flood begins, the estuarine circulation increases the flow speed near the bed and reduces it near the surface, producing strong shear; on day 78.9, a near-surface current in excess of 0.2 m s^{-1} downstream (towards Chesapeake Bay) is observed, with a near bed current of about 0.2 m s^{-1} upstream. Conversely, at the start of the ebb, the estuarine circulation opposes the flow near the bed, and increases the flow near the surface, producing a velocity profile with almost no shear.

Stratification and shear both increase during the ebb and decrease during the flood, with maximum values of both occurring in the latter part of the ebb, and minimum values in the latter part of the flood. During the second, weaker, flood, some stratification remains, with a top-bottom difference in density of at least 1.5 kg m^{-3} throughout. This produces the mid-water column maximum in the estuarine velocity profile which is a common feature of shallow estuaries (Uncles, 2002) in which the barotropic pressure gradient, which is constant with depth, interacts with the baroclinic pressure gradient due to the influx of denser water from Chesapeake Bay to increase the upstream flow speed lower in the water column.

The across-stream velocity profiles are included in panel (b) of Figure 4.9 for completeness. These velocities are generally an order of magnitude smaller than the along-stream velocities at the same height. The exception to this is on day number 79.2, at the start of the ebb, when the across-channel flow of ~0.1 m s^{-1} is of similar magnitude to the along-channel flow.

Another feature of the mean along-channel velocities during this period is the multiple peaks in the flow speed which are seen at maximum flood lower down in the water

column. At 1.3 m above the bed, there are three peaks in the mean flow speed on the first flood, at day numbers 78.93, 79 and 79.07 (Figure 4.10(a)). This is reduced to two peaks at day numbers 79 and 79.07 at 2.3m above the bed; at 4.3 m above the bed, there is a single peak at day number 79.05. These multiple peaks are observed intermittently throughout the observational period, except close to springs, and may be evidence of higher tidal harmonics.

The along-channel Reynolds stress for four heights above the bed is shown in Figure 4.10(b). During the first flood, near the bed, the Reynolds stress has a maximum coinciding with peak flow; two further peaks are observed at 1.3 m above the bed, coinciding with the two later peaks in the current velocity. At mid-water column, the peak Reynolds stress occurs much later than the peak flow, with a delay of over an hour. As the near-bed stress reaches its peak value, the water column is still well stratified (note density contours in Figure 4.9); it is not until the water column has become almost completely mixed that higher stresses are observed throughout the water column. This occurs only briefly, before the current speed falls rapidly, with an associated fall in the magnitude of the Reynolds stress.

During the ebb, only the stress in the bottom depth cell is measurable above the instrument noise level; despite the current speed being of similar magnitude to that of the earlier flood, the stresses are much lower, reaching a maximum of about 0.03 Pa near the bed, compared to around 0.12 Pa on the flood. The time of maximum Reynolds stress near the bed again coincides approximately with the peak flow. During the ebb, the water column restratifies, which prevents the Reynolds stresses from increasing near the bed and propagating through the water column (Figure 4.9(c)).

During the second flood, the currents are much weaker than during the first flood, producing lower stresses throughout the water column and leaving some residual stratification. At 1.3 m and 2.3 m above the bed, the peak Reynolds stress occurs at approximately the same time as the peak current speed at this level. Higher in the water column, the stress does not rise above the instrument noise level. The across-channel Reynolds stress, shown in Figure 4.9(d), is typically an order of magnitude smaller than that in the mean flow direction throughout the tidal cycle. An interesting

feature of the time series of Reynolds stress near the bed is that it consists of high peaks divided by relatively long periods of very low stress, in contrast to the velocity time series, which is largely sinusoidal (Figure 4.10).

The TKE production rate is shown on a logarithmic colour scale in Figure 4.11(a) for the neap tidal period. The TKE production rate only reaches its peak value on the first flood when the water column has become almost completely vertically mixed, with a near-bed maximum of 0.03 W m^{-3} ($10^{-1.5}$). On the second flood, the production is much lower, reaching only 0.004 W m^{-3} ($10^{-2.4}$), a similar magnitude to that observed on the ebb. The TKE production rate therefore largely follows the pattern of the along-channel Reynolds stress (compare with Figure 4.9(c)).

Before calculating the eddy viscosity, the data were filtered to remove any shear values which were less than two standard deviations of the expected noise in the shear estimates (0.02 s^{-1}: see chapter 3 for details) since these would tend to produce unreasonably high estimates of the eddy viscosity as well as spurious negative estimates. The eddy viscosity was then calculated using equation 2.9 (chapter 2): $N_z = -\overline{u'w'_R}/\partial\overline{u}_R/\partial z$, and is shown as a contour plot in Figure 4.11(b) and as a series of line plots for the six lowest depth cells in Figure 4.12. During the first flood, the peak eddy viscosity occurs at about 2 m above the bed. It occurs later than either the peak Reynolds stress or TKE production rate: as the shear diminishes, but whilst the Reynolds stress is still relatively high. There is also a smaller peak in the eddy viscosity in the lowest two depth cells, which precedes the main peak during the first flood, similar to the smaller peak in the Reynolds stress at day number 79. During the ebb and the second flood, the eddy viscosity is only measurable close to the bed; this is associated with the very low values of Reynolds stress and TKE production rate at this time.

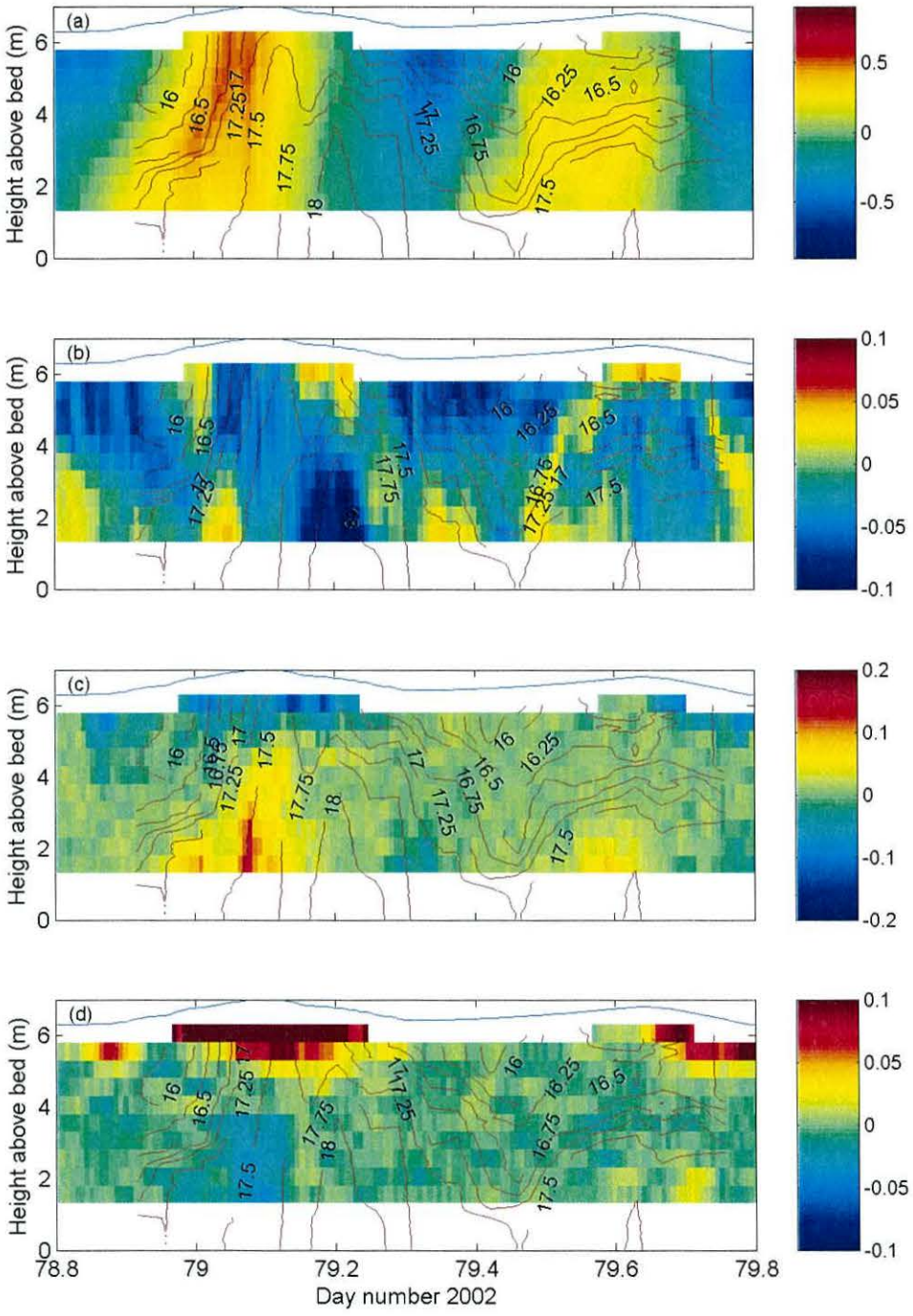

Figure 4.9: (a) Along-channel velocity (m s^{-1}), (b) across channel velocity (m s^{-1}), (c) along-channel Reynolds stress (Pa) and (d) across-channel Reynolds stress (Pa) with density contours (σ_T) for the first (neap) intensive period. Note that the colour scales are different for the along- and across-channel components in order to show the features of each.

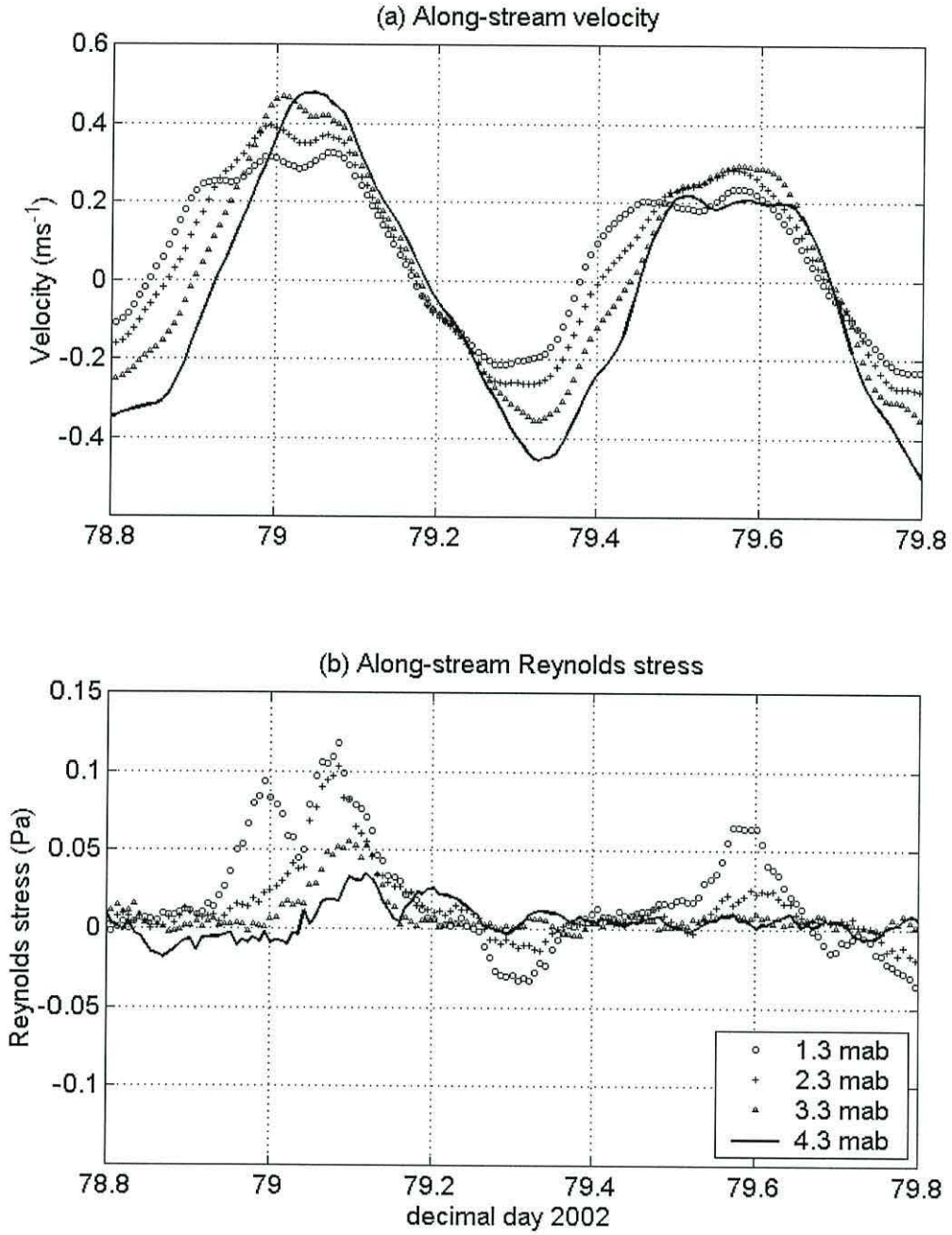

Figure 4.10: Along-channel velocity and Reynolds stress for first (neap) intensive period for four depth cells centred at 1.3 m, 2.3 m 3.3 m and 4.3 m above the bed. A 60-minute running mean has been applied to the 10-minute averaged values.

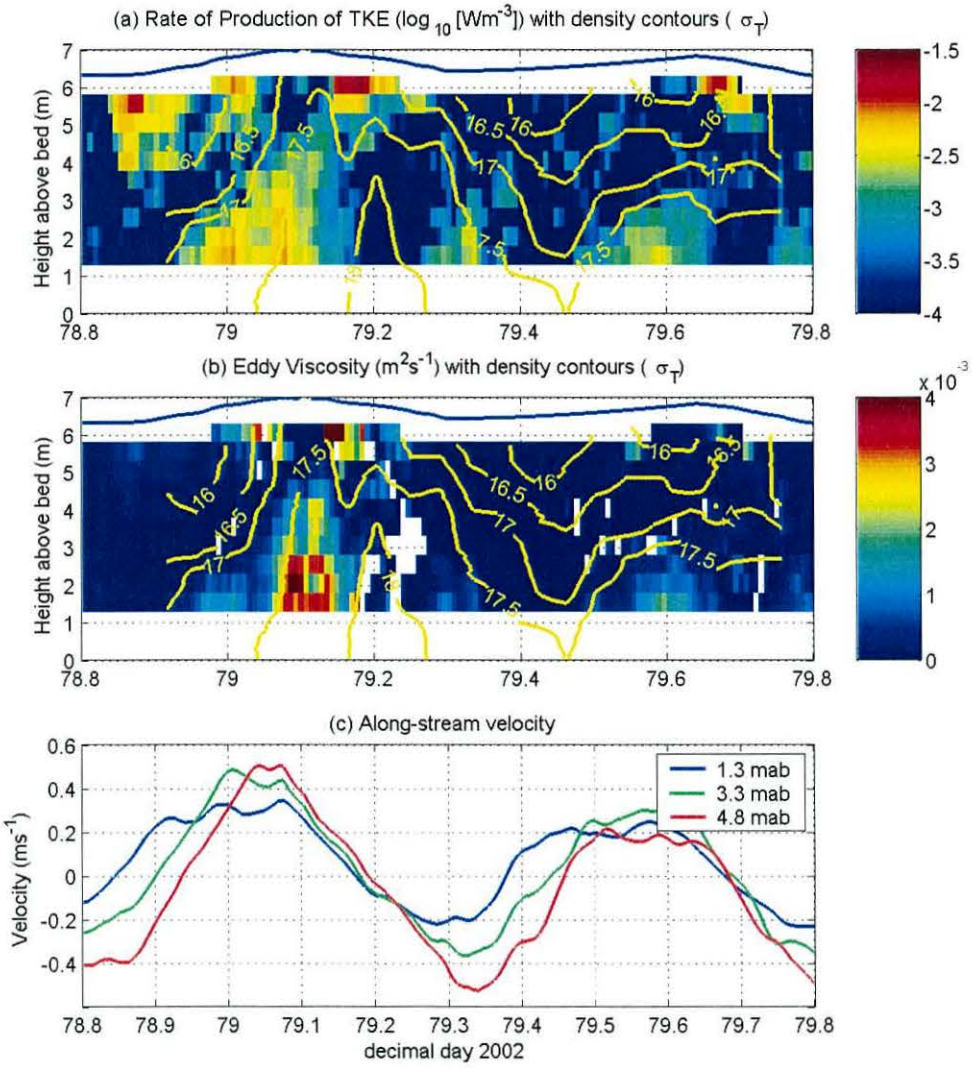

Figure 4.11: Rate of Production of TKE (P) and Eddy Viscosity (N_z) for the first (neap) intensive period, along with the mean along-channel flow at three heights above the bed. The velocities are 30-minute mean values; P and N_z have been calculated every 10 minutes and the 30-minute mean value plotted every 10 minutes. The blank spaces in the plots of P and N_z are where these parameters are undefined, that is, where the Reynolds stress and the shear have opposite signs. This is due to both estimates being subject to a certain degree of uncertainty, so this occurs mainly at times of low stress and/or low shear. The eddy viscosity is also undefined at those times when the shear in the mean flow approaches zero.

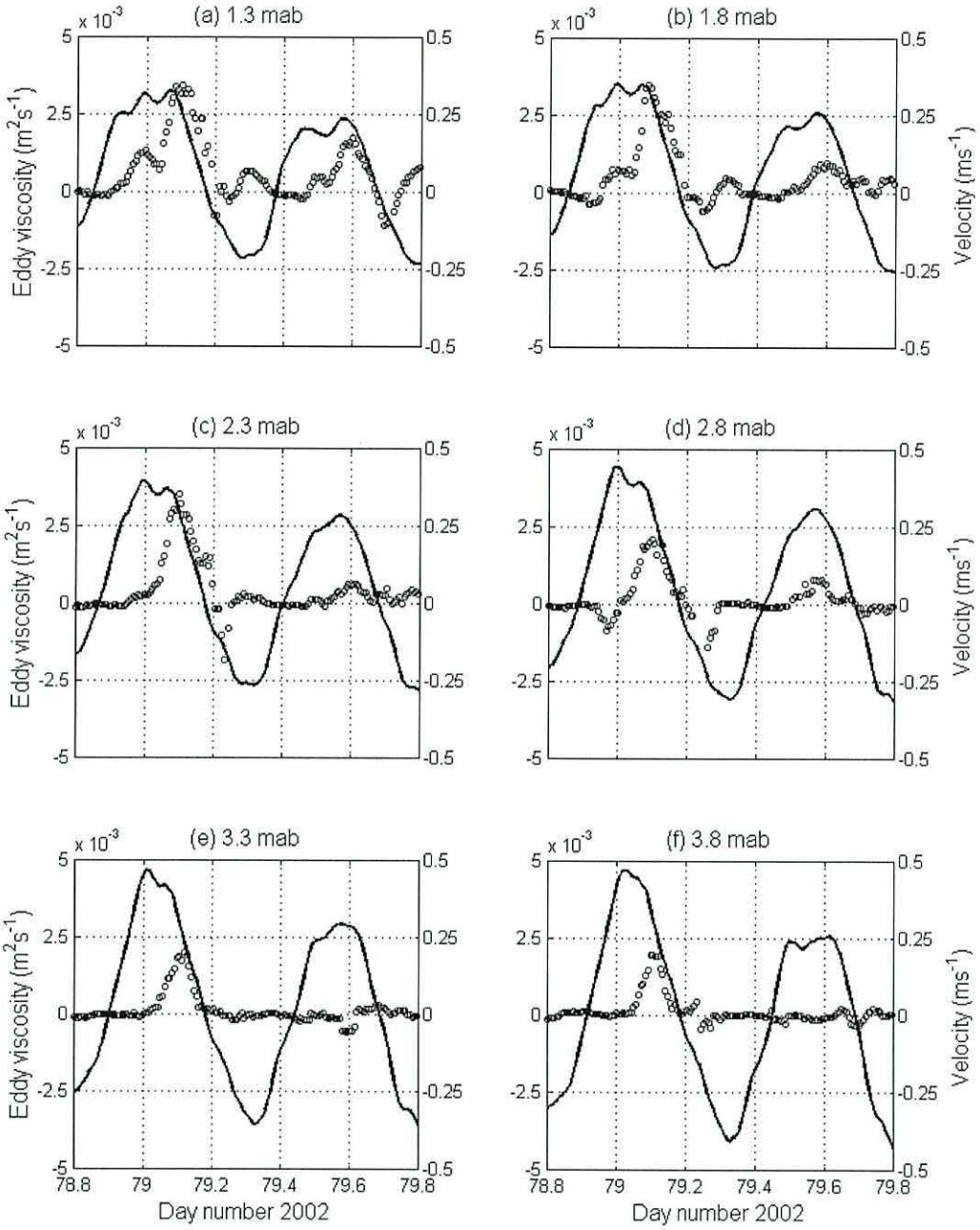

Figure 4.12: Velocity (solid line) and eddy viscosity (open circles) at 6 heights above the bed for the neap tidal period. The y-axis scale is in m s^{-1} for the velocities and m^2 s^{-1} for the eddy viscosities

4.3.3 Flow and turbulence at springs

At springs, there is a strong flood-ebb asymmetry in mean flow and turbulent parameters, but each tidal cycle tends to follow the same pattern. The near surface flow speed at springs reaches a maximum of about 1 m s^{-1} on the ebb and 0.7 m s^{-1} on the flood. The stratification is generally weak, with slight stratification developing towards the end of the ebb, and being eroded almost completely during the flood. The effect of the estuarine circulation, which tends to produce a mid-depth maximum in the velocity profile during the flood, is therefore much less pronounced than at neaps.

The water column experiences some degree of shear, which is stronger on the ebb than on the flood (Figure 4.13(a)). Near-bed and near-surface regions reach zero velocity at about the same time on the transition from flood to ebb (day numbers 86.46, 86.97 and 87.5); on the transition from ebb to flood the zero flow near the bed precedes that near the surface by about 0.5 hours (day numbers 86.75, 87.27 and 87.77). However, there is no discernible delay in the peak flow between near bed and near surface regions.

The across-channel current, shown Figure 4.13(b), is about an order of magnitude smaller than that in the along-channel direction; the two components are of a similar magnitude only when the current changes direction. This can be seen on days 86.8 and 87.3 at the start of the flood, and days 87 and 87.55 at the start of the ebb.

On the flood, the Reynolds stress reaches its maximum value soon after the peak flow, with a delay of about an hour (Figure 4.13(c) and Figure 4.14). This delay is approximately constant throughout the water column. The stress reduces in magnitude further away from the bed, decreasing from a maximum of almost 0.6 Pa near the bed, to less than 0.4 Pa at 4.3 m above the bed (Figure 4.14, day number 86.87). On the ebb, the Reynolds stress reaches its maximum value throughout the water column at approximately the same time, which coincides approximately with the peak flow throughout the water column.

The Reynolds stress time series shown in Figure 4.14 indicates long periods of very low stress as the current changes direction, with very strong peaks during periods of

strong flow. This is similar to the pattern seen during the neap period near the bed. The period of very low stress is slightly longer on the transition from flood to ebb than on the transition from ebb to flood, and increases higher up the water column. Near the bed, the period of very low Reynolds stress starts at about the time of zero flow; higher in the water column, the low stresses are centred around the time of zero flow.

In common with the neaps period, the across-channel Reynolds stress shown in Figure 4.13 (d) is generally very low with the highest values occurring at mid-water column at peak flood.

The Reynolds stress calculated from the ADV data for the period of the 1.2 MHz ADCP deployment at springs (Figure 4.15) largely tracks the estimates from the ADCP data; the stress appears to follow a different relationship with the velocity at faster flow speeds (above ~ 0.2 m s^{-1}) compared with that which occurs at lower flow speeds. Although the phenomenon is less pronounced in the ADV data, it is nevertheless present, and is particularly noticeable on the transition from flood to ebb (day numbers 84.9, 85.5, 86, 86.5, 87). It is also present on some tidal cycles on the transition from ebb to flood (day numbers 84.6, 86.2). The presence of this feature in the ADV data, as well as in the surface elevation estimated from the ADCP backscatter, indicates that it is a true characteristic of the flow rather than an error or an artefact of the ADCP processing method.

The TKE production rate at springs is shown in Figure 4.16 on a logarithmic scale (a) and on a linear scale (b). On the ebb, the TKE production rate reaches a maximum of 0.1 W m^{-3} near the bed. This compares with a maximum of 0.04 W m^{-3} on the flood. High levels of TKE production are present throughout the water column during the ebb, with values reaching up to 0.05 W m^{-3} at 4.8 m above the bed. On the flood, the values at this level are an order of magnitude smaller.

The eddy viscosity is shown as a contour plot in Figure 4.16(c) and as a line plot for eight different levels above the bed in Figure 4.17. The striking feature of the eddy viscosity for this part of the spring-neap cycle is that it is much higher on the flood phase of the tidal cycle than on the ebb, despite the TKE production rate being much

higher on the ebb. At 1.3 m above the bed, the eddy viscosity is of similar magnitude on the flood and the ebb. This is particularly evident in Figure 4.17(a). Higher in the water column, the eddy viscosity increases on the flood and decreases on the ebb, with the maximum flood value occurring at 3 m to 4 m above the bed (Figure 4.17(e) and (f)).

The high eddy viscosity at times of lower TKE production can be explained by looking at the parameters from which they were calculated. At mid-depth, the Reynolds stress is of similar magnitude for both ebb and flood, (Figure 4.14(d)) while the shear is much lower on the flood (compare the flood and ebb parts of Figure 4.16(d)). The high TKE production rate on the ebb can be explained by the higher current speeds and shear (Figure 4.16(d)). On the flood, the eddy viscosity is higher, since the low shear allows the water to move more freely in a vertical plane.

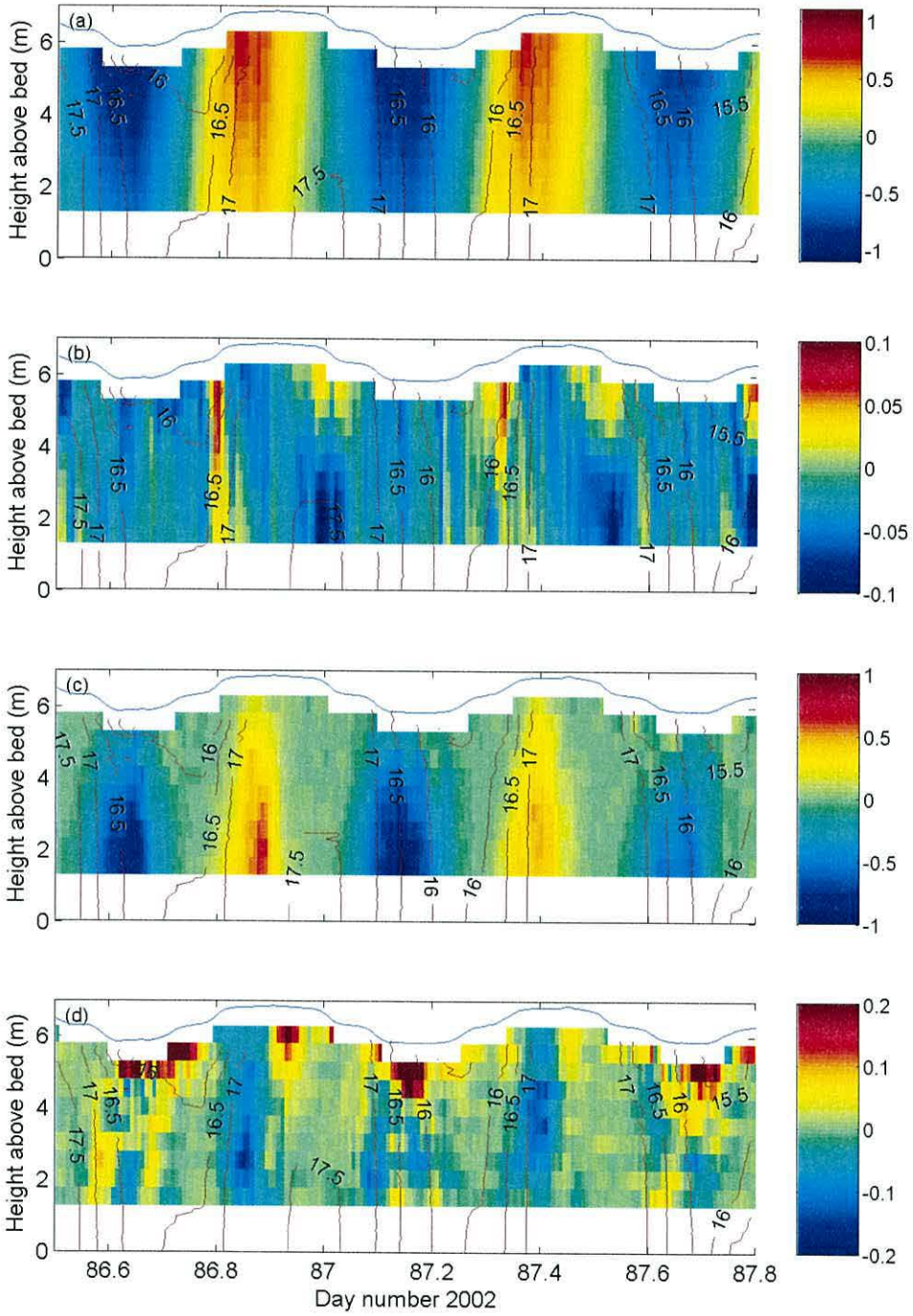

Figure 4.13: (a) Along-channel velocity (m s^{-1}), (b) across channel velocity (m s^{-1}), (c) along-channel Reynolds stress (Pa) and (d) across-channel Reynolds stress (Pa) with density contours (σ_T) for the second (spring) intensive period. Note that the colour scales are different for the along- and across-channel components in order to show the features of each.

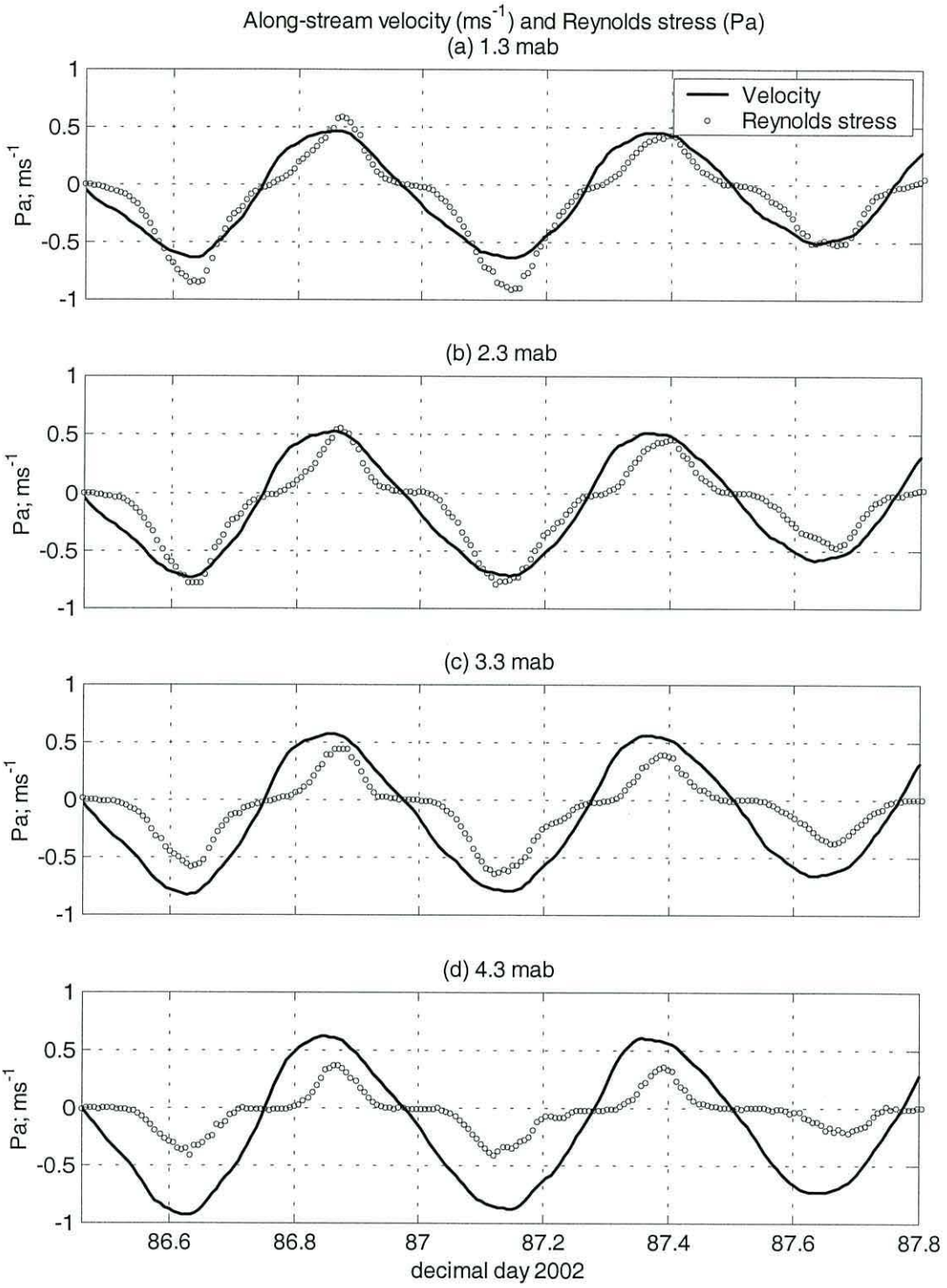

Figure 4.14: Along-stream velocity and Reynolds stress ($-\rho\overline{u'w'}$) at four heights above the bed for the second (spring) intensive period. A running mean of 60-minutes has been used to smooth the original 10-minute averaged data

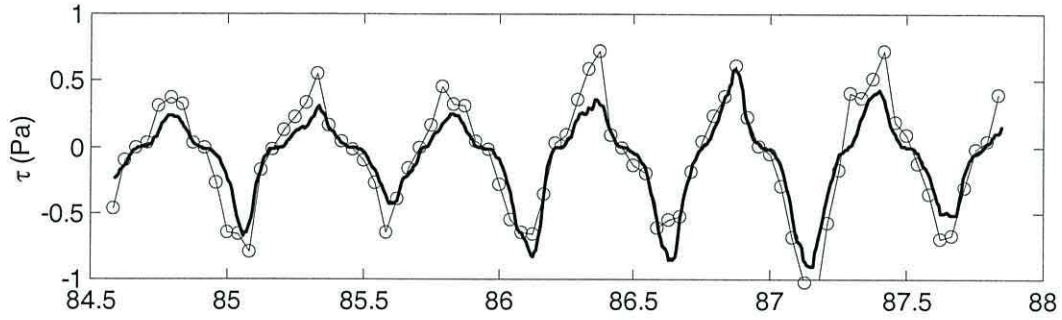

Figure 4.15: Comparison of Reynolds stress calculated from the ADCP at 1.3 m above the bed (solid line) and the ADV at 1.12 m above the bed (open circles)

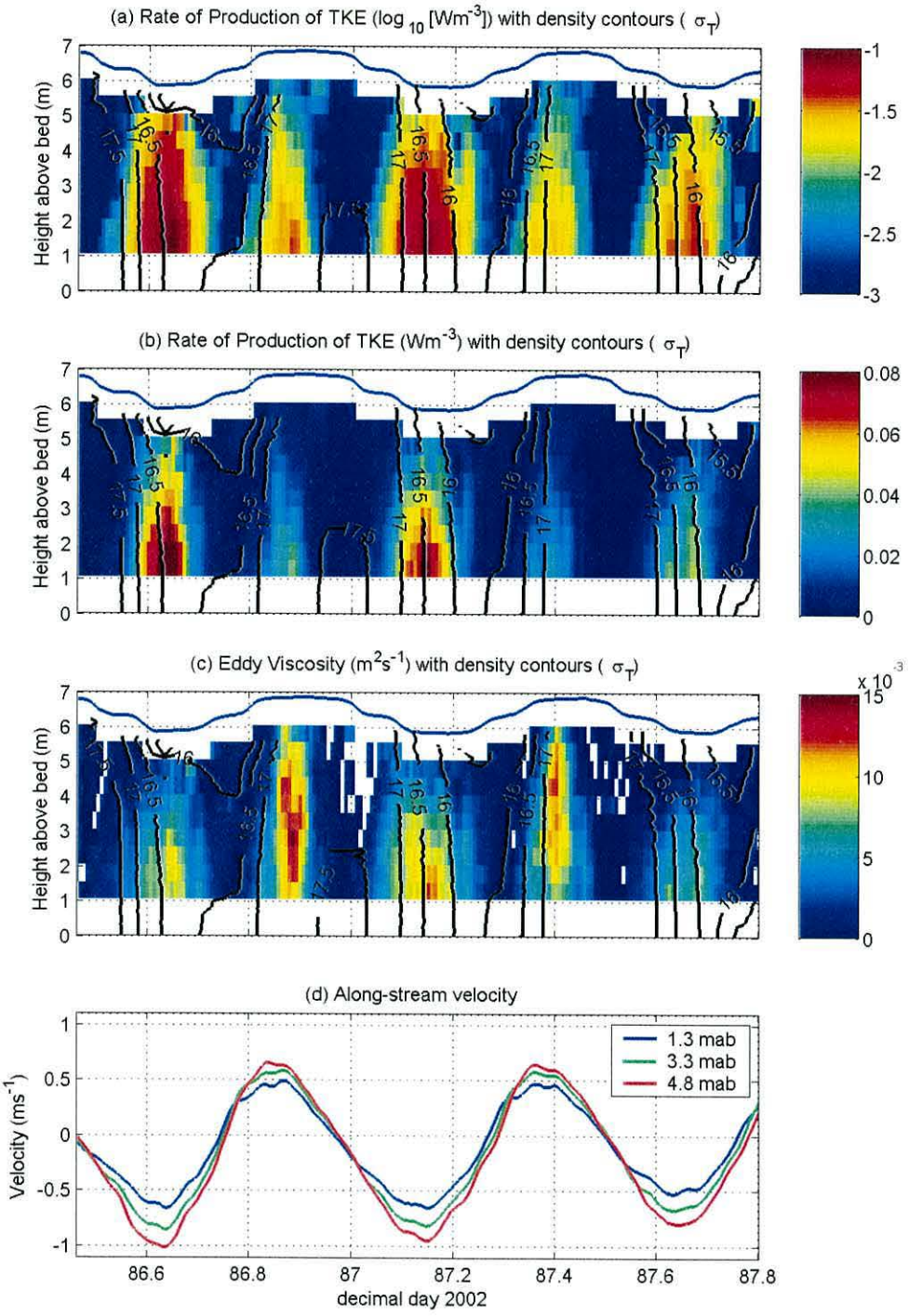

Figure 4.16: Rate of Production of TKE and Eddy Viscosity for second (spring) intensive period

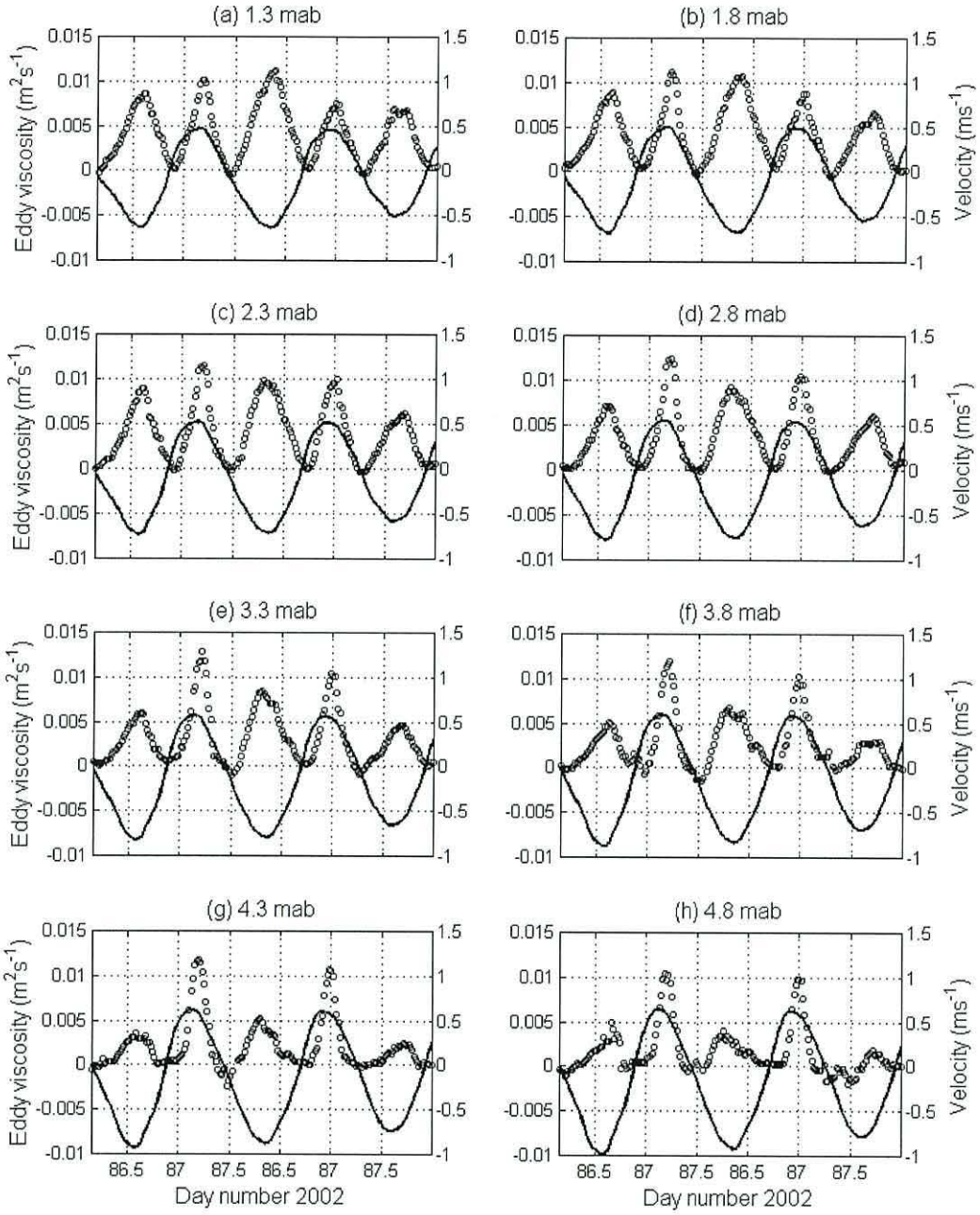

Figure 4.17: Velocity (solid line) and eddy viscosity (open circles) at 8 heights above the bed for the spring tidal period.

4.4 TKE

It was shown in chapter 3 that a parameter Q which is proportional to the TKE $q^2/2 = \left(\overline{u'^2} + \overline{v'^2} + \overline{w'^2}\right)/2$ (chapter 2, equation 2.1) can be calculated from the sum of the along-beam velocity variances: $Q = \frac{1}{4\sin^2\theta}\sum_{i=1}^{4}\overline{b_i'^2}$ (chapter 3, equation 3.12). An overview of the time series of Q over the entire period of the observations was shown in Figure 4.5. In order to analyse the data more effectively over shorter time periods, Q is plotted for the entire period of the first and second deployments of the 1.2 MHz ADCP in Figure 4.18(a) and Figure 4.19(a) respectively.

The cycle of TKE at neaps (Figure 4.18(a)) is not clearly linked with the tidal cycle (compare with the depth mean velocity in panel (b)), but there is a series of high values near the surface. The highest of these occurs at the time of the strong wind event on day 80, indicating that the high along-beam variances are due to the orbital velocities of wave motions. In order to investigate the correlation between the wind strength and direction and the TKE, the along-channel component of the wind is plotted in panel (c), with positive values indicating that the wind is blowing up-river.

The correlation between the wind velocity vector and the high along-beam standard deviations (panel (d)) is very clear. On day 80.2, the very strong wind event, in which there is a 10 m s^{-1} wind blowing down-river during the flood, produces standard deviations of over 0.15 m s^{-1} near the surface, compared with the tidally-induced turbulence, which produces standard deviations of order 10^{-3} m s^{-1}. Three other periods of strong winds (day numbers 81.5, 82 and 83) are also connected with an increase in the along-beam standard deviations and Q. On each of these occasions, the wind is blowing in an up-river direction during the ebb. When the wind is in the same direction as the flow, such as on day 78.8 at the start of the record, Q remains low. The effect of the wind can also be seen in the record of the Reynolds stress (panel (e)), with high stresses appearing near the surface at times when the Q values are elevated: particularly on day 80, but also on day 79.1 around high water, day 81.6 at high water and day 83 at low water).

During the second ADCP deployment covering the spring tidal period (Figure 4.19), initial low winds are replaced by fairly strong winds of around 8 m s^{-1} blowing up-river during the flood, which produces slightly elevated values of Q near the surface (day 84.8). As the tidal flow changes direction, so does the wind, and again the near surface Q is raised by only a small amount (day 85). During the next flood (day 85.3), the wind blows downstream, this time substantially elevating the near-surface values of Q over a longer period. A brief up-river wind event at slack water on day 85.5 is followed by nearly 24 hours of down-river winds. During this period it can clearly be seen how the near-surface value of Q increases when the wind is directed against the tidal flow, as the down-river wind increases Q near the surface much more on the flood than on the ebb. From day 86.5 until the end of the record, the wind blows upstream; this time the largest values of near-surface Q occur during the ebb. The wind seems to have less effect on the Reynolds stress during the springs period; its effect can only really be seen near the surface on day 85.4 around high water.

These data indicate that high along-beam variances near the surface are due to the effect of waves, with the largest waves being connected with periods when there are strong winds blowing against the mean flow. For the period of these observations, no data of wave height or frequency are available, so for the purpose of the analysis of the present data set, the effect of waves can only be treated as an uncertainty in the estimates of the turbulent parameters. In general, the Reynolds stress and TKE production rate estimates are not contaminated by the effects of wave action to the same extent as Q, since the wave action is present in all four beams, and is effectively cancelled out. However, the waves are sufficiently strong, the effects are also seen in the estimates of Reynolds stress.

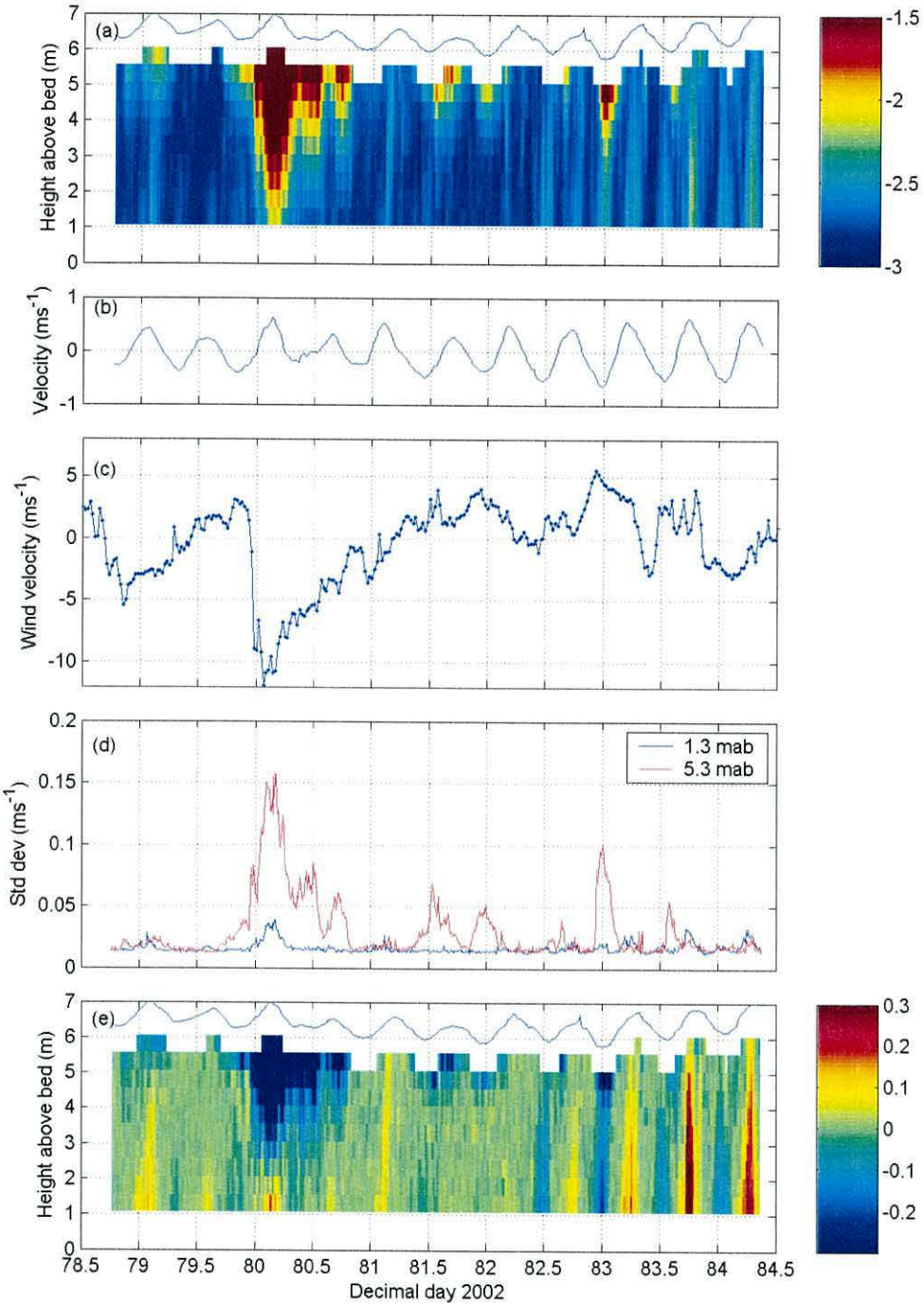

Figure 4.18: (a) Q (quantity proportional to the TKE per unit mass) for the first deployment of the 1.2MHz ADCP at neaps plotted on a logarithmic colour scale ($\log_{10}$[J kg^{-1}]); (b) Along-stream depth mean velocity (30-minute means); (c) Wind velocity (30-minute means), oriented in the along-channel direction: positive values indicate the wind component directed up-river; (d) Standard deviation of the along beam velocities for beam 1 at 1.3 and 5.3 m above the bed; (e) Along-channel Reynolds stress (Pa) using 30-minute mean values.

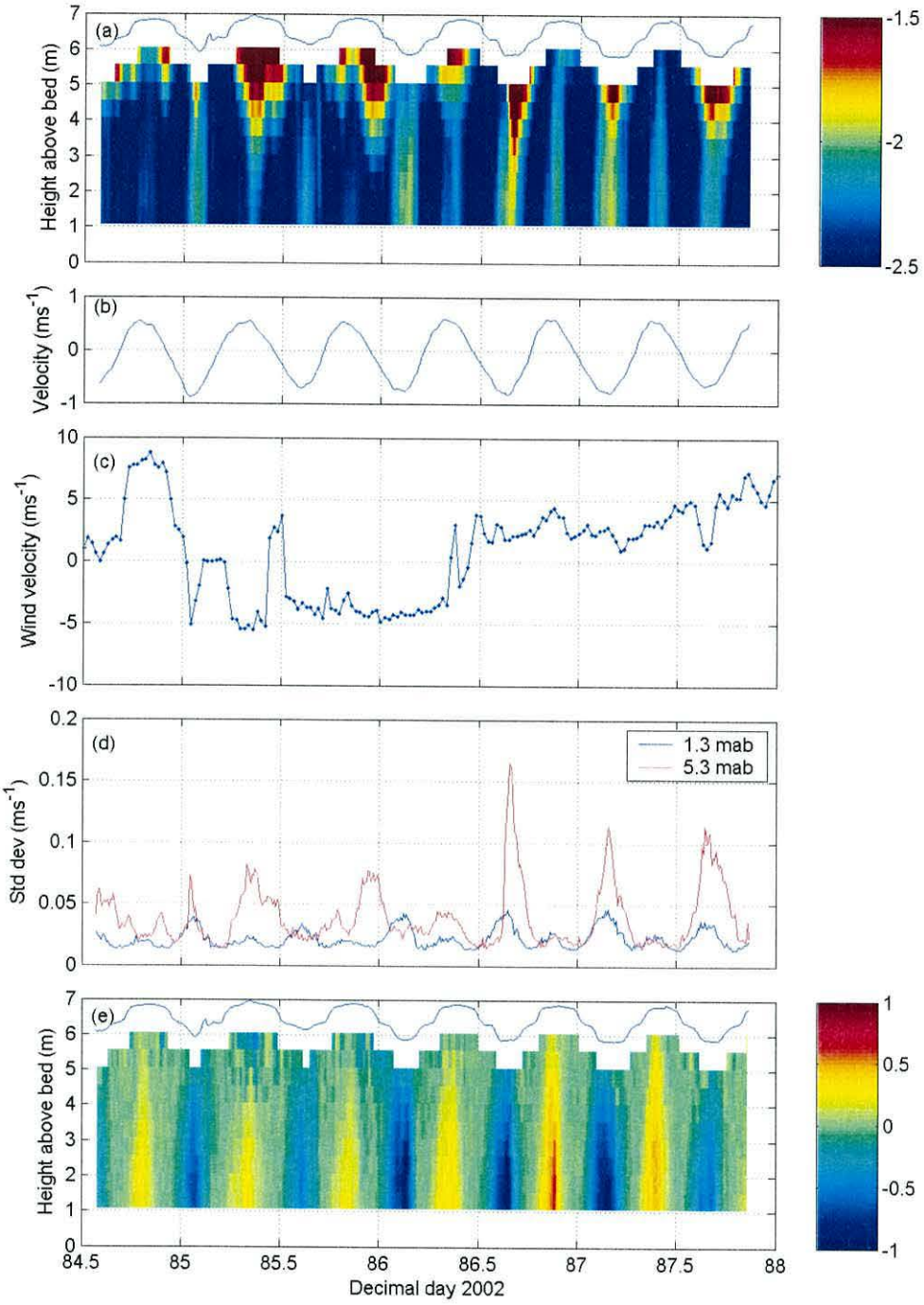

Figure 4.19: (a) Q (quantity proportional to the TKE per unit mass) for the second deployment of the 1.2MHz ADCP at springs plotted on a logarithmic colour scale ($\log_{10}$[J kg^{-1}]); (b) Along-stream depth mean velocity (30-minute means); (c) Wind velocity (30-minute means), oriented in the along-channel direction: positive values indicate the wind component directed up-river; (d) Standard deviation of the along beam velocities for beam 1 at 1.3 and 5.3 m above the bed; (e) Along-channel Reynolds stress (Pa) using 30-minute mean values.

4.5 Summary

The Reynolds stress, TKE production rate and eddy viscosity are all affected by the degree of stratification in the water column, taking lower values when the water column is stratified. This is seen most clearly at neaps: during the ebb, when the stratification is at its maximum level, all three parameters have lower values than during the flood, despite the higher currents on the ebb. At springs, when the stratification is weak, the highest Reynolds stresses and TKE production rates occur on the ebb, when the currents are strongest. In contrast to this, the eddy viscosity is higher on the flood, due to the effects of tidal straining; the tendency to stratify on the ebb results in lower values of the eddy viscosities, even though the local stratification is low compared to that seen at neaps.

A parameter Q, which is proportional to the TKE, can be used to ascertain when wave effects are likely to produce significant errors in the Reynolds stress and TKE production rate estimates. In the absence of measurements of the anisotropy of the flow, this is also the best available estimate of the cycle of TKE.

CHAPTER 5

The York River Estuary: Interpretation of Results

5.1 Tidal straining

In order to interpret the effects of the horizontal density gradient on the York River results, an analysis of tidal straining is necessary, the theory of which was described in section 2.4.4. A comparison of the input of buoyancy due to tidal straining and its destruction by the effects of turbulent mixing can be made, and from this comparison it should be possible to predict when the water column will stratify due to tidal straining, and when the stirring mechanism will out-compete the straining term, resulting in complete vertical mixing of the water column.

The rate of change of φ due to straining $(\partial\varphi/\partial t)_{strain}$ is estimated from the horizontal density gradient from the S4 moorings and the shear in the mean flow from the ADCP. There was a failure of one of the S4 moorings mounted near the bed, so the along-channel density gradient $\partial\rho/\partial x$ is estimated from the two near-surface moorings. The surface experiences slightly greater differences in density over a tidal cycle than the bed, due to the effects of surface heating during the day and the high shear in the mean flow during the ebb. As a result, the use of the two surface moorings may not accurately represent the straining parameter, but the deviation from the true value should not be great.

A large proportion of the TKE production takes place close to the bed in the region which was not sampled by the ADCP (below 1.05mab), so a correction was applied to the depth-integrated production estimates to obtain a realistic value of the total TKE production rate for the tidal stirring term, $(\partial\varphi/\partial t)_{stir} = \delta P_{total}/h$ where δ is an efficiency term. If it is assumed that the velocity profile is logarithmic, then:

$$\frac{\int_{z_0}^{h} P dz}{\int_{1.05}^{h} P dz} \propto \frac{\log(h/z_0)}{\log(h/1.05)} \tag{5.1}$$

Using a value of $z_0 = 0.001$m, with a mean depth h over the tidal cycle of 6.4m, this gives a correction factor of approximately 5. The wind stirring term is given by $(\partial\varphi/\partial t)_{wind} = \delta_s k_s \rho_s W^3/h$, where δ_s is an efficiency term and k_s is a surface drag

coefficient. Values for δ, δ_s and k_s are taken from the results of Simpson and Bowers (1981): $\delta = 0.004$, $\delta_s = 0.023$, $k_s = 6.4 \times 10^{-5}$ and $\rho_s = 1$ kg m^{-3}.

The times at which it is expected that straining will out-compete stirring and result in stratification of the water column can be obtained by subtracting the tidal and wind stirring terms from the straining term [equation (2.15)]. Two estimates for the potential energy anomaly φ can then be obtained: one from the net value of $\partial\varphi/\partial t$ integrated over time, the other directly from the CTD measurements.

The time series the along-channel velocity at two heights for the spring intensive period is shown in panel (a) of Figure 5.1, the tidal straining parameter is shown in panel (b) and the tidal and wind stirring terms are shown in panel (c). At almost all times, the tidal stirring term is greater than the wind stirring term. The exceptions to this are at the end of the ebb, on day numbers 86.75 and 87.75, when relatively strong winds coincide with weak flow.

Panel (d) shows the net value of $\partial\varphi/\partial t$ when the tidal stirring term is subtracted from the straining term, neglecting wind effects. Positive values indicate that the straining mechanism is strong enough to stratify the water column. Two estimates are used for the efficiency δ: 0.004 and 0.001. The smaller efficiency is plotted, since the one empirically determined by Simpson and Bowers (1981) for thermally stratified regions of shelf seas indicates that the water column should remain vertically mixed for most of the tidal cycle, but this is not the case in the York River. For both efficiencies, the straining is seen to reach its peak on the late ebb (day numbers 86.75, 87.3 and 87.8), and also to dominate at the beginning of the ebb (day numbers 86.55, 87-87.05 and 87.6), with the stirring reaching its maximum around peak flood (day numbers 86.85 and 87.35).

In panel (e) the potential energy anomaly estimated by integrating the net value of $\partial\varphi/\partial t$ over time is plotted, using both efficiencies, as in panel (d); a third symbol represents the lower efficiency of tidal stirring combined with wind stirring. All three time series follow the same pattern, with stratification occurring at the end of the ebb (day numbers 86.75, 87.3 and 87.8), and to a lesser extent at the start of the ebb on the

first and third tidal cycles (day numbers 86.55 and 87.6). The lower efficiency of tidal stirring also indicates some stratification at the start of the ebb on the second tidal cycle (day number 87.1).

The potential energy anomaly φ estimated directly from the CTD data is shown in panel (f) and indicates that the times of greatest stratification from the direct measurements coincide with those predicted by the tidal straining analysis. Only the data from the lowest 6m of the water column are used in this estimate, to avoid errors due to the action of surface waves at low water, which might affect the pressure measurements made by the CTD. The CTD values are most closely tracked for an efficiency δ of 0.001, although the inclusion of wind effects reduces the stratification to zero on day number 87.8, despite the CTD data at this point indicating a weakly stratified water column.

The main difference between the estimate of φ from the straining and stirring terms and that from the CTD data is that the latter show the water column to be stratified to some degree throughout the period of observations, except briefly at peak flood (day numbers 86.9 and 87.4), while the tidal straining estimates predict a vertically mixed water column for the whole period from peak flood up until after the start of the ebb. The CTD values of φ are also about twice those estimated from straining and stirring. The discrepancy between the tidal straining estimates of the degree of stratification and those observed in the CTD data could be due to one or more of the following factors: (a) The efficiency term δ is an empirically determined factor resulting from research in regions of thermal stratification, so an appropriate value for a partially stratified estuary such as the York River may differ considerably from the two values used in the calculations here; (b) The efficiency and drag coefficient terms in the wind stirring calculations were also taken from the study in shelf seas and may need to be amended for the conditions in the estuary; (c) Errors in the estimate of the change in φ due to tidal straining may have resulted from the use of the horizontal density gradient at the surface rather than a mean value for the whole water column; (d) The horizontal density gradient may not be uniform over the distance between the two moorings; (e) The degree of stratification may be dependent on local effects such as local freshwater runoff as well as on the large scale effects of the horizontal density gradient; (f) The wind measurements were made at Gloucester Point, some 15km

from the observation site, so may not accurately represent the local meteorological conditions throughout the observation period.

One of the interesting features of the York River results at springs is that high TKE production rates (P) are coincident with low eddy viscosity (N_z) on the ebb, and low values of P coincide with high N_z on the flood. An examination of the terms which govern N_z and P will improve understanding of this phenomenon.

The appropriate parameters [(a) velocity, (b) buoyancy frequency squared (N^2), (c) Reynolds stress (τ), (d) N_z, (e) P and (f) Richardson number (Ri)] are shown in Figure 5.2 for four parts of the tidal cycle: peak flood, peak ebb, the transition from ebb to flood and the transition from flood to ebb [compare the velocity profiles in panel (a)] . The high values of P observed on the ebb during the spring tidal period [panel (e)] is sufficient to keep the water column locally vertically mixed [note the low values of N^2 in panel (b)], but the turbulence is constantly working against the input of stratification due to tidal straining, so N_z is continuously being suppressed by the tendency of the water column to stratify [panel (d)]. During the flood, the low shear which results from tidal straining means that the water can move more freely in a vertical plane, hence N_z is higher on the flood. However, the momentum transport between layers is low, since the water is all moving at about the same speed, and this keeps P low [panel (e)]. The apparent contradiction in which high values of P are coincident with low N_z on the ebb and low P coincides with high N_z on the flood therefore has a simple physical explanation.

Ri represents the static stability of a stratified shear flow: low values of Ri indicate that the water column is unstable and turbulent mixing occurs; high values indicate a water column in which the stratification is sufficient to suppress the turbulent mixing processes. It might therefore be expected that during periods in which the eddy viscosity is high, the value of Ri would be low. A comparison of panels (d) and (f) indicates that this relationship is somewhat more complex. During the peak flow period in the flood direction, Ri remains at or above the critical value (0.25) in the top part of the water column, at about 4mab and higher, but N_z remains high throughout the water column [panel (d)], implying that mixing is taking place despite the fact that

Ri is above the critical value. Conversely, during the peak flow period in the ebb direction, *Ri* remains below the critical value in the top half of the water column, but N_z falls linearly between bed and surface.

The reason for the difference in *Ri* between ebb and flood can be seen by comparing panels (a) and (b). *N* is of similar magnitude at ~3-5m above the bed at peak flow on both ebb and flood [panel (b)], indicating a similar degree of stratification, but the shear is much higher on the ebb [panel (a)], hence *Ri* is lower on the ebb than on the flood [panel (f)]. This brief analysis indicates the complexity of the interplay between turbulence, stratification, shear and the horizontal density gradient, so the relationship between N_z and *Ri* will now be examined in more detail.

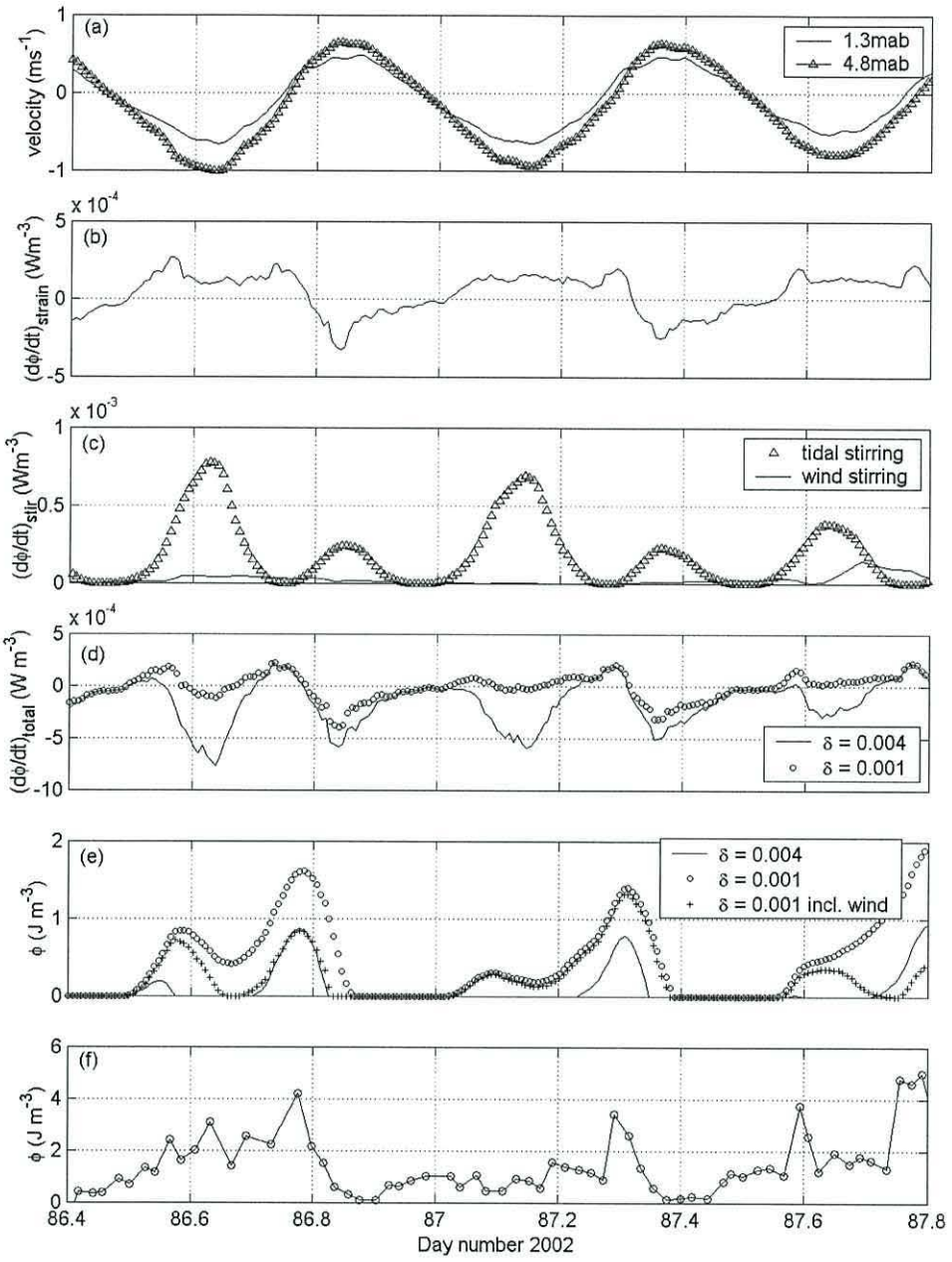

Figure 5.1: Tidal straining parameters for second (spring) intensive period: (a) the near-bed and near-surface along-channel velocity indicating the shear in the mean flow; (b) the tidal straining parameter $\partial\varphi/\partial t$ obtained using equation 2.15; (c) the estimate of $\partial\varphi/\partial t$ due to wind and tidal stirring; (d) $(\partial\varphi/\partial t)_{strain} - (\partial\varphi/\partial t)_{stir}$ including stirring due to the tides only and two different values for the efficiency factor δ; (e) an estimate of the potential energy anomaly φ by integrating (d) over time for the values of δ and (f) a direct estimate of φ from the CTD density profiles.

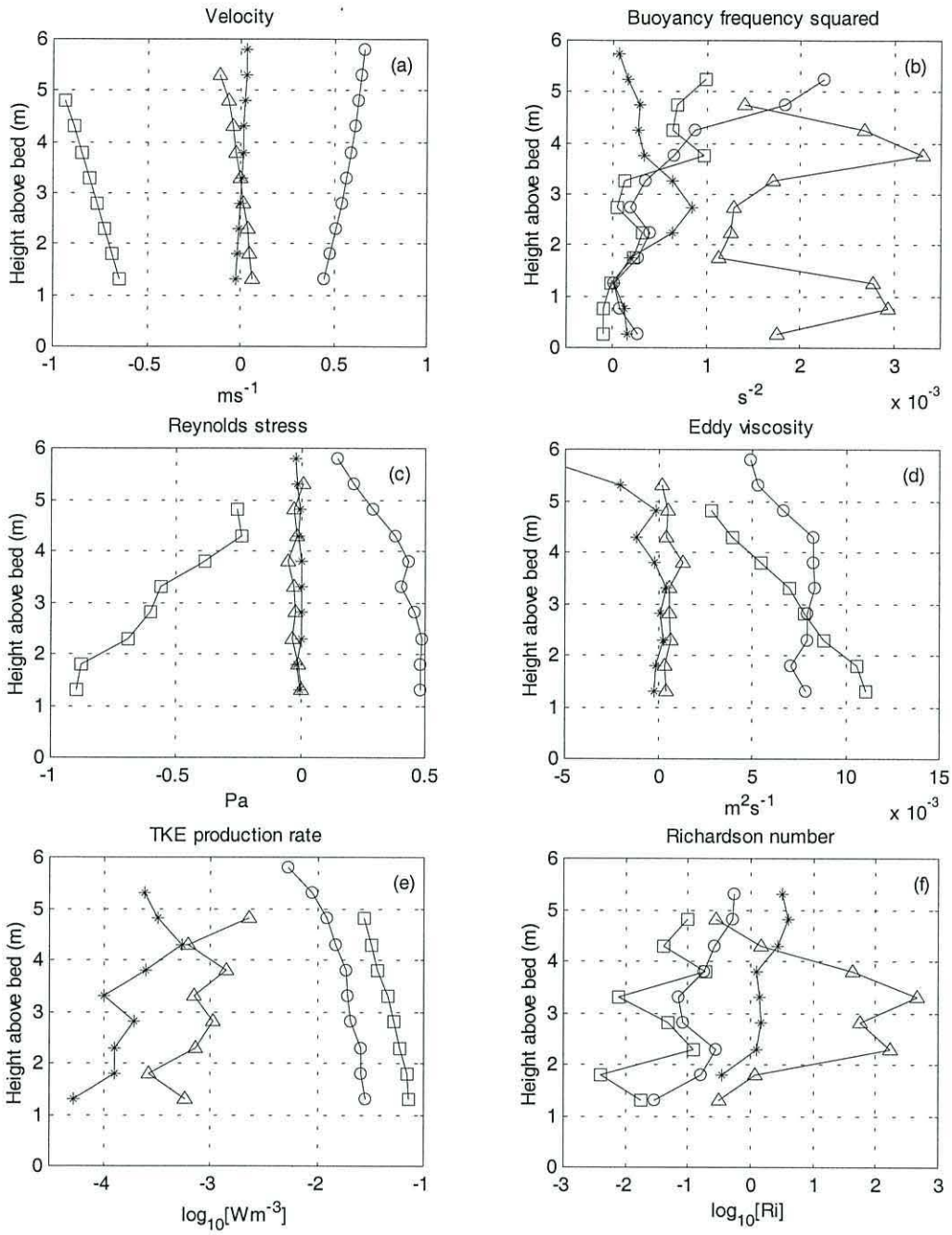

Figure 5.2: Profiles of parameters for four selected times in the tidal cycle: peak flood (circles), peak ebb (squares), transition from ebb to flood (triangles) and transition from flood to ebb (asterisks). 30-minute averaging was used for the velocity and Reynolds stress, 60-minute averaging for the eddy viscosity and TKE production rate. The buoyancy frequency and Richardson number were calculated at the times of the CTD profiles with a 60-minute average used for the shear, which was interpolated to the appropriate time. The tidal cycle chosen was from day numbers 86.75 to 87.2, since this was the cycle with the highest flow speeds and the pattern of each parameter was at its clearest.

5.2 Richardson number, eddy viscosity and Ozmidov scale

It was observed in the previous section that N_z is affected by both the Richardson number *Ri* and the tendency of the tidal straining mechanism to mix and stratify the water column. In order to analyse this relationship further, and the complex relationship of the turbulence and stratification, the change in *Ri* over a tidal cycle is examined. The profiles of the shear in the mean along-channel flow obtained from the ADCP measurements and density profiles from the CTD measurements are used in this analysis.

Since the density measurements did not always coincide with the centre of a 10-minute averaging period of the ADCP data, the latter were interpolated so that the times at which the shear is used to calculate *Ri* correspond to the times at which the CTD profiles were made. This was done in order to avoid any inaccuracies which might result from interpolation of the density profiles which were measured at approximately half-hourly intervals; the ADCP velocity measurements, with 10-minute averaging, are reasonably smooth, and therefore the interpolation might be expected to represent the true values with a reasonable degree of accuracy. Contour plots of *Ri* and other associated parameters: eddy viscosity, stratification length scale, density, shear and current velocity, are shown in Figure 5.3 and Figure 5.4 for the first and second intensive periods respectively. *Ri* in each case is plotted on a logarithmic scale, and normalised by 0.25, the critical value: any values below zero on the logarithmic scale therefore represent the times at which the Richardson number falls below its critical value of 0.25. The along-channel velocities at each level have been plotted in order to see how the Richardson number changes with the mean flow.

At neaps, there are three periods in which *Ri* is sub-critical [Figure 5.3(a)]. The first is between day numbers 79 to 79.15 during the latter part of the first flood, when the stratification is being eroded [panel (d)]. Low Richardson numbers are observed as high as 2.3 m above the bed, but above this level the residual stratification results in *Ri* remaining above its critical value. This is the period when the observed eddy viscosity reaches its maximum value [panel (b)]. The second period of low *Ri* is between day numbers 79.3 and 79.45, during the ebb, at about the time of the peak Reynolds stress. This time, values at or below the critical value are observed

throughout the water column, despite the stratification, but the eddy viscosity remains low at all levels. These low *Ri* values appear to be the result of very high shear in the mean current. The third period of low *Ri* is between day numbers 79.5 and 79.7, on the second flood, and is observed only in the lowest two depth cells. As in the case of the first flood, it occurs at the same time as the eddy viscosity increases, during the latter half of the flood, when the stratification low in the water column has been eroded.

In order to obtain a clearer indication of when stratification and tidal straining inhibit the growth of turbulent eddies, the Ozmidov scale $l_O = \left(\varepsilon / N^3\right)^{1/2} \approx \left(P / N^3\right)^{1/2}$ is plotted in panel (c). The time series of l_o closely follows that of the eddy viscosity, and both appear to show a strong inverse relationship with the Richardson number.

During the spring tidal period, *Ri* falls well below the critical value during peak flow in both ebb and flood directions in the lower half of the water column [Figure 5.4(a)]. Higher in the water column, at 4.3 m above the bed, *Ri* barely falls below 0.25 at any time in the tidal cycle. The lowest values at this level are seen on the ebb during the night (day number 87.1) when the stratification is lower than during the daytime ebb phases.

During the first ebb (day number 86.5 - 86.7) the shear [panel (e)] is high throughout the water column and the stratification reaches its peak [panel (d)] as the flow velocity reaches zero and changes direction [panel (f)]. This results in low Richardson numbers being observed through the entire water column and an increase in the eddy viscosity [panel (b)]. The low shear levels and relatively high stratification at the start of the flood (day number 86.8) result in high *Ri* values and low eddy viscosity. There then follows a short period of slightly higher shear combined with a well-mixed water column during the flood, which results in low *Ri* being observed (day numbers 86.8 to 86.9), accompanied by an increase in the eddy viscosity throughout the water column. Towards the end of the flood (day number 86.95), the extremely low shear results in high values of *Ri*, despite the negligible stratification levels, and the eddy viscosity falls. This pattern is repeated on the subsequent tidal cycles.

During the springs period, there is a greater difference between the patterns seen in the eddy viscosity and Ozmidov scale [panel (c)], although an inverse relationship with Ri is still present to some degree, particularly between Ri and l_o. At mid-depth, l_o and N_z follow a similar pattern, with a tendency to slightly higher values on the flood, albeit for a very short period. Near the bed, the two parameters track each other closely on the ebb, but are quite different on the flood, with l_o showing high values for a longer period than is seen in the eddy viscosity. This can be explained by an analysis of how each parameter is calculated; the parameters used in the calculation of N_z take into account the distance from the boundary, while those used to calculate l_o do not. The Ozmidov scale simply reflects how the eddy size is affected by stratification, not by distance from the boundary. Hence the high values near the bed simply indicate a region in which the stratification does not affect the growth of the eddies, the high turbulent production rate near the bed being adequate to overcome the effects of the stratification.

The main deviation from an inverse relationship between Ri and l_o is seen high in the water column, at about 4 m above the bed and higher. At this level, Ri remains at or below the critical value on both ebb and flood, but N_z and l_o are lower on the ebb than on the flood. This is because N_z and l_o implicitly incorporate the effects of tidal straining, which tends to mix the water column on the flood and stratify on the ebb, hence the water column is effectively less stratified on the flood and more stratified on the ebb than is implied by the local gradient Richardson number.

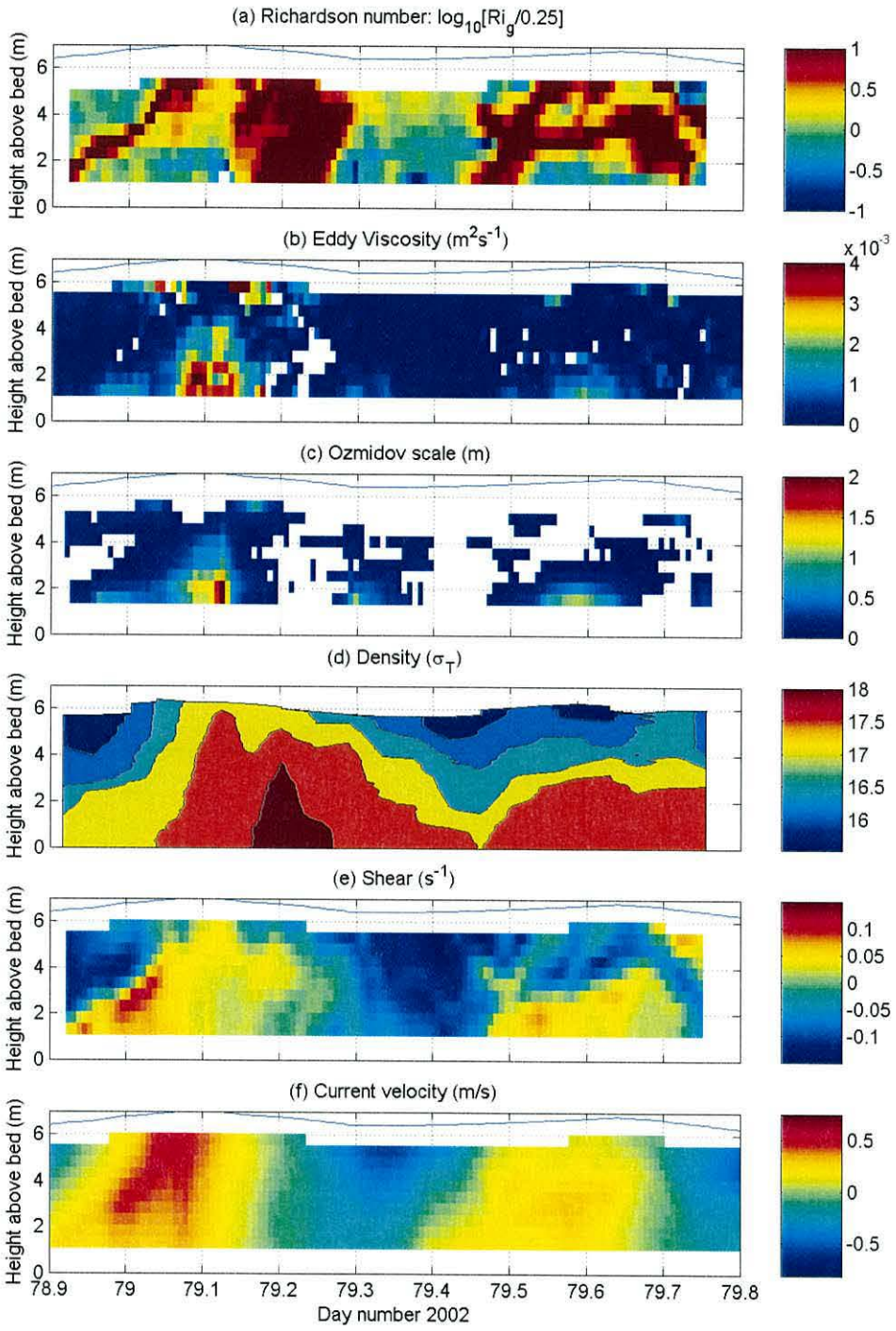

Figure 5.3: Richardson number and associated parameters for the first (neap) intensive period

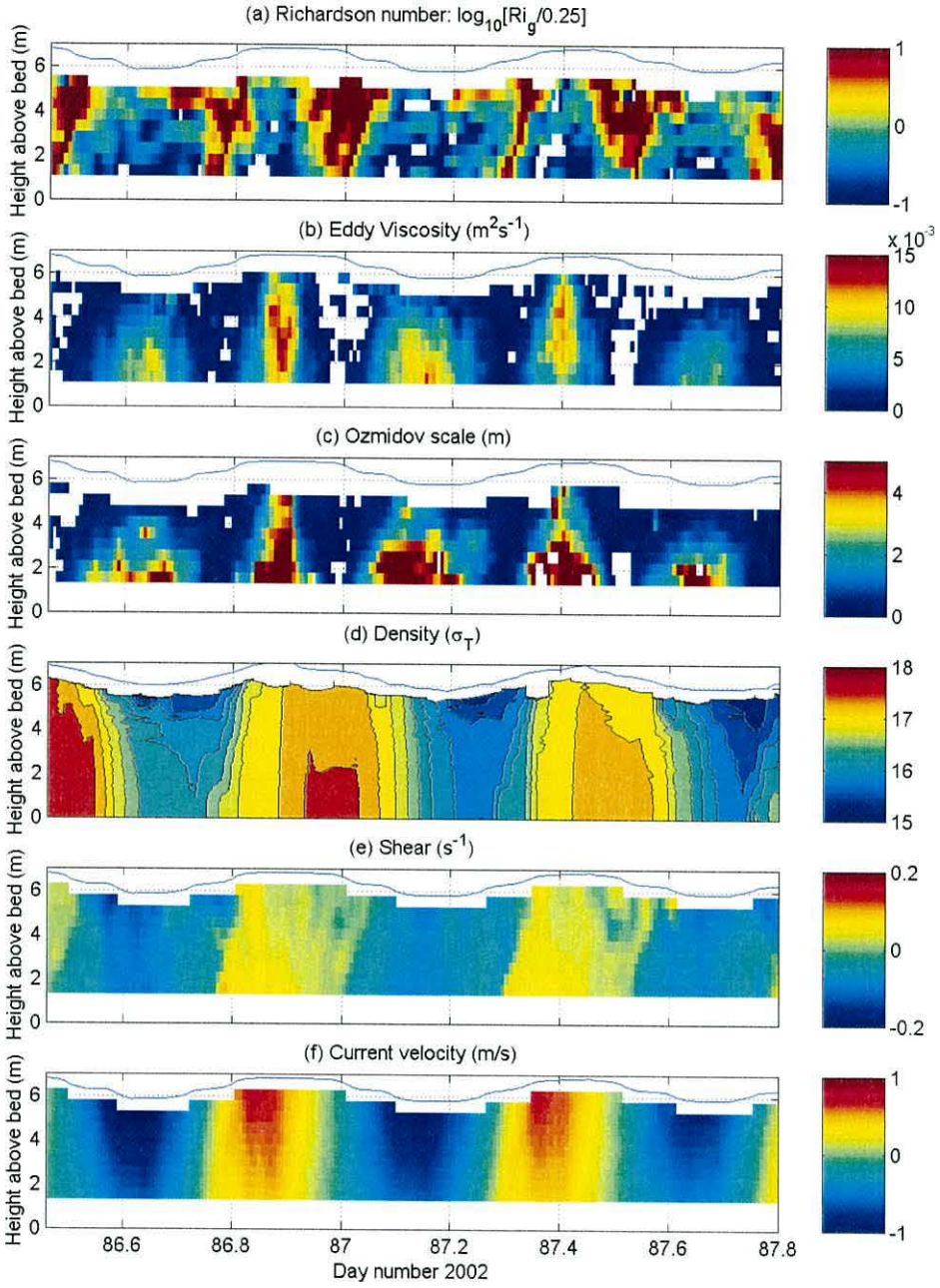

Figure 5.4: Richardson number and associated parameters for the second (spring) intensive period

5.2.1 Parameterizations of eddy viscosity using the Richardson number

In the previous section it was shown that there is evidence of an inverse relationship between N_z and Ri, with high Ri largely corresponding to low N_z and vice versa. The low values of Ri last for much longer on the ebb than on the flood, just as the periods of high eddy viscosity are longer on the ebb than on the flood. From the initial analysis in the previous section, it appears that N_z is governed by tidal straining as well as by Ri. A more rigorous analysis of the relationship between N_z and Ri will indicate to what extent tidal straining is important.

The relationship between the eddy viscosity and Richardson number has been the focus of several previous studies, where the object has been to parameterize the eddy viscosity in terms of the Richardson number. Parameterizations of this type are used in turbulence modelling applications and take the general form:

$$N_z = \xi + A_0(1+\alpha Ri)^{-\beta}$$

where A_0 is the eddy viscosity in the absence of stratification ($Ri = 0$), and α, β and ξ are constants to be determined empirically. Three such parameterizations are:

Munk and Anderson (1948):

$$N_z = A_0(1 + 10Ri)^{-1/2} \tag{5.2}$$

Pacanowski and Philander (1981):

$$N_z = A_0(1 + 5Ri)^{-2} + \nu \tag{5.3}$$

Bowden and Hamilton (1975):

$$N_z = 0.0005 + 0.0025H\hat{U}(1 + 7Ri)^{-1/4} \tag{5.4}$$

These three parameterizations will be referred to as MA, PP and BH respectively. The kinematic molecular viscosity, ν, in PP is at least an order of magnitude smaller than A_0, so can be neglected, as can the constant 0.0005 in BH. A_0 is assumed either to be a constant (MA and PP), or to be a tidally varying parameter $A_0 = 0.0025|\hat{U}|H$ where $\hat{U}$ is the depth mean velocity and H is the water depth (BH). The Richardson number used in BH and PP is an overall Richardson number Ri_o for the whole water column, given by:

$$Ri_o = \frac{gH\,\Delta\rho/\rho}{\hat{U}^2} \tag{5.5}$$

where $\Delta\rho$ is the top-bottom density difference. A single eddy viscosity for the entire water column results from the use of values of A_0 and Ri which are constant with depth, making direct comparisons with the present set of results difficult. It is also physically unrealistic, since N_z is expected to change substantially with distance from the boundaries, especially in a shallow, estuarine environment. One argument for using Ri_o in preference to the gradient Richardson number Ri, was that the measurements of $\partial u/\partial z$ were likely to be inaccurate due to the wide vertical spacing of current meters (Bowden, 1977). Since that deficiency has largely been overcome with the use of the acoustic Doppler current profiler, it seems reasonable to compare the present results with these parameterizations, but replacing Ri_o with Ri.

MA and PP were developed from observations in the ocean thermocline, with density differences largely due to temperature gradients, where flood-ebb asymmetry might be expected to be of no great importance, therefore these parameterizations assume a simple inverse power law relationship between the Richardson number and the eddy viscosity with no account made for the direction of flow. BH, however, was developed from observations in an estuarine environment, where the stratification and hence the Richardson number are higher on the ebb than on the flood, resulting in lower values of the eddy viscosity on the ebb.

A constant value for A_0 throughout the water column and over the tidal cycle is assumed in MA and PP, who estimate that it should be of order 5 x 10^{-3} m^2s^{-1}. This is of the correct order of magnitude for the present data set: if the r.m.s. value of $\hat{U}$ and the mean value of H are calculated for a whole number of tidal cycles, the result is a single value for $A_0 = 0.0025|\hat{U}|H \sim 0.008$ m^2s^{-1}. However, a more accurate picture might be obtained if the eddy viscosity for unstratified flow is allowed to vary with height above the bed and over a tidal cycle.

In Figure 5.5, the eddy viscosity calculated from each parameterization is plotted as a time series. The value of A_0 in the parameterizations is calculated from the eddy viscosity profile for unstratified steady flow using $A_0 = \kappa u_* z(1 - z/h)$ (Rippeth *et al.*

2002), using a value of u_* calculated from the observations using $u_*^2 = \left|-\overline{u'w'}\right|$ from the lowest depth cell of the ADCP centred at 1.3mab.

All three parameterizations shown in Figure 5.5 indicate a short period of high eddy viscosity on the flood with its maximum at mid-depth, which correlates well with the eddy viscosity calculated from the data. On the ebb, the parameterizations continue to predict the maximum at mid-depth, but at a slightly lower depth than on the flood due to the water being shallower. The data, however, show the maximum to be even lower in the water column and smaller than that predicted by all three models.

The local gradient Richardson number is low throughout the water column on the ebb, only reaching levels above the critical value near the surface on the flood and throughout the water column around slack water. The ebb lasts for longer than the flood, hence the low values of *Ri* last for longer on the ebb than on the flood. This results in the high values of eddy viscosity lasting for a longer period on the ebb than on the flood. At mid-depth, *Ri* is lower on the ebb than on the flood, resulting in the high mid-depth eddy viscosity from the parameterizations, showing the same pattern as the eddy viscosities estimated from the data.

Figure 5.6 shows these results using a non-dimensional form of the eddy viscosity N_z/A_0 ; the values obtained from the observations are normalized by A_0 as described above. The data are plotted separately for ebb and flood due to the differences between the two parts of the tidal cycle and the observed values for the upper and lower parts of the water column are represented by different symbols. The direction of flow in each depth cell is used to define the flood and ebb parts of the tidal cycle; due to the nature of the mean flow, therefore, at certain times the flow will be in the flood direction in one depth cell and in the ebb direction in an adjacent cell.

There is a general conformity to the models, with the highest observed eddy viscosity occurring at sub-critical values of *Ri*, although during the flood the correlation between *Ri* and N_z is fairly weak. At sub-critical Richardson numbers during the ebb, PP gives a better prediction of the observed values of N_z, particularly in the lower half of the water column, while MA tends to predict higher values than those observed.

It is concluded that the discrepancy between the measured eddy viscosity and that predicted from *Ri* is an indication that the eddy viscosity is not governed by the local Richardson number, but also by the effect of the tidal straining mechanism, which enhances mixing during the flood and stratification during the ebb. During the ebb, the 'effective' Richardson number, that is, a parameter which represents the true effects of buoyancy and mixing, may be higher than the local gradient Richardson number which has been measured.

The failure of the Richardson number parameterizations to accurately represent the profiles of eddy viscosity appears to be a result of the local Richardson number lacking a component which represents the horizontal density gradient. It has been suggested that the effect of the horizontal density gradient on the local turbulent parameters can be expressed in terms of a 'horizontal Richardson number' (Ri_x) (Monismith *et al.*, 1996; Stacey *et al.* 2001), which takes the form:

$$Ri_x = \frac{g(\partial\rho/\partial x)H^2}{\rho u_*^2} \tag{5.6}$$

If such a horizontal Richardson number were to be combined with the local gradient Richardson number, it may be possible to parameterize N_z more accurately. However, a Richardson number of this type still lacks a component which represents the direction of flow, and the tendency of the velocity shear and the horizontal density gradient to increase the stratification on the ebb and decrease it on the flood. A horizontal Richardson number which does take into account the direction of flow is analogous to the ratio of the rate of change of the potential energy anomaly φ to the rate of production of TKE.

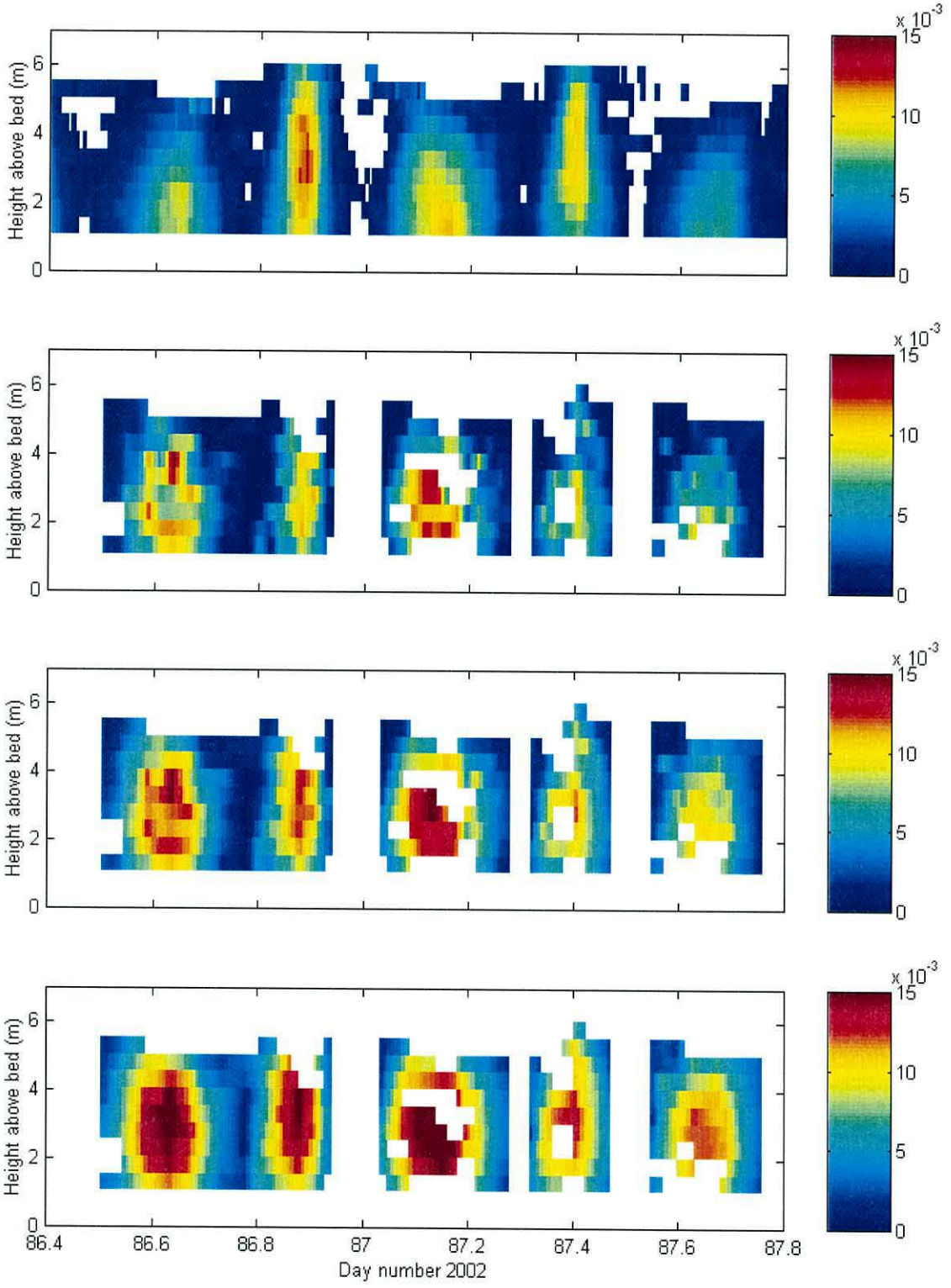

Figure 5.5: Eddy viscosity ($m^2\ s^{-1}$) from (a) data using $N_z = -\overline{u'w'}/(\partial u/\partial z)$; Richardson number parameterizations using (b) Pacanowski and Philander; (c) Munk and Anderson and (d) Bowden and Hamilton. Blank regions indicate negative values of Ri or N_z.

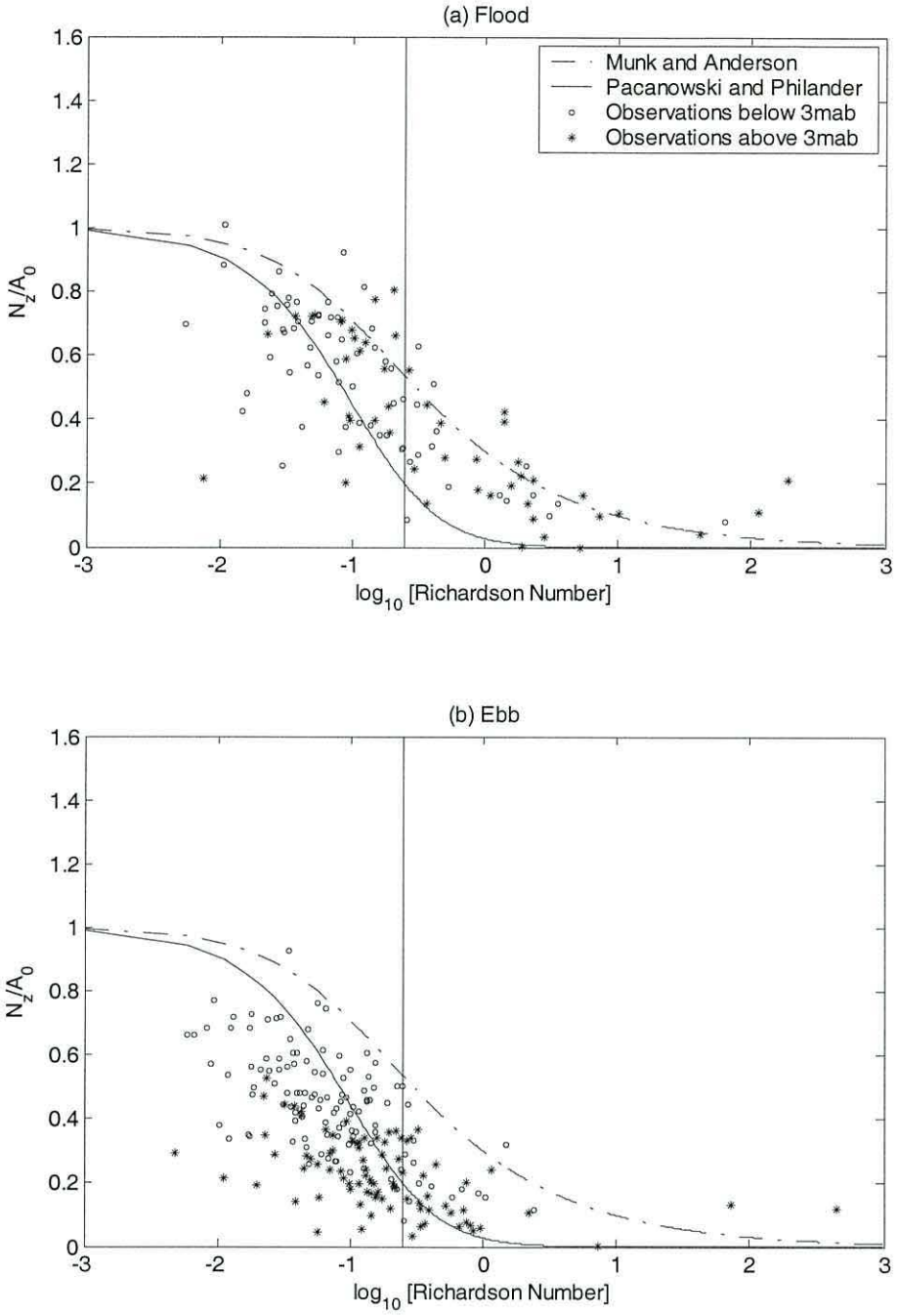

Figure 5.6: Eddy viscosity calculated from the data using $N_z = \overline{u'w'_R}/\partial\overline{u}_R/\partial z$ for the bottom 7 depth cells on the second (spring) intensive period and normalized using a value of $A_0 = \kappa u_* z(1 - z/h)$, where $u_*^2 = \left|-\overline{u'w'}\right|$ in the lowest depth cell, compared with those from the Munk - Anderson parameterization (dotted line) and the Pacanowski - Philander parameterization (solid line). The observations are plotted separately for flood and ebb and for the upper and lower parts of the water column. The solid vertical line indicates the critical value of $Ri = 0.25$.

5.3 Drag Coefficient: Relating the friction velocity to the depth mean flow

It is commonly held that the friction velocity u_* is related to the depth mean flow $\hat{U}$ according to a quadratic drag law $u_*^2 = C_D \hat{U}^2$ where C_D is a constant of order 10^{-3}; a typical shelf sea value is about 0.0025 (Soulsby, 1983). Alternatively, a drag coefficient can be determined using the velocity at a fixed height above the bed; a common way of doing this is to use the velocity at 1m above the bed. This method normally yields a slightly higher value of the drag coefficient (C_{100}), since the velocity near the bed is usually lower than the depth mean value. Before this relationship can be analysed, it is necessary to ascertain whether there is a phase difference between the mean velocity and the stress near the bed. From careful visual inspection of the time series of τ_b compared with that of $\hat{U}$ (and τ_b compared with that of U_b, where U_b is the velocity in the bottom depth cell of the ADCP, centred at 1.3 m above the bed), and by performing a simple tidal analysis, using the M_2 tidal component only, it is observed that there is a phase delay of τ_b compared to $\hat{U}$ and U_b of about 11°, or 20 minutes. The lagged value of $U_b|U_b|$ (i.e. U_b at time t-20 minutes) is plotted in Figure 5.7, with the Reynolds stress at the same height at time t.

The square of the friction velocity, $u_*^2 = |\tau_b|/\rho$ is now plotted against $\hat{U}|\hat{U}|$ in Figure 5.8(a) for the data from the second (springs) deployment of the 1.2MHz ADCP, with the velocity lagged by 20 minutes. A slightly clearer picture is obtained when u_*^2 is plotted against $U_b|U_b|$ [panel (b)].

A linear regression was performed on τ_b versus $\hat{U}|\hat{U}|$ and τ_b versus $U_b|U_b|$. The drag coefficient from the regression of τ_b on $\hat{U}|\hat{U}|$ is 1.03×10^{-3} and the fit to the data is good, with $r^2 = 0.89$. From the regression of τ_b on $U_b|U_b|$, a value of $C_{100} = 1.7 \times 10^{-3}$ is obtained (C_{100} is the drag coefficient using the velocity at 1.3m above the bed). These estimates of the drag coefficient, however, are considerably lower than the 'typical' value mentioned above.

A visual inspection of Figure 5.8 also suggests that a drag law which includes a component which varies with the mean flow speed might produce a better fit to the

data. Such a law would take the form $u_*^2 = C_D\hat{U}|\hat{U}|\left(1 + a\hat{U}\right)$. As a first approximation to such a law, the data are split into 'fast' and 'slow' flow speeds and a linear regression performed on each part of the data set separately to see if there is a significant difference in the drag coefficient obtained. The 'slow' flow speeds are defined as $U^2 < 0.1$ m^2 s^{-2}, and 'fast' flow speeds as $U^2 > 0.1$ m^2 s^{-2}, with the flood and ebb phases of the tidal cycle being considered separately for fast flows. The value of 0.1 m^2 s^{-2} was chosen, since this is the approximate value at which the relationship between τ_b and $U_b|U_b|$ changes; it is shown as a dashed line in Figure 5.7.

The results of the analysis for different flow speeds is shown in Table 5.1 and indicates that the drag coefficient is significantly lower for slow flows: C_D has a mean value of 0.67 x 10^{-3} and C_{100} a mean value of 1.11 x 10^{-3}. For fast flowing currents, C_D takes values of 1.34 x 10^{-3} (flood) and 1.21 x 10^{-3} (ebb), while the values of C_{100} are 2.56 x 10^{-3} and 2.04 x 10^{-3} respectively. Although the mean values for the flood and ebb at times of fast flow are different, the differences are not significant, due to the relatively large uncertainty at these times. The appropriate regression lines are shown in Figure 5.8: the solid lines indicate the three regression lines for slow and fast flow; the dashed line indicates the regression line for the whole data set.

The conclusion from this analysis is that a quadratic drag law must be modified to include a flow-related component, since the stress is proportionally greater at times of high flow than at times of slow flow.

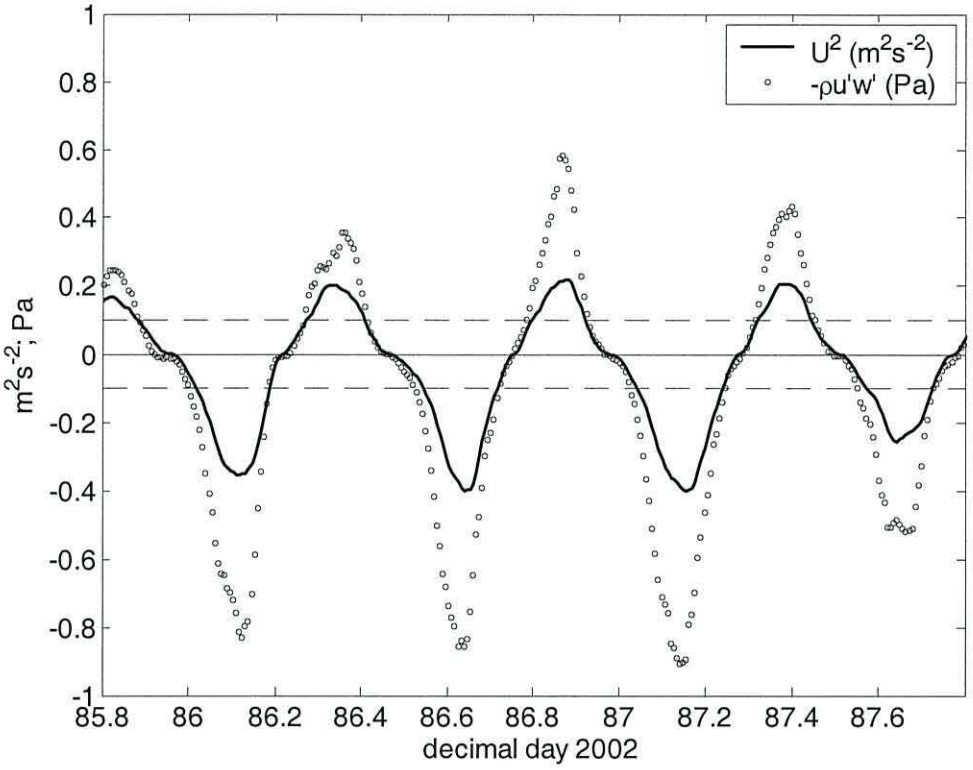

Figure 5.7: Time series of Reynolds stress, with velocity at time – 20 minutes. The dashed lines show $U^2 = 0.1$ m^2 s^{-2}.

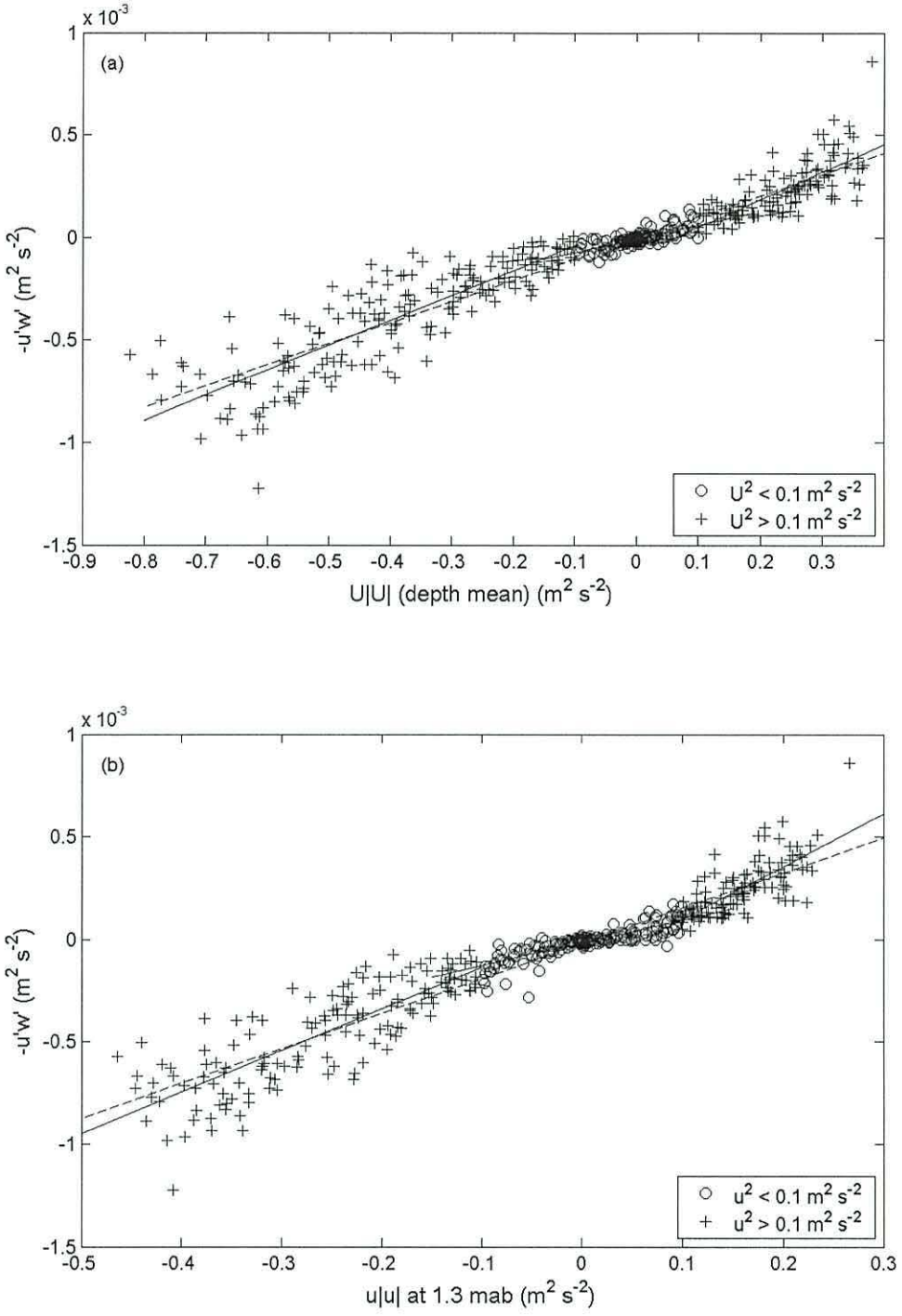

Figure 5.8: Reynolds stress in bottom depth cell of the ADCP (representing τ_b) plotted against (a) $\hat{U}|\hat{U}|$, where $\hat{U}$ is the depth mean along-channel velocity and (b) $U_b|U_b|$, where U_b is the along-channel velocity in the lowest depth cell of the ADCP (1.3 m above the bed).

Table 5.1: The drag coefficient and its 95% confidence limits. Column (a) gives the value of C_D (or C_{100}) from regression; (b) gives the sample standard deviation; (c) is the maximum value of C_D (or C_{100}) (columns (a) plus (b)); (d) the minimum value of C_D (or C_{100}) (columns (a) minus (b)); (e) is the correlation coefficient of regression, r^2; and (f) the degrees of freedom of the sample.

	(a)	(b)	(c)	(d)	(e)	(f)
	C_D	+/-	max C_D	min C_D	r^2	d.o.f.
All data using $\hat{U}$	1.03×10^{-3}	0.03×10^{-3}	1.06×10^{-3}	1.00×10^{-3}	0.89	470
$\hat{U}^2 < 0.1$ m^2 s^{-2}	0.67×10^{-3}	0.09×10^{-3}	0.76×10^{-3}	0.57×10^{-3}	0.57	150
$\hat{U}\lvert\hat{U}\rvert > 0.1$ m^2 s^{-2}	1.34×10^{-3}	0.20×10^{-3}	1.54×10^{-3}	1.15×10^{-3}	0.58	135
$\hat{U}\lvert\hat{U}\rvert < 0.1$ m^2 s^{-2}	1.21×10^{-3}	0.11×10^{-3}	1.32×10^{-3}	1.10×10^{-3}	0.73	181

	C_{100}	+/-	max C_{100}	min C_{100}	r^2	d.o.f.
All data using U_b	1.71×10^{-3}	0.05×10^{-3}	1.77×10^{-3}	1.66×10^{-3}	0.90	470
$U_b^2 < 0.1$ m^2 s^{-2}	1.11×10^{-3}	0.09×10^{-3}	1.20×10^{-3}	1.01×10^{-3}	0.73	204
$U_b\lvert U_b\rvert > 0.1$ m^2 s^{-2}	2.56×10^{-3}	0.43×10^{-3}	2.99×10^{-3}	2.13×10^{-3}	0.55	116
$U_b\lvert U_b\rvert < 0.1$ m^2 s^{-2}	2.04×10^{-3}	0.23×10^{-3}	2.27×10^{-3}	1.81×10^{-3}	0.68	146

5.4 Dynamical Balance

The dynamical balance equation is based on Newton's second law of motion, so by careful measurement of the accelerations present and the main forcing terms producing these accelerations, a greater understanding of the dynamical processes in the York River estuary may be gained. A second aim in this particular case is to further test the validity of the Reynolds stress estimates, using the approach of Rippeth *et al.* (2002).

The simplified along-channel momentum balance equation in linearized, depth-integrated form, can be written:

$$-\frac{\tau_b}{\rho h} = \frac{\partial U}{\partial t} + g\frac{\partial \eta}{\partial x} \tag{5.7}$$

where $\partial U/\partial t$ is the depth averaged acceleration estimated from the ADCP. The pressure gradient term, $g\,\partial\eta/\partial x$ is estimated from the tide gauge data and the distance between them (26.7 km). The stress divergence term $-\tau_b/\rho h$ is estimated from the Reynolds stress near the bed ($\tau_b = -\rho\overline{u'w'}$ in the lowest depth cell; hence τ_b is positive on the flood) and the total depth of the water column; h = total depth – 1.3 m to compensate for the unsampled region near the bed.

It should be noted here that due to an unforeseen problem with the levelling of the tide gauges, and damage due to Hurricane Isabel, the absolute levels at the two sites are not available, so the mean was extracted from each time series of water depths at Taskinas Creek and Gloucester Point in order to estimate the pressure gradient term $g\,\partial\eta/\partial x$. Any errors in the estimate of the tide gauge levels will not affect the shape of the graphs, only the position of the zero line.

A time series of the three terms in equation (5.7) for the second deployment of the 1.2 MHz ADCP (over the spring tidal period) is shown in Figure 5.9(a). Panel (b) of the same figure shows the left hand side and right hand side of equation (5.7) plotted as a time series. These are in reasonably good agreement on the flood (the negative values on the graph). However, on the ebb, the stress divergence term greatly exceeds the sum of the other two terms at peak flow, while being of similar magnitude or lower at

times of slower flow. This discrepancy occurs at the times when there is a large peak in the Reynolds stress, which was described in section 4.3.3 (see also figure 4.14) and is associated with very strong flows.

In order to check that these peaks are not simply an artefact of the way in which the ADCP data have been processed, the dynamical balance calculations were repeated, but this time, the stresses estimated from the ADV at 1.12 m above the bed (mab) were used instead of those from the ADCP at 1.3 mab. The other terms were calculated as in the previous analysis, from the ADCP and tide gauge data. The results of this analysis are plotted in Figure 5.9(c) which shows similar peaks in $-\tau/\rho h$ to those in panel (b).

One possible explanation for the peaks in the stress divergence term, which are not reflected in the other terms, is that the assumption of a linear stress profile does not hold. In Figure 5.2(c) it was seen that the stress profile was approximately constant in the near bed region at times of peak flow on both ebb and flood. To see if this feature occurs at all times of the tidal cycle, τ in depth cell 2 at 1.8 mab is plotted against τ at 1.3m above the bed for the second deployment of the 1.2MHz ADCP at springs (30-minute means in both cases) in Figure 5.10. The solid line on the graph indicates equality; a linear regression of τ in depth cell 2 (τ_2) against τ in depth cell 1 (τ_1) gives: $\tau_2 = (0.988 \pm 0.016)\tau_1$ with r^2=0.99 (156 degrees of freedom), with some profiles actually indicating a decrease from depth cell 2 to depth cell 1. For a linearly varying stress profile in a water column of mean depth H = 6.5m, with depth cell 1 centred at h_1 = 1.3m above the bed and depth cell 2 centred at h_2 = 1.8m above the bed, $\tau_2/\tau_1 = (H - h_2)/(H - h_1) = 4.7/5.2 = 0.903$. An assumption of linearly varying stress between the bed and the surface which was based on the stress in the lowest depth cell would therefore tend to overestimate the stress at the bed, particularly at times of peak flow, when τ has its maximum value.

The dynamical balance is further investigated by plotting the left and right hand sides of equation (5.7) against each other [Figure 5.11(a)]. A linear regression on the data yields the following result:

$y = 0.985x + 1.6 \times 10^{-5}$ $\quad r^2 = 0.589$ $\quad$ (467 d.o.f.)

This indicates that the terms are of the right order, but the fit is not particularly good. There is also a large number of points along the x-axis which represent the low values of the bottom stress which occur even when the other terms are relatively large. During the strongest spring tides, the balance between the two sides of the momentum equation appeared to be closer, as indicated in panel (b) of Figure 5.11, for day numbers 86.4 to 87.5. The linear regression for this period yields:

$y = 1.34x - 4.6 \times 10^{-7}$ $\quad r^2 = 0.703$ $\quad$ (159 d.o.f.)

For the flood part of the tidal cycle only:

$y = 1.23x + 5.2 \times 10^{-8}$ $\quad r^2 = 0.697$ $\quad$ (72 d.o.f.)

For the ebb part of the tidal cycle only:

$y = 1.78x - 1.8 \times 10^{-5}$ $\quad r^2 = 0.405$ $\quad$ (85 d.o.f.)

Despite the closer agreement of the two sides of the balance equation, the high values of τ on the ebb are still present, as are the very low stresses which persist for a relatively high range of values of the other two terms.

In the equation for the dynamical balance (5.7), the advective, baroclinic and Coriolis terms were neglected, since these are normally expected to be much smaller than the other three terms. If these terms are included, the dynamical balance equation in the along-channel direction with the acceleration terms (including the advective and Coriolis terms) on the left hand side and the forcing terms (tidal, baroclinic and frictional) on the right can be written:

$$\frac{\partial u}{\partial t} + u\frac{\partial u}{\partial x} + v\frac{\partial u}{\partial y} + w\frac{\partial u}{\partial z} - fv = -g\frac{\partial \eta}{\partial x} + \frac{gh}{\rho}\frac{\partial \rho}{\partial x} - \frac{\tau_b}{\rho h} \qquad (5.8)$$

In a uniform channel, the flow can be considered to be uniform along and across the channel, so the advective terms, like the Coriolis and baroclinic terms, are expected to be small. However, in order to check that these terms were not, in fact producing the discrepancy in the balance, the Coriolis and baroclinic terms were calculated. In addition, a corrective term was calculated, to estimate the magnitude of the effect of the earth's rotation on the use of tide gauges on opposite sides of the estuary. The measured surface slope between the two tide gauges (η) represents the sum of the true surface slope along the channel (η_x) and the difference in height between the two sides of the channel (η_y). The momentum balance in the transverse direction is

$fu = -g\,\partial\eta_y/\partial y$, assuming all other terms are negligible. Therefore:

$$\Delta\eta = \frac{\Delta\eta_x}{\Delta x}\Delta x + \frac{\Delta\eta_y}{\Delta y}\Delta y = \Delta\eta_x - \frac{fu}{g}\Delta y \tag{5.9}$$

where Δy is the width of the channel at the point of the observations (3300 m). Hence:

$$\frac{\Delta\eta_x}{\Delta x} = \frac{\Delta\eta}{\Delta s} + \frac{fu}{g}\frac{\Delta y}{\Delta s} \tag{5.10}$$

where Δs is the distance between the two tide gauges, and the left hand side of equation (5.10), which is the true surface slope term, can be calculated from the two measured terms on the right hand side. Data were not available to check the magnitude of the advective terms, but the other five terms in equation (5.8), along with the corrective term for the effect of the two tide gauges being on opposite sides of the estuary, are plotted in Figure 5.12. This shows that the three main terms in equation (5.7) [panels (a) to (c)] are of order 10^{-4} ms^{-2}, while the baroclinic term [panel (d)] is of order 10^{-5} ms^{-2} and the Coriolis term [panel (e)] of order 10^{-6} ms^{-2}. The corrective term for the surface slope [panel (f)] is also of order 10^{-6} ms^{-2}. These three smaller terms are therefore not sufficient to account for the discrepancy in the dynamical balance.

In order to analyse this discrepancy further, the residuals are calculated using all the dynamical balance terms in equation (5.8) apart from the advective terms. All the terms are taken on to one side, and the sum plotted in Figure 5.12(g) In this panel the excess in the stress divergence term at peak ebb can clearly be seen as a large negative peak (day numbers 86.1, 86.6 and 87.15). Also visible in this panel is the low stress divergence around slack water and also during the flood phase of the tidal cycle when the flow is relatively weak: during these periods there is a positive peak in the residuals. A fourier analysis of the residuals [Figure 5.13(c)] shows strong signals at the M_2, M_4 and M_6 frequencies, as well as some lower frequency effects. This suggest that while the dynamical balance terms used account for most of the signal, there are still some effects at these frequencies which are not accounted for.

If it is assumed that the stress estimates from both instruments are reasonably accurate, one or more of the following may account for the failure of the momentum

terms to balance: (a) the deviations of the stress profile from linear result in errors in the vertically integrated estimate of the stress, (b) the advective terms have a significant effect due to transverse flows or (c) the non-uniformity of the channel between the two tide gauges, in terms of width, depth and bottom stress is significant.

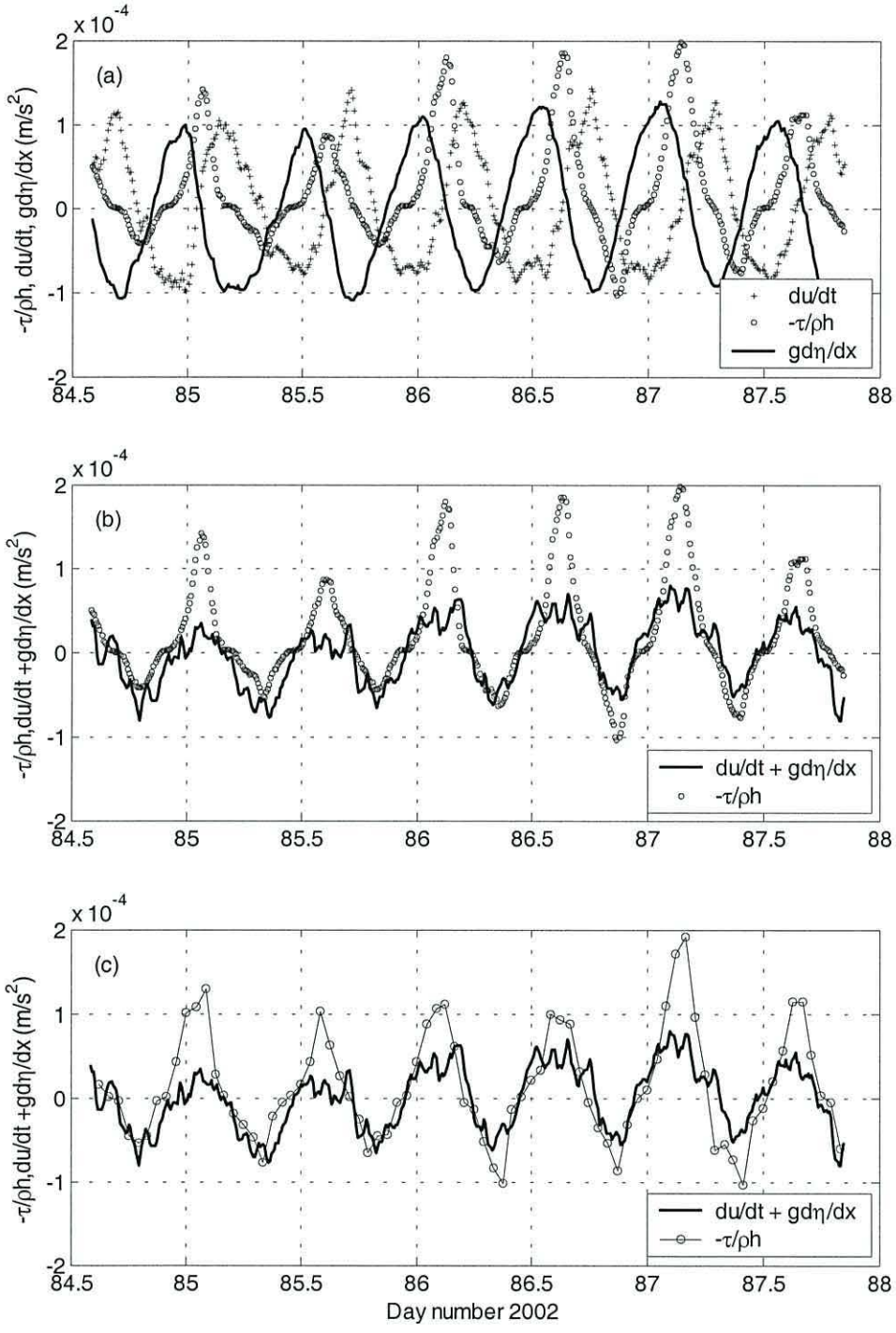

Figure 5.9: Dynamical Balance terms for second 1.2 MHz ADCP deployment showing (a) all three dominant terms using $-\tau/\rho h$ from the ADCP; the two sides of equation (5.7) using (b) $-\tau/\rho h$ from the ADCP and (c) $-\tau/\rho h$ from the ADV

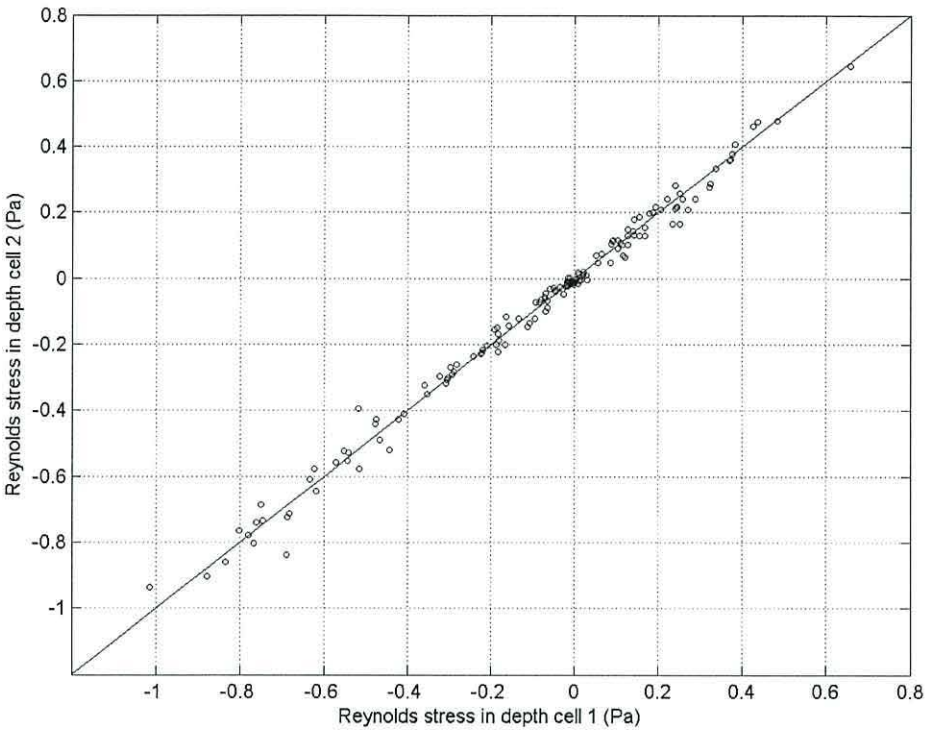

Figure 5.10: Comparison of Reynolds stress in depth cells 1 and 2. The solid line indicates equality of the two values.

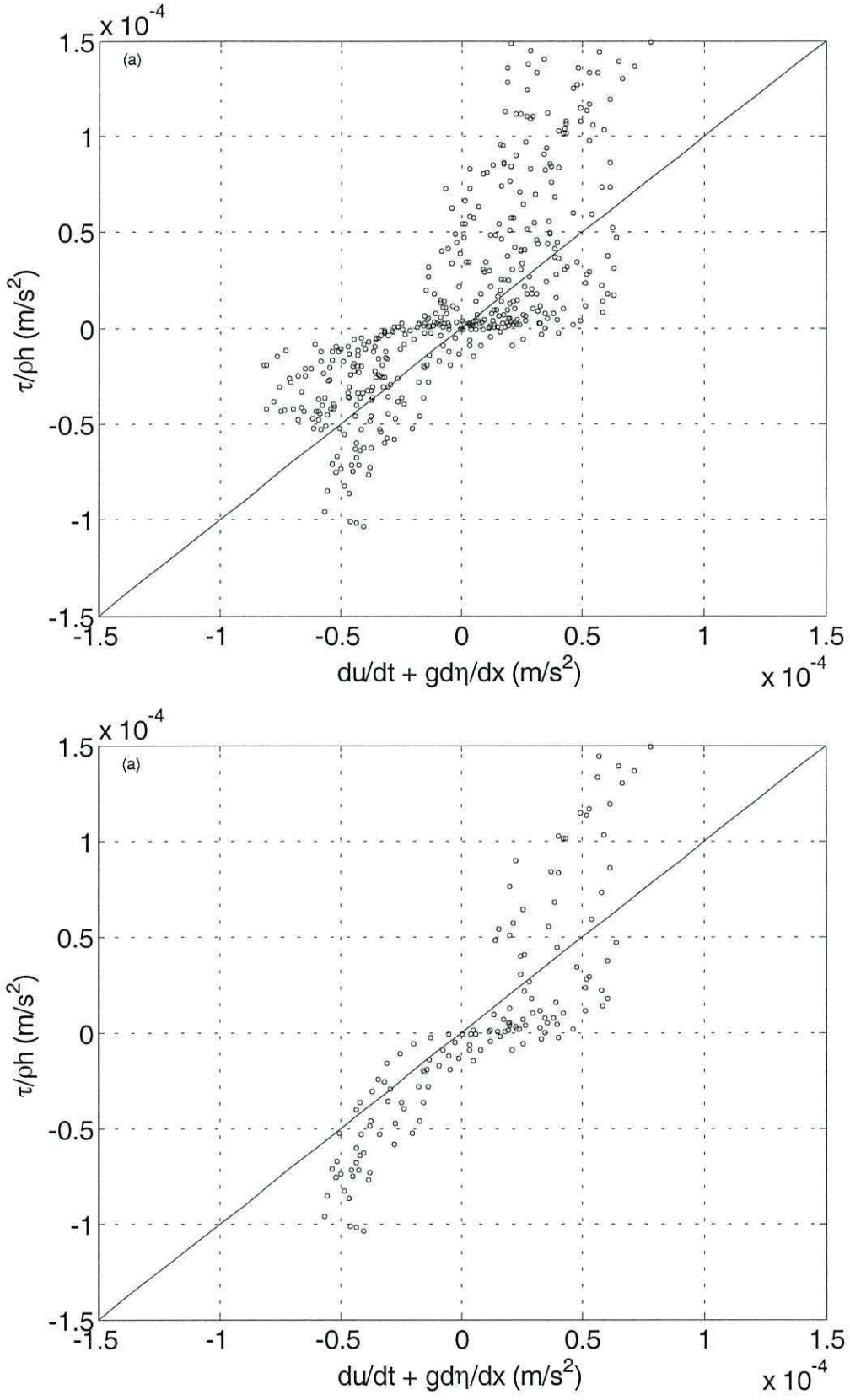

Figure 5.11: Dynamical Balance for the three dominant terms for (a) the whole of the second 1.2 MHz ADCP deployment and (b) for day numbers 86.4 to 87.5.

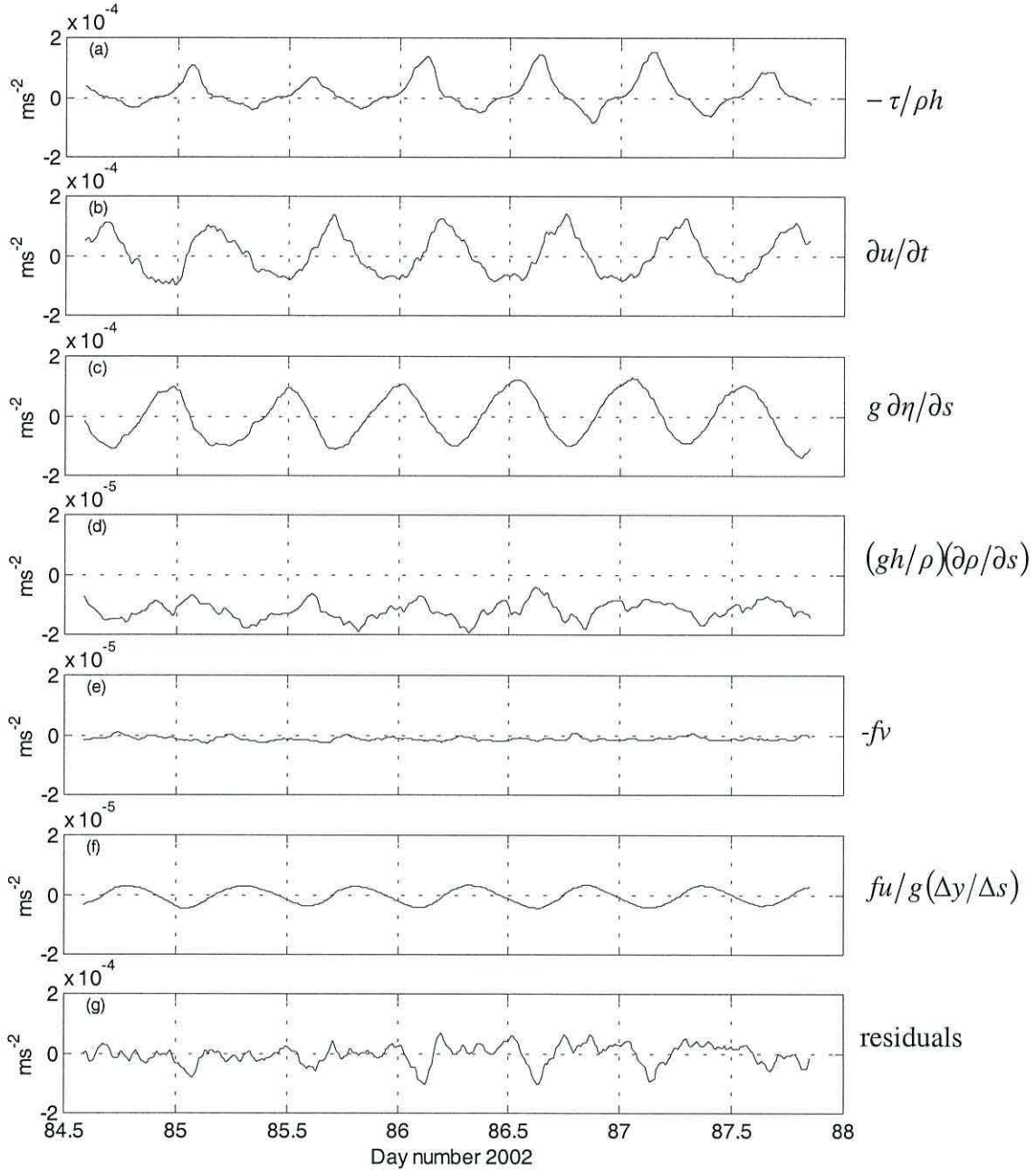

Figure 5.12: Dynamical balance terms: (a) $-\tau/\rho h$; (b) $\partial u/\partial t$; (c) $g\,\partial\eta/\partial s$; (d) $(gh/\rho)(\partial\rho/\partial s)$; (e) $-fv$; (f) $fu/g\,(\Delta y/\Delta s)$ and (g) residuals when terms (a) to (f) are taken onto one side of the dynamical balance equation.

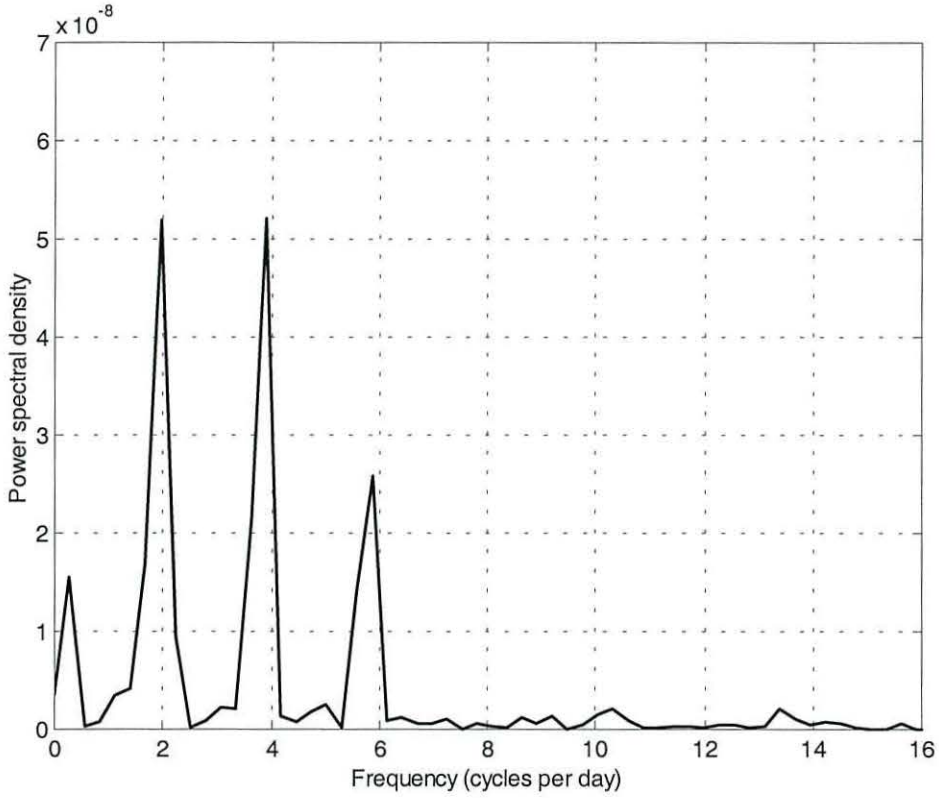

Figure 5.13: Fourier transform of residuals of dynamical balance terms

5.5 Summary

In this chapter, the effects of tidal straining and stratification on the turbulent motions was analysed. Tidal straining inhibits the growth of eddies on the ebb, when it tends to stratify the water column, and promotes eddy growth on the flood, when it enhances mixing. The gradient Richardson number, which is based purely on the local stratification, takes no account of this effect, and is therefore inadequate as a predictor of eddy viscosity. An improvement could be made in eddy viscosity parameterizations using the Richardson number by incorporating a horizontal Richardson number to account for the action of tidal straining.

The drag coefficient and momentum balance were analysed, and it was shown that the drag coefficient, which relates the stress at the bed with the mean flow, is better represented by a function with a flow-related component than by the more conventional quadratic drag law. The dynamical balance is incomplete, particularly at peak ebb; this is most likely to be due to inaccurate measurement of stress at the bed, transverse flows or channel irregularities.

CHAPTER 6

The York River Estuary: Analysis of Uncertainties and Errors

Sections 6.1 to 6.4 consist of extracts from a published paper (Williams and Simpson, 2004).

6.1 Uncertainties in measurements of stress, shear and TKE production rate

Analysis of uncertainties in the calculation of the Reynolds stress and TKE production rate were made using the methods outlined in chapter 3. For this analysis, the data from the second deployment of the 1.2MHz ADCP in the York river estuary were used. Another data set from the Menai Strait (Rippeth *et al.*, 2002) was also analysed in a similar manner in order to determine how much improvement in the accuracy of the turbulence measurements had been achieved through the use of mode 12 instead of the standard mode 1 used in the Menai Strait. In the Menai Strait, along-beam velocity data were collected every 2 seconds using a 4-ping ensemble average; thus 300 values were used to calculate the variances and the Reynolds stresses compared with 600 values used in the York river estuary where mode 12 was used to record velocities every second.

Further estimates of noise levels were made from along-beam velocities measured in Vivian quarry near Llanberis, North Wales, a disused and now flooded slate quarry. The water at Vivian quarry is about 20m deep, and since there is no tidal or river flow, the water can be assumed to be still, apart from wind effects. These data are used to attempt to quantify the instrument noise in still water and compare with the values provided by RDI. The instrument was deployed in the quarry for short periods facing downwards through the water column in different configurations and the along-beam velocities recorded as for the two data sets. These data will be referred to as the 'quarry' data. For the purpose of this section, the York River estuary and the Menai Strait data sets will be referred to as 'mode 12' and 'mode 1' respectively. In all three data sets, a depth cell size of 0.5 m was used.

Figure 6.1 shows the standard deviation of the Reynolds stresses calculated from the observations using equation 3.23 in chapter 3:

$$\sigma_R = \left(\frac{\gamma_R \left(\left(\overline{b_1'^2}\right)^2 + \left(\overline{b_2'^2}\right)^2 \right)}{2M \sin^2 2\theta} \right)^{\frac{1}{2}}$$

plotted against the associated Reynolds stress. The factor γ_R for the Reynolds stresses was estimated as having a median value of ~1.6 for mode 1 and ~1.7 for mode 12 (Figure 6.2). If a linear regression is performed on the data shown in Figure 6.1, the following results are obtained:

Mode 1: $\rho\sigma_R = 0.151\rho\left|\overline{u'w'}\right| + 0.074$ ($r^2 = 0.93$)

Mode 12: $\rho\sigma_R = 0.104\rho\left|\overline{u'w'}\right| + 0.018$ ($r^2 = 0.95$)

indicating that the instrument noise is reduced from ~0.07 Pa in mode 1 to less than 0.02 Pa in mode 12. The reduction in the gradient from 0.151 to 0.104 indicates that the uncertainty in the calculated values due to the variance in the Reynolds stresses from turbulent motions has also been reduced by using a greater number of ensembles to estimate the stress. The reduction is consistent with the theory, since if twice as many ensembles are used to calculate the Reynolds stress, the standard deviation due to the turbulent fluctuations should be reduced by a factor of $\sqrt{2} \approx 1.41$. Here, the reduction is by a factor of ~1.45.

The along-beam velocity standard deviation (σ_N) from the trials at the quarry were estimated as 0.0217 ms^{-1} for mode 1 (using a 4-ping mean as in the observations) and 0.0184 ms^{-1} for 1 second averages at 10Hz in mode 12. Using the data from the two deployments, we get values of 0.018ms^{-1} for mode 1 and 0.014ms^{-1} for mode 12. These are slightly higher than the values of 0.0168ms^{-1} for mode 1 and 0.0106ms^{-1} for mode 12 indicated by RDI's *PlanADCP* configuration software.

For still water, both the along-beam velocity and the variance due to turbulent fluctuations are zero, so the variance in the Reynolds stress can be determined using $\sigma_R^2 = \frac{\sigma_N^4}{M \sin^2 2\theta}$ (equation 3.26, chapter 3). From the quarry results, the standard deviation of the Reynolds stress due to instrument noise, is $\rho\sigma_R = 0.0436$ Pa in mode 1 (using M=300) and $\rho\sigma_R = 0.0219$ Pa in mode 12 (using M=600). The larger value

obtained for the minimum standard deviation of the Reynolds stress for mode 1 using the regression method is due to the greater scatter of the data points around the regression line, despite a good fit to the line. This can be seen clearly in Figure 6.1, where the median value of the standard deviation for near-zero Reynolds stress is less than 0.06 Pa, consistent with the quarry value.

The uncertainties in the Reynolds stresses were obtained using the semi-empirical method outlined in section 3.4.2. In order to check on the accuracy of this method, further estimates of the uncertainties were made directly from the data. The Reynolds stresses for depth cell 2 were sorted according to the associated value of the Reynolds stress in depth cell 1, since a linear regression of the stress in cell 2 on the associated stress in cell 1 yields a correlation coefficient, r^2, of more than 97% for both data sets (Figure 6.3(a) and (b)). The data were sorted into 24 bins, with an equal number of data points in each. For each bin the standard deviation was calculated as the r.m.s. value of the deviations from the linear trendline, and plotted against the mean Reynolds stress for that bin. The results for this are shown in Figure 6.4, together with the semi-empirical values obtained from equation (3.23). Further estimates of the uncertainty at hourly intervals for a 25-hour subset of the mode 12 data were made using a bootstrap method, following that used by Lu and Lueck (1999b), in which the along-beam velocity fluctuations were resampled to obtain 1000 new series of 600 data points for each 10-minute period, which were then used to obtain 1000 new estimates of the 'stress'. The 95% confidence limit obtained using this method is in very close agreement with the value of $2\sigma_R$ obtained using the other methods.

For still water, the variance of the shear is given by (see equation 3.30, chapter 3):

$$\sigma_S^{\,2} = \frac{\sigma_N^{\,2}}{M(\Delta z)^2 \sin^2\theta}$$

For mode 1, the minimum value of σ_S from the observational data is 4.19 x 10^{-3} s^{-1}. From the quarry noise tests, the standard deviation of the shear due to instrument noise alone is 3.67 x 10^{-3} s^{-1}, consistent with the observational values. For mode 12 the results are even closer: 2.20 x 10^{-3} s^{-1} from the quarry and 2.09 x 10^{-3} s^{-1} from the observations.

Figure 6.5 shows a similar plot to Figure 6.1, this time for the standard deviation of the TKE production rate plotted against the production rate. The gradient here is reduced from ~ 0.194 to ~0.128, (r^2 values are approximately 0.97 for both) indicating that the percentage error in the TKE production rate estimates has been reduced from over 19% to less than 13%. The reduction factor here is ~1.5, compared to a factor of $\sqrt{2}$ from theory. A direct method, similar to that used for the Reynolds stresses, was used to check the accuracy of the calculated values of the standard deviation of the TKE production rate which were obtained using the method outlined in section 3.4.4. The values of P in depth cell 2 were divided into bins according to the associated value of P in depth cell 3, since again, there is a strong linear correlation between the estimated value of P in adjacent depth cells (Figure 6.3(c) and (d)) with r^2 values of 93% for mode 1 and 96% for mode 12. Removing the linear trend, the standard deviation of P is represented by the r.m.s. value of the deviations from the line. These results are shown in Figure 6.6. The direct estimates of the standard deviations of TKE production rate are in satisfactory agreement with the semi-empirical values for both mode 1 and mode 12.

The standard deviation of the TKE production rate due to each of the three terms in equation (3.31) are plotted for both mode 1 and mode 12 in Figure 6.7, along with the total standard deviation. About 85% of the variance in the TKE production rate estimates is due to the second term in equation (3.31): $\left(\rho^2(\partial u/\partial z)^2 {\sigma_R}^2\right)$ at times of high flow, with most of the remaining 15% due to the first term $\left(\rho^2\left(\overline{u'w'}\right)^2 {\sigma_S}^2\right)$ and the final term $\left(\rho^2 {\sigma_S}^2 {\sigma_R}^2\right)$ making a negligible contribution at least an order of magnitude smaller than either of the other two terms. At times of low flow, the final term is of the same order as the second term, and the first term is negligible. This indicates that in order to reduce the uncertainty in the estimates of the rate of turbulent production, we particularly need to reduce the uncertainty in the Reynolds stress estimates, ${\sigma_R}^2$. Since this involves increasing the number of ensembles, M, used to calculate the variance, it is apparent that ${\sigma_S}^2$ will also be decreased by the same factor at times when turbulent fluctuations dominate over instrument noise. The instrument noise, $\rho\sigma_S\sigma_R$, shown by the open circles in Figure 6.7, has a minimum value of about 2.1×10^{-4} Wm^{-3} for mode 1 and about 3×10^{-5} Wm^{-3} for mode 12. Inserting the

values from the quarry noise tests into equations (3.26) and (3.30) give noise levels in TKE production rate $\rho\sigma_S\sigma_R$ of 1.6 x 10^{-4} Wm^{-3} and 4.8 x 10^{-5} Wm^{-3} for modes 1 and 12 respectively, consistent with the noise levels from the observations.

The estimates of the uncertainties in the Reynolds stress, shear and TKE production rate are summarised in Table 6.1. Comparing the estimate of each parameter using the quarry test results and the observational data show that there is agreement in each case to within a factor of 2 or better. These results indicate that the still water tests are a good indicator of the true uncertainties in Reynolds stress, shear and TKE production rate estimates.

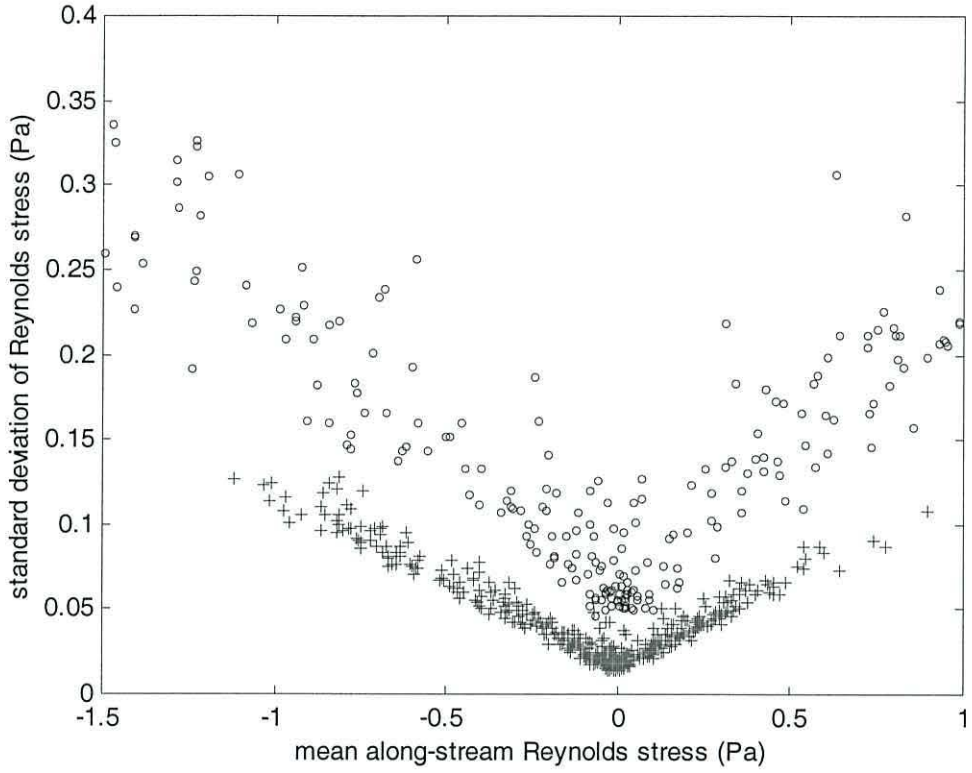

Figure 6.1: The calculated standard deviation of the Reynolds stress estimates in the main flow direction plotted against the mean value of the Reynolds stress for mode 1 (open circles) and mode 12 (crosses).

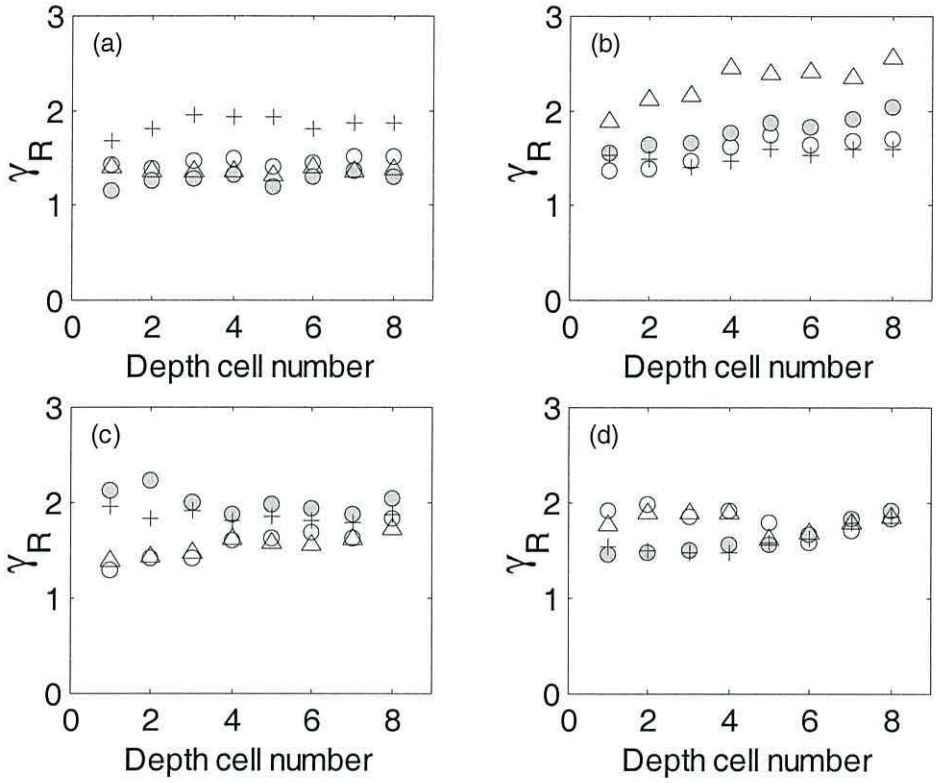

Figure 6.2: Correction factor γ_R for non-independence of b'^2 measurements in each beam for (a) mode 1 flood, (b) mode 1 ebb, (c) mode 12 flood and (d) mode 12 ebb. Each beam is plotted separately as open circles (beam 1), shaded circles (beam 2), triangles (beam 3) and crosses (beam 4). The mean values of the correlations are slightly higher when the velocity recorded is in the main flow direction, hence there is a difference between flood and ebb for some beams.

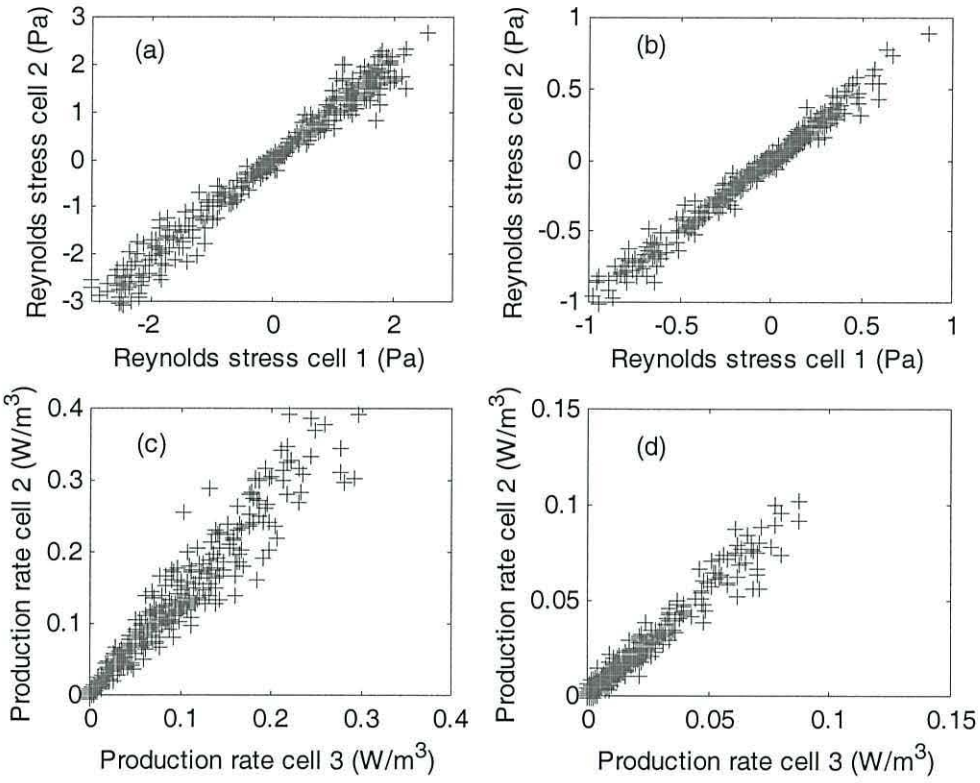

Figure 6.3: The relationship between both the Reynolds stress for (a) mode 1 and (b) mode 12, and the TKE production rate for (c) mode 1 and (d) mode 12, in adjacent depth cells.

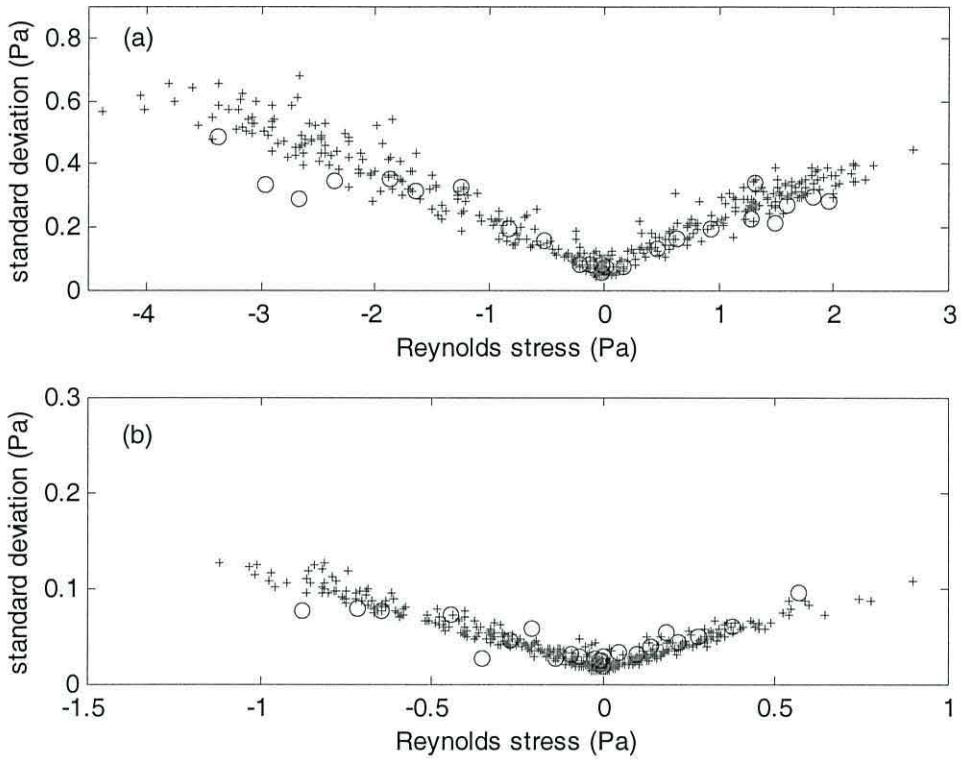

Figure 6.4: The standard deviation of the Reynolds stress estimates using the two methods are compared, for (a) mode 1 and (b) mode 12. In the 'empirical' method, shown by the open circles, the data were sorted into bins containing an equal number of data points according to the value of the Reynolds stress in an adjacent depth cell; the mean and standard deviations were then calculated.

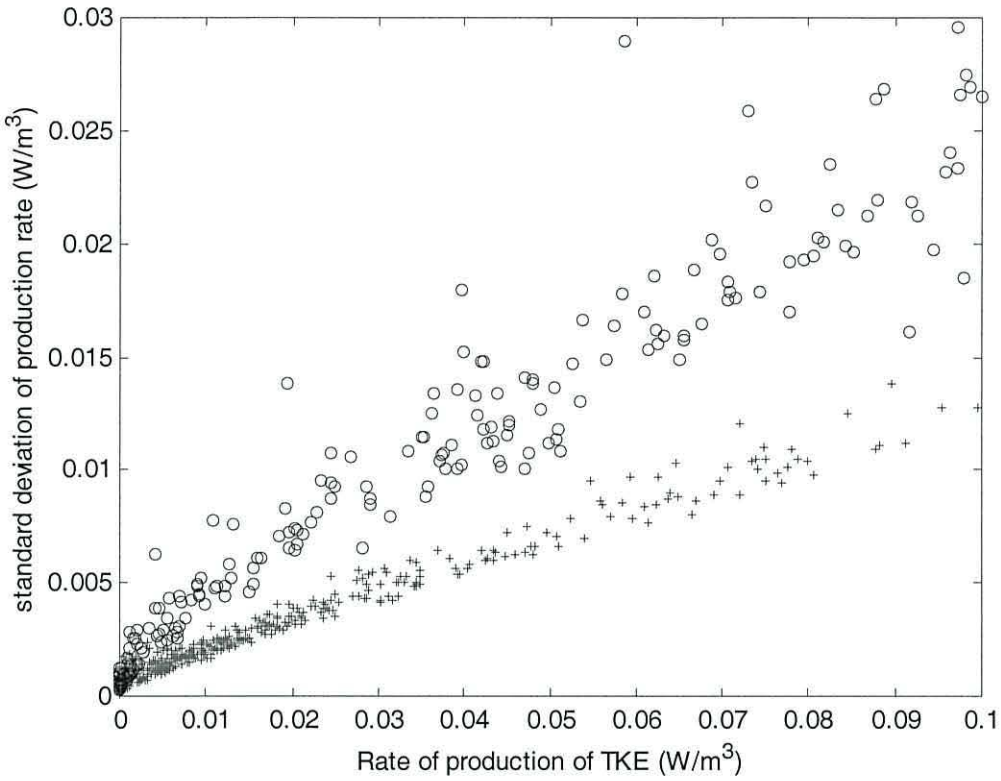

Figure 6.5: The calculated standard deviation of the TKE production rate estimates plotted against the mean value of the TKE production rate for mode 1 (open circles) and mode 12 (crosses).

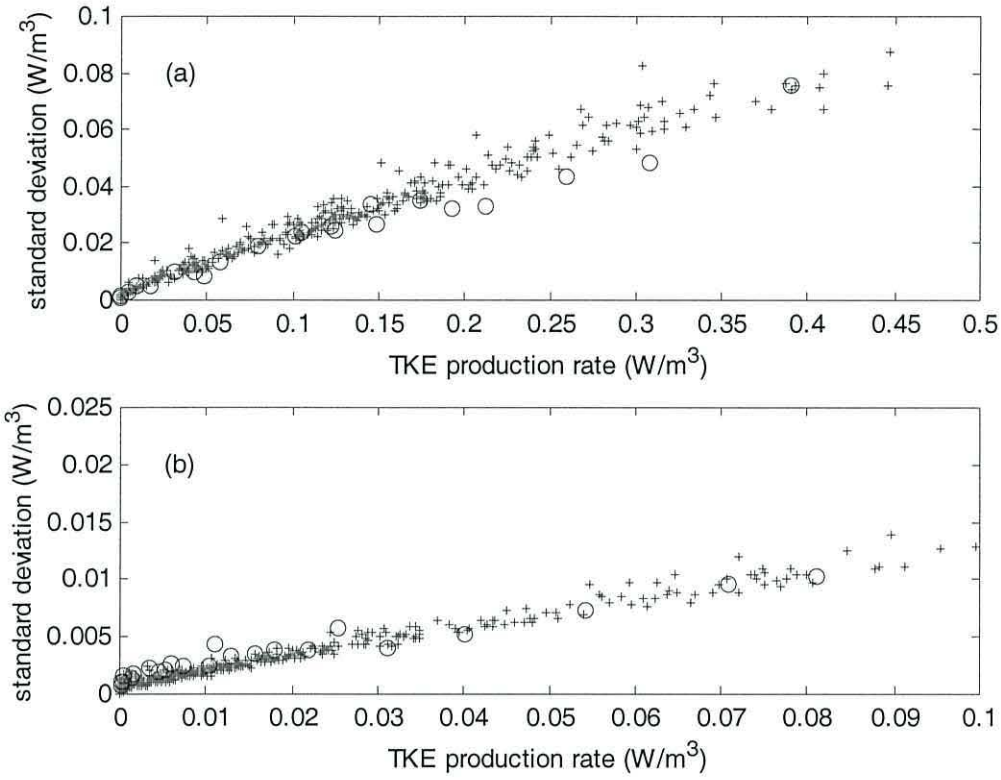

Figure 6.6: The standard deviations of the TKE production rate estimates using the two methods are compared, for (a) mode 1 and (b) mode 12. In the 'empirical' method, shown by the open circles, the data were sorted into bins containing an equal number of data points according to the value of the production rate in an adjacent depth cell; the mean and standard deviations were then calculated.

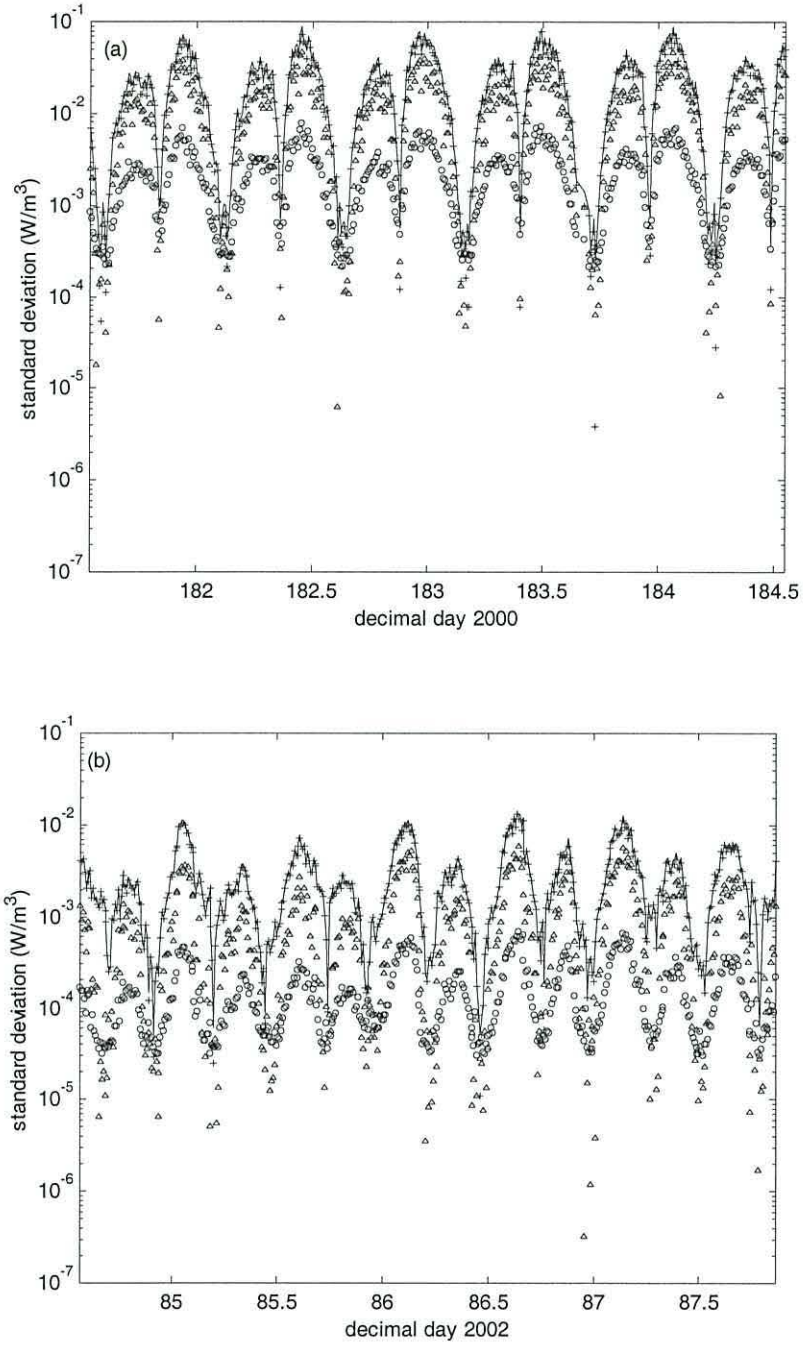

Figure 6.7: Time series of components of standard deviation of TKE production rate for (a) mode 1 and (b) mode 12. The three terms are: $\rho|\overline{u'w'}|\sigma_S$ (triangles), $\rho|\partial u/\partial z|\sigma_R$ (crosses), $\rho\sigma_S\sigma_R$ (open circles). The total standard deviation (the square root of the sum of the squares of the three terms) is also shown by a solid line. The highest values are for the term containing the variance of the Reynolds stress, except at slack water, when the noise term $(\rho\sigma_S\sigma_R)$ dominates.

Table 6.1: The estimated values of the standard deviations of the along-beam velocity (σ_N), the Reynolds stress (σ_R), the shear (σ_S), and the rate of production of TKE (σ_P) for mode 1 and mode 12. Each value has been estimated both from the observations and from the tests in a stationary water column (the quarry tests) using a 10-minute averaging period.

	Mode 1	Mode 12
σ_N (observations) (m s^{-1})	0.018	0.014
σ_N (test) (m s^{-1})	0.0217	0.0184
$\rho\sigma_R$ (observations) (Pa)	0.074	0.018
$\rho\sigma_R$ (test) (Pa)	0.0435	0.0219
σ_S (observations) (s^{-1})	4.19×10^{-3}	2.09×10^{-3}
σ_S (test) (s^{-1})	3.67×10^{-3}	2.20×10^{-3}
$\rho\sigma_P$ (observations) (W m^{-3})	2.12×10^{-4}	3.01×10^{-5}
$\rho\sigma_P$ (test) (Wm^{-3})	1.60×10^{-4}	4.81×10^{-5}

6.2 Improvements in measurements due to use of the fast-pinging mode

The analysis of the mode 1 and mode 12 data sets indicates that mode 12 at 10 Hz, recording ensemble averages at 1 Hz reduces the floor level for detection of Reynolds stress to about 0.04 Pa compared with about 0.14 Pa using mode 1 at 2 Hz recording ensemble averages at 0.5 Hz, if it is assumed that the detection limit is twice the standard deviation of the measurements at zero flow. At higher stresses, the uncertainty due to flow-related noise is reduced by using a higher number of ensembles for each estimate: for example for a stress estimated at 1 Pa, the uncertainty in mode 12 is about 12% compared with 22% in mode 1. There is a similar effect on the detection of lower levels of TKE production: the detection level in mode 12 is approximately 6×10^{-5} W m^{-3}, compared with 4×10^{-4} W m^{-3} in mode 1, an improvement by a factor of about six. At higher production rates there is a reduction in the uncertainty from over 19% to less than 13%. In both the TKE production rate and the Reynolds stress, the reduction in the uncertainty is due to a combination of an increase in the number of pings per ensemble and an increase in the number of ensembles used to calculate the Reynolds stress.

To illustrate the improvement in the quality of the data obtained using mode 12, Reynolds stress profiles at hourly intervals for a 12-hour period for each data set are shown in Figure 6.8. In (a) and (b) the 10-minute averaged along-channel profiles are shown for modes 1 and 12 respectively; in (c) and (d) the profiles have been averaged over an hour (6 profiles). In general, the stress profiles show the expected pattern of increasing magnitude towards the bed, and tending towards zero near the surface.

Error bars (±1 standard deviation) are indicated in each case for the two profiles at the extremes of the tidal cycle; these are the maximum uncertainties, since, except close to slack water, the uncertainty is mainly due to the element which is proportional to the stress. The small size of the error bars and the smoothness of the lines plotted in Figure 6.8 (d) for the hourly averaged mode 12 data indicate how accurately the Reynolds stresses can be measured using the currently available technology.

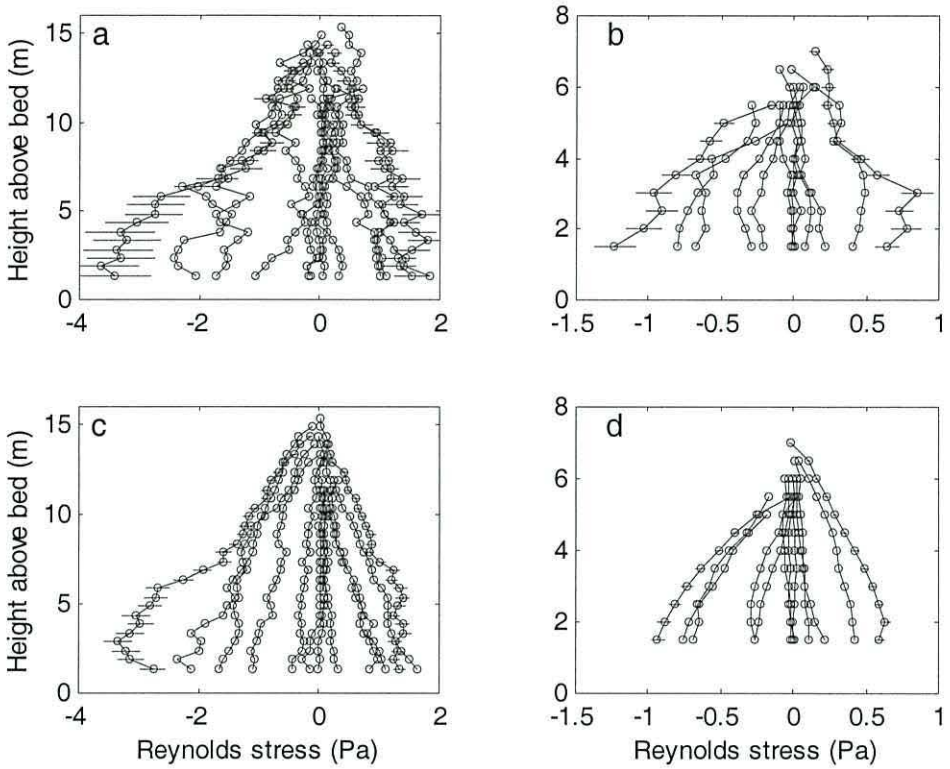

Figure 6.8: Profiles of Reynolds stress $-\rho\left(\overline{u'w'}\right)$ for a 12 hour period for each data set. The raw 10-minute profiles are plotted for (a) mode 1 and (b) mode 12. The stress at each level was then averaged over 1 hour (6 profiles), these are shown for (c) mode 1 and (d) mode 12. Error bars are shown in each case for maximum flood and maximum ebb profiles.

6.3 Turbulent time scales and optimal sampling rates

Strategies to reduce the uncertainties in the estimates of Reynolds stress, shear and TKE production rate can be devised if we have an estimate of the time scale of the turbulent motions. Some information regarding the time scales can be obtained from an analysis of the role of the factor γ (equation 3.20). As the interval between measurements, Δt, is reduced to the autocovariance time scale of the turbulence, further increases in the frequency of velocity measurements will do little to decrease the uncertainty in the stress estimates due to the associated increase in γ as adjacent measurements become increasingly covariant. The number of measurements M which can be used to calculate the stresses is also constrained by the stationarity period of the flow. The stationarity period gives a maximum value of $M = T/\Delta t$, which for T = 10 minutes and Δt = 1 second sets a limit of $M \approx 600$. At present, the highest possible frequency of recording of velocity measurements using mode 12 is 1 Hz. The technology therefore provides a constraint at present of a maximum value for $M = T$ (seconds), even in regimes in which the turbulent time scales are shorter than one second. Using the maximum possible value of M combined with the maximum number of pings in each ensemble will give the most accurate measurement of Reynolds stress for any given ADCP configuration.

If it were possible to record velocity measurements at a higher frequency, the best quality data would be obtained with an interval between measurements, Δt, which is equal to the autocovariance time scale of the turbulence. This would give the maximum possible value for M, considering the stationarity period, and would reduce the value of γ to 1, with a consequent decrease in the standard deviation of the Reynolds stress estimates. By using an interval of less than Δt between measurements we would expect an increase in γ which would offset any improvement in the uncertainties due to the increase in M.

The correction factors γ_R and γ_S which compensate for the non-independence of successive values of $b_i'^2$ and $\partial u/\partial z$ respectively, are similar for mode 1 and mode 12, and somewhat smaller than those observed by Stacey *et al.* (1999a), with a maximum value of less than three in each case, and a median value of about 1.6, except for the

near-bed values of γ_S in mode 12, which have a median value of more than two. The largest values of these factors are only found around slack water, particularly on the transition from ebb to flood when the accelerations are extremely high. The high values of γ occur during the short periods when the stationarity of the flow was in doubt according to the run test mentioned in section 4.2. The non-stationarity of the flow during these periods means that some of the fluctuating velocities which have been estimated contain an element of the mean flow, and the autocorrelation time scale can therefore be expected to be larger than that of the true fluctuations.

If the time scale of the turbulence were greater than 1 second, it might be expected that the correction factor γ for the 1-second averages used in mode 12 would be higher than that for the 2-second averages used in mode 1. If the time scale were shorter than 1 second, there would be no significant correlation between one measurement and the next using either 1 Hz or 0.5 Hz sampling frequencies. In the data sets from the York River estuary and the Menai Strait, the fact that there is a significant correlation is known, since both γ_R and γ_S are greater than 1. However, most values are relatively low, so the correlation between successive measurements can be assumed to be very weak, indicating that for the flow in the York River estuary, a near optimum sampling rate was used.

6.4 Effect of depth cell size on ADCP turbulence estimates

Near the boundary, as the length scale of the turbulent fluctuations decreases, some undersampling of the variance may result from the use of depth cells of the size used here. Previous studies show this effect to be small: Lu *et al.* (2000) estimate that using a depth cell size of 1 m produces an underestimate of the Reynolds stress of 5% compared with a depth cell size of 0.1 m, and Rippeth *et al.* (2002) estimate a loss of less than 5% when comparing depth cells of 0.5 m and 0.25 m. An additional, unfavourable effect of decreasing the depth cell size is to increase the instrument noise, which may have serious implications in a low energy regime.

When configuring an ADCP for turbulence measurements, the choice of depth cell size, Δz, represents an irreversible decision in relation to stress and TKE uncertainty. Stress recorded with an initial choice of Δz cannot be matched, in terms of statistical

reliability, by averaging data from two adjacent depth cells of size $\Delta z/2$. Since the standard deviation of velocity varies approximately as $1/\Delta z$:

$$\sigma_N(\Delta z/2) = 2\sigma_N(\Delta z)$$

where $\sigma_N(\Delta z)$ is the standard deviation of the along-beam velocities for a depth cell of size Δz. Averaging adjacent depth cells of size $\Delta z/2$ gives:

$$\sigma_N(2 \text{ x } \Delta z/2) = \sqrt{2}\sigma_N(\Delta z)$$

indicating a higher standard deviation of the velocity measurements if the smaller depth cell size is selected, even after averaging over two depth cells. This gives the ratio of the uncertainty in the Reynolds stress estimates due to instrument noise using the two values of Δz:

$$\frac{\sigma_R(2 \text{ x } \Delta z/2)}{\sigma_R(\Delta z)} = \frac{\sigma_N{}^2(2 \text{ x } \Delta z/2)}{\sigma_N{}^2(\Delta z)} = 2$$

since $\sigma_R \propto \sigma_N{}^2$ (equation 3.30). If the stresses are calculated first, then averaged over 2 depth cells of size $\Delta z/2$, then the ratio is even less favourable: $\left(2\sqrt{2}\right)$. In practice, in RDI's Workhorse ADCPs, σ_N does not vary exactly as $1/\Delta z$, but exhibits a discontinuous variation with depth cell size, which is documented in RDI's configuration software (*PlanADCP*).

6.5 Errors due to tilt in the ADCP

An analysis of the effect of tilt on the estimates of Reynolds stress was presented in chapter 3. The tilt for each of the deployments of the ADCPs is shown in Table 6.2. Pitch is positive when beam 3 is higher than beam 4; roll is positive when beam 2 is higher than beam 1. Also shown in the table is the heading for each deployment and the angle θ_H, which is the angle through which the x-axis (direction of beam 1) must be rotated in order to align with the along-stream direction of flow. The tilt analysis in chapter 3 shows that the effect of tilt on the Reynolds stress estimates is more severe when the tilt is in the plane of the main flow direction.

In the first deployment of the 1.2 MHz ADCP, beams 1 and 2 are approximately aligned with the flow direction (bearing 340°); the tilt angle in this plane is 1.5°, which is low enough for the errors induced by this tilt to be low: around 10-15%. The

tilt in the plane of beams 3 and 4 is higher, at 3°, but since these beams are almost aligned with the across-channel direction, the contribution to the error in the Reynolds stress estimate will be small. In the second 1.2 MHz deployment, both tilt angles are small, so these data are expected to be affected only slightly by the tilt errors. In the third 1.2 MHz deployment, the pitch angle of 2.5° may have a significant effect on the data, since beams 3 and 4 are aligned at an angle of only 37° to the main flow direction. Similarly in the case of the 600 kHz ADCP, in which both tilt angles were relatively large, with beams 1 and 2 approximately aligned with the mean flow direction.

The negative roll angle in the 600 kHz deployment means that the error should tend to decrease the contribution to τ on the flood, and increase it on the ebb, since the value of $\overline{b_2'^2} - \overline{b_1'^2}$ is negative on the flood. The pitch angle would tend to have the reverse effect, but makes a lesser contribution to the calculated along-stream stress, since beams 3 and 4 are aligned in a plane close to the along-channel direction. The stresses obtained from this deployment can be directly compared with those from the second 1.2 MHz deployment since there was an overlap of some 15 hours in the deployment periods. Tilt errors in the 1.2 MHz data are expected to be small due to the small tilt angles, but both pitch and roll would both tend to increase the measured value of τ on the flood and decrease it on the ebb. The comparison of these two data sets for the time at which data are available from both instruments is shown as a time series in Figure 6.9 for the lowest seven depth cells of the 600 kHz and the depth cells at the same height for the 1.2 MHz. The data points corresponding to the flood indicate that slightly higher values are obtained from the 1.2 MHz. On the ebb, similar maximum values are obtained from both instruments, but the peak value in the 600 kHz occurs earlier than that of the 1.2 MHz.

In the scatter plot (Figure 6.10), the same data from the two instruments are plotted against each other. On the flood, there is a definite tendency for the 1.2 MHz to produce higher values, while on the ebb, this trend is less clear. These results are consistent with the expected errors due to higher tilt in the 600 kHz.

Table 6.2: Tilt and heading angles for each ADCP deployment. The pitch is positive for beam 3 higher than beam 4; roll is positive for beam 2 higher than beam 1.

	Pitch	Roll	Heading	θ_H = 340° - heading - 90°
1.2 MHz (1)	3°	1.5°	079°	171°
1.2 MHz (2)	0.6°	-0.6°	290°	320° (-40°)
1.2 MHz (3)	2.5°	-1°	303°	307° (-53°)
600 kHz	-2.5°	-2.7°	077°	173°

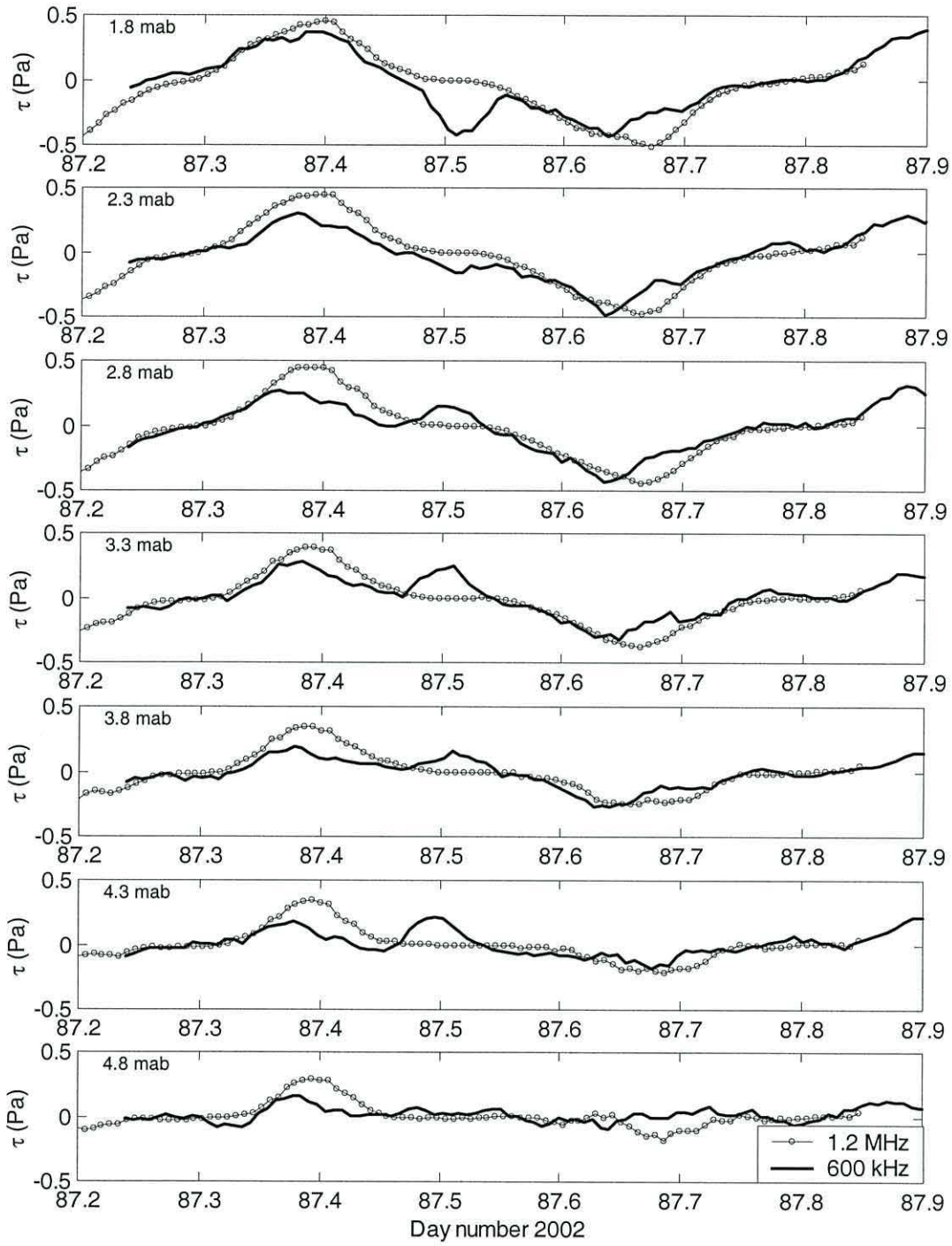

Figure 6.9: Time series of along-stream Reynolds stress τ at 7 different heights above the bed for the deployments of the two ADCPs for the period when data were obtained from both

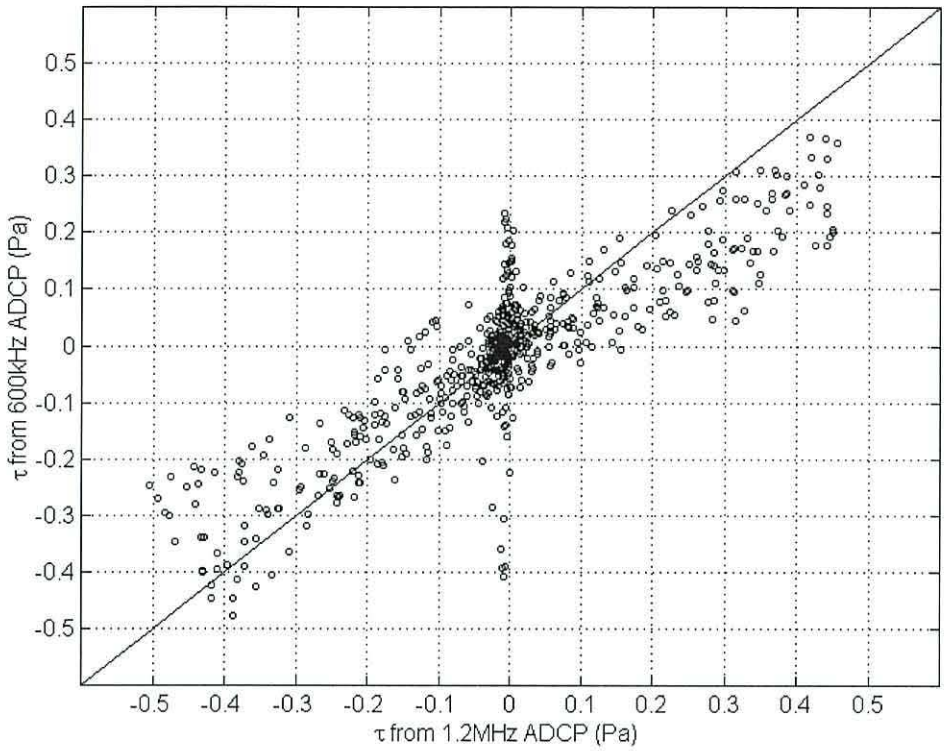

Figure 6.10: Scatter plot of Reynolds stress $\tau = -\rho\overline{u'w'}$ estimated from the 600 kHz and 1.2 MHz ADCPs for the period during which simultaneous data were obtained.

6.6 Errors due to waves

In section 3.4.6, it was estimated that the error in the Reynolds stress estimates in the presence of surface waves was of order 10^{-3} m^2 s^{-2} for small tilt angles. This is an order of magnitude greater than the peak stress at neaps and the same order as the peak stress at springs. There is therefore a significant error in the Reynolds stress estimates if any surface waves are present. The absence of any accurate wave data leaves only the along-beam velocity variances and the wind data as predictors of when these errors are likely to be significant. The analysis of the cycle of TKE in chapter 4 indicates the periods when the Reynolds stress and TKE production rate estimates might be compromised due to the presence of surface waves.

6.7 Summary

The uncertainties in the ADCP data from the York River have been analysed, indicating that using the technology currently available, Reynolds stresses of 0.04 Pa and TKE production rates of 5×10^{-5} W m^{-3} can be detected. The results from the York River are compared with those from a body of still water, and with the noise values supplied by RDI, using their *PlanADCP* software; all estimates are found to be consistent.

The errors due to tilt are examined using the data from two ADCPs which were deployed simultaneously. Whilst absolute errors cannot be determined, the results from the two ADCPs are consistent with those expected from the theoretical analysis of chapter 3.

CHAPTER 7

Summary and Discussion

The cycle of turbulence and stratification was analysed for the York River Estuary, a partially stratified estuary. Recent improvements in acoustic Doppler technology were exploited to obtain high quality measurements of turbulent parameters. The uncertainties in these quantities were calculated using a rigorous statistical analysis, the results of which were corroborated by calculating the uncertainties in a subset of the data using a nonparametric bootstrap method; the two methods were found to be in close agreement.

In the York River, a partially stratified estuary, the observed Reynolds stress and TKE production rate are suppressed by stratification. The eddy viscosity is similarly affected by stratification, but is further suppressed during the ebb by the effects of tidal straining, whilst tending to exhibit the characteristics of a mixed water column on the flood. The dynamical balance obtained for the York River is incomplete, particularly at peak ebb. The drag coefficient was estimated using a quadratic drag law, and was observed to increase at higher flow speeds.

7.1 Measurements of turbulence using the ADCP variance method

The accuracy of the application of the variance method to turbulence measurements using ADCPs has improved a great deal in recent years following advances in instrumentation. The analysis presented in Chapter 6 indicates that ADCP measurements are now able to detect Reynolds stresses as low as 0.04 Pa and TKE production rates of order 10^{-5} W m^{-3} (using RDI's mode 12), compared with the previous generation of instruments and firmware in which the limits of detection were approximately 0.14 Pa and order 10^{-4} W m^{-3} respectively (using RDI's mode 1). It is now also possible to measure the eddy viscosity through most of the water column and most of the tidal cycle. Previously, this could only be done with any degree of accuracy during peak flow periods (Rippeth *et al.*, 2002).

The correction factor γ, which compensates for the non-independence of successive measurements of the velocity fluctuations and shear, although greater than one, is low for most of the observation period. This indicates that in the York River observations

a near-optimum sampling frequency in terms of the turbulent time scales has been achieved by recording velocities at 1Hz.

The depth cell size chosen for this study was based on a compromise between spatial resolution and the expected magnitude of the uncertainties in the Reynolds stress and TKE production rate estimates. The analysis of the uncertainties in these estimates indicates that the choice of 0.5 m depth cells was appropriate for observation of the entire spring-neap cycle in the York River estuary. The main deficiency in these results is in the estimates of the turbulent parameters near the bed: the velocity measurements calculated internally by the ADCP are a weighted average over a vertical distance which is twice the nominal depth cell size. This causes a smoothing of the velocity measurements in a region in which the shear is high. Additionally, when taking into account the blanking interval used by the instrument and the height of the transducers above the bed, the lowest depth cell in the York River estuary deployments is centred at over 1m from the bed. Recent advances in instrumentation, which were not available at the time of these observations, may have partially solved the latter problem for future deployments, since an ADCP is now available in which the blanking interval can be set to zero. The spatial resolution could also be improved by using a smaller depth cell size; this would only be appropriate in a regime in which the currents are comparable to or stronger than those observed in the York River estuary at springs, since the flow-related uncertainty dominates during stronger flows.

7.2 Results from the York River estuary observations

7.2.1 Summary of the interaction of turbulence and stratification

Analysis of the evolution of turbulence over a spring-neap cycle was made using the variance method which uses the along-beam velocities from a fast-sampling ADCP to estimate the Reynolds stress, TKE production rate and eddy viscosity. The results were then examined in relation to the action of tidal straining. Throughout the spring-neap cycle in the York River estuary, faster-flowing currents are observed on the ebb. In a fully mixed water column, these might be expected to produce higher Reynolds stresses, rates of TKE production and eddy viscosity than on the flood when the flow is weaker.

At neaps, the water column is stratified at all times. The level of stratification is reduced somewhat during the flood, particularly when the tidal currents are relatively strong, but increases during the ebb. The characteristics of the turbulence at this time are quite different from those of a vertically mixed water column. The stress, production rate and eddy viscosity are all suppressed during the periods of strongest stratification; the highest values of all three parameters were observed during the stronger flood, when the stratification was at its weakest. The times of maximum stress and TKE production rate at this time coincided approximately with the time of peak flow speed, whilst there was a delay in the maximum eddy viscosity until the stratification reached a minimum, when the flow was already decelerating. The stresses were lower on the ebb than on the flood by a factor of about four, despite the stronger currents, since the stratification allows the layers of water of different density to glide smoothly over each other, with low frictional stresses between them, thus producing high shear values combined with low Reynolds stresses. The TKE production rate and eddy viscosity, which are both dependent on τ, were therefore also lower on the ebb: P by about an order of magnitude and N_z diminished to a level which could barely be discerned above noise as the stratification suppressed the turbulent motions.

At springs, the water column remained very weakly stratified for most of the tidal cycle, with slightly stronger stratification around slack water, particularly at the end of the ebb. The tidal currents during this part of the spring-neap cycle were significantly stronger on the ebb than on the flood. The highest values of Reynolds stress, TKE production rate and eddy viscosity persisted for longer on the ebb, reflecting the flood-ebb asymmetry, both in terms of the flow speeds and the fact that the ebb phase of the tidal cycle in the York River estuary lasts for longer than the flood. The highest stress and TKE production rates were also observed during the ebb, while the highest eddy viscosity occured during the flood, when the shear was low and the water column relatively well-mixed. This result is consistent with those of Geyer *et al.* (2000), who found that the tidally averaged eddy viscosity in the Hudson River was about twice as large during floods as during ebbs. The flood-ebb asymmetry in the eddy viscosity is a reflection of the tidal straining mechanism, in which the constant stratifying influence of the horizontal density gradient confines the turbulent activity to the lower part of the water column during the ebb, while on the flood, the addition

of tidal straining effects to a very weakly stratified water column allow the turbulent motions to exhibit behaviour similar to that of a vertically mixed water column.

7.2.2 The discrepancies in the York River dynamical balance

In chapter 5, the dynamical balance for the York River Estuary was examined, and the bottom stress term from the ADCP was observed to be higher by a factor of up to three during the ebb. This contrasts with the results of a test of the dynamical balance in the Hudson River (Trowbridge *et al.*, 1999), in which benthic acoustic stress sensors (BASS) were used to estimate the bottom stress. They found that the bottom stress was consistently lower than the sum of the pressure gradient and acceleration terms by a factor of up to two.

Trowbridge *et al.*, (1999) suggest several reasons for the failure of the momentum terms to balance: local estimates of the Reynolds stress at the bed may not be representative of the bottom stress on a scale of kilometres, a substantial part of the momentum transfer may be due to form drag, or the neglected advective terms $u\,\partial u/\partial x$, $v\,\partial u/\partial y$ and $w\,\partial u/\partial z$ may be significant.

Recent work using models (Lerczak and Geyer, 2004) indicate that the advective terms $v\,\partial u/\partial y$ and $w\,\partial u/\partial z$ may be important in stratified estuaries due to transverse circulation effects. In order to estimate the advective terms $u\,\partial u/\partial x$ and $v\,\partial u/\partial y$ with an adequate degree of accuracy, it would be necessary to deploy an array of five ADCPs along and across the estuary, in order to calculate the gradient of u in both directions and measure u and v at a central point. An accurate measurement of $w\,\partial u/\partial z$ is even more difficult to achieve. The ADCPs deployed in this study provide an estimate of the shear in the along-channel velocity within the limits of accuracy outlined in chapter 3. They also provide a crude estimate of the vertical velocity w, given by:

$$w = \frac{-\left(\overline{b}_1 + \overline{b}_2 + \overline{b}_3 + \overline{b}_4\right)}{4\cos\theta} \tag{7.1}$$

However, this estimate is compromised by any tilt in the ADCP. The error in the vertical velocity due to tilt is given by (Lu and Lueck, 1999a): $\psi_{34}(\overline{b}_4 - \overline{b}_3) - \psi_{12}(\overline{b}_2 - \overline{b}_1)$, where ψ_{34} = pitch and ψ_{12} = roll and $\overline{b}_i$ is the mean along-beam velocity for beam i. Even tilt angles as low as those obtained during the springs ADCP deployment (0.6° and –0.6° respectively), result in tilt errors of order 0.01 m s^{-1}, the same order as the estimates of w using equation (7.1). A further problem occurs due to the difficulty in establishing the true pitch and roll angles relative to the direction of the normal to the mean flow, since the tilt angles are relative to the direction of the local gravitational force which may deviate from the normal to the mean flow direction.

The results of the Lerczak and Geyer (2004) model indicate that the effect of the transverse circulation is stronger during the flood than during the ebb by a factor of about four, while the results from the York River show the greatest discrepancy in the dynamical balance during the ebb. If the discrepancy in the dynamical balance for the York River is in fact due to transverse circulation effects, a possible explanation for this apparent conflict with the results from the model could be due to the different cross-sectional shapes of the channels: the York River Estuary has a deep channel near the bank to the north east, bordered by shallower regions, whilst the channel cross section used in the model has much steeper bed slopes towards the banks.

7.2.3 Evidence of a tidally varying drag coefficient

In the York River, analysis of the drag coefficient shows that it appears to vary with the flow speed. This contradicts the generally accepted assumption that the bottom drag coefficient is constant for a given region, depending only on the bed roughness (Soulsby, 1983). However, a surface drag coefficient which varies with wind speed is generally accepted in the case of wind blowing over water bodies (e.g. Smith, 1980; Large and Pond, 1981). This is an area in which more research needs to be done in order to establish what mechanisms are driving the flow-related drag coefficient and whether a similar phenomenon also occurs in other regions.

7.2.4 Improved parameterizations of eddy viscosity

Parameterizations of eddy viscosity using a gradient Richardson number were found to be inadequate in the York River Estuary due to the presence of tidal straining effects. These simple inverse power law relationships are inadequate in the present case, since they fail to take into account buoyancy effects in which stratification or inverse density gradients are instantaneously destroyed by mixing and convection, but are nevertheless part of the physical process. It is conjectured that a better result might be obtained by including in the parameterizations a horizontal Richardson number, which is effectively a parameter representing tidal straining. This might be similar in form of that proposed by Stacey et al. (2001) (see equation (5.6)), but modified to include the flow direction, so that it would be positive or negative depending on whether the tidal straining mechanism is contributing to stratification or to mixing (or convection).

7.2.5 Measurements of turbulence in the presence of wind and waves

The effects of wind and the resulting wave action on the along-beam variances measured by the ADCP indicate that measurements of turbulent parameters in the presence of waves are severely compromised. The particularly large effects seen in the estimates of the TKE are somewhat diminished in the Reynolds stress and TKE production rate estimates due to the subtraction of the variance along two opposite beams where the wave effects are largely cancelled out since the time average of the wave effects in each beam is the same. However, even a small tilt in the ADCP introduces an error due to waves, since the time averaged wave fluctuations can no longer be assumed to be the same in opposite beams.

In order to overcome this problem, the first strategy which should be employed is to ensure that the ADCP is mounted in such a way that the tilt is negligible. Gimballed mountings for ADCPs are now available, and this technology should ensure that the ADCP is mounted so that the nominal vertical is the true local gravitational direction. This will not, of course, completely overcome the errors due to tilt should the direction of the local gravitational acceleration deviate significantly from the normal to the mean flow direction.

In future observations, the collection of wave data such as wave height along with the turbulence measurements could make possible the separation of velocity fluctuations generated by wave action from those generated by tidally induced turbulence. Methods are available to estimate the wavelength and direction of the waves from the along-beam velocities of the ADCP (Howarth, 1999), but accurate estimates of wave-induced errors also require information regarding the amplitude of the waves.

7.3 Conclusions

It has been demonstrated that the ADCP variance method can be used to measure Reynolds stresses greater than about 0.04 Pa and TKE production rates of order 10^{-5} W m^{-3} and higher. It is also possible to estimate eddy viscosity throughout the water column and obtain upper and lower bounds for the TKE. Care should be taken when deploying an ADCP for turbulence measurements that the tilt in the instrument is minimised, since even a small tilt can severely compromise the quality of the measurements, particularly if surface waves are present. Errors due to surface waves could be better quantified in future observations if some wave data, such as wave height are recorded.

The current technology allows measurement of velocity fluctuations at 1Hz, which is close to the autocorrelation time scale of the turbulent motions at the observation site used in this study. Improvements in future measurements are therefore likely to be associated with technological advances which allow higher spatial resolution of velocity measurements with low uncertainties rather than a further increase in ping rates.

The accuracy of the ADCP estimates of Reynolds stress, TKE production rate and eddy viscosity in the partially stratified York River estuary enabled a detailed analysis of the cycle of each of these parameters to be made. These results indicate that stratification suppresses all three parameters, and that tidal straining further lowers the eddy viscosity on the ebb and enhances it on the flood.

The data set analysed here suggests that the bottom stress does not conform to a quadratic drag law which is universal for all flow speeds, and a flow-related

component is required to accurately predict the bottom stress from the mean flow velocity. The understanding of this phenomenon could be improved by measurement of the Reynolds stress closer to the bed, since the bed stress in the York River was estimated from the stress in a depth cell centred at over a metre above the bed.

The momentum balance in the York River estuary is incomplete, particularly at peak ebb, possibly due to transverse circulation effects, the estimation of which requires further measurements of the velocity gradients along and across the estuary as well as accurate estimates of the vertical velocity. It is also possible that the non-uniformity of the channel between the tide gauges or the effects of form drag are responsible for the failure of the momentum terms to balance exactly. The results of the dynamical balance analysis, despite the discrepancies, are nevertheless encouraging; a future observational campaign might use an array of ADCPs, which could be used to accurately estimate the effects of the transverse circulation, thus removing one of the possible sources of the failure of the momentum terms to balance.

References

Bakker, D.C.E., H.J.W. deBaar and H.P.J. deWilde (1996) Dissolved carbon dioxide in Dutch coastal waters, *Marine Chemistry*, **55**, 247-263

Beardsley, R.C., R. Limeburner, H. Yu and G.A. Cannon (1985) Discharge of the Changjiang into the East China Sea, *Continental Shelf Research*, **4**, 57-76

Bendat, J.B. and A.G. Piersol, 1971: *Random Data: Analysis and Measurement Procedures*, John Wiley, New York, 407pp.

Bertuccioli, L., G.I. Roth, J. Katz and T.R. Osborn (1999) A submersible particle image velocimetry system for turbulence measurements in the bottom boundary layer, *Journal of Atmospheric and Oceanic Technology*, **16**, 1635-1646

Borges, A.V. and M. Frankignoulle (2003) Distribution of surface carbon dioxide and air-sea exchange in the English Channel and adjacent areas, *Journal of Geophysical Research – Oceans*, **108** (C5), art.no. 3140

Bowden, K.F. (1977) Turbulent processes in estuaries, in *Estuaries, Geophysics and the Environment*, National Academy of Sciences, Washington, D.C., pp.46-56

Bowden, K.F. (1983*) The Physical Oceanography of Coastal Waters*, Ellis Horwood Ltd., W. Sussex, 302pp.

Bowden, K.F. and L.A. Fairbairn (1952) Further observations of the turbulent fluctuations in a tidal current, *Philosophical Transactions of the Royal Society A*, **244**, 335-356

Bowden, K.F. and M.R.Howe (1963) Observations of turbulence in a tidal current, *Journal of Fluid Mechanics,* **17**, 271-284

Bowden, K.F. and P. Hamilton (1975) Some experiments with a numerical model of circulation and mixing in a tidal estuary, *Estuarine and Coastal Marine Science*, **3**, 281-301

Burgett, R.L., D. Hebert and N.S. Oakey (2001) The vertical structure of turbulence on the Southern Flank of Georges Bank, *Journal of Geophysical Research*, **106**, 22545-22558

Cai, W.J., Z.H.A. Wang and Y.C. Wang (2003) The role of marsh-dominated heterotrophic continental margins in transport of CO2 between the atmosphere, the land-sea interface and the ocean, *Geophysical Research Letters*, **30**(16), art.no. 1849

Cameron, W.M. and D.W. Pritchard (1963) Estuaries, in The Sea vol.2, M.N. Hill (ed.), Wiley, New York, Section III, pp. 306-324

Dewey, R.K. and W.R. Crawford (1988) Bottom Stress Estimates from Vertical Dissipation Rate Profiles on the Continental Shelf, *Journal of Physical Oceanography*, **18**, 1167-1177

Dewey, R.K., W.R. Crawford, A.E. Gargett and N.S. Oakey (1987) A microstructure instrument for profiling oceanic turbulence in coastal bottom boundary layers, *Journal of Atmospheric and Oceanic Technology*, **4**, 288-297

Doron, P., L. Bertuccioli, J.Katz and T.R. Osborn (2001) Turbulence Characteristics and Dissipation Estimates in the Coastal Ocean Bottom Boundary Layer from PIV Data, *Journal of Physical Oceanography*, **31**, 2108-2134

Dyer, K.R. (1997) *Estuaries*, John Wiley, England, 195pp.

Eriksen, C.C. (1978) Measurements and models of fine structure, internal gravity waves and wave breaking in the deep ocean, *Journal of Geophysical Research*, **83**, 2989-3009

Fisher, N.R. (2003) The cycle of turbulent kinetic energy dissipation and mixing in Regions of Freshwater Influence, Ph.D. Thesis, University of Wales, Bangor 141pp.

Frankignoulle, M. and A.V. Borges (2001) European continental shelf as a significant sink for atmospheric carbon dioxide, *Global Biogeochemical Cycles*, 15, 569-576

Gargett, A.E. (1994) Observing turbulence with a modified acoustic Doppler current profiler, *Journal of Atmospheric and Oceanic Technology*, **11**, 1592-1610

Gargett, A.E. (1999) Velcro measurement of turbulence kinetic energy dissipation rate ε, *Journal of Atmospheric and Oceanic Technology*, **16**, 1973-1993

Gargett, A.E. and T.R. Osborn (1981) Small-scale shear measurements during the fine and microstructure experiment (FAME), *Journal of Geophysical Research*, **86**, 1929-1944

George, R. and H.J. Hussein (1991) Locally axisymmetric turbulence, *Journal of Fluid Mechanics*, **233**, 1-23

Geyer, W.R., J.H. Trowbridge and M.M. Bowen (2000) The dynamics of a partially mixed estuary, *Journal of Physical Oceanography*, **30**, 2035-2048

Goodman, L.A. (1960) On the exact variance of products, *Journal of the American Statistical Association*, **55**, 708-713

Grant, W.D. and O.S. Madsen (1986) The continental shelf bottom boundary layer, *Annual Review of Fluid Mechanics*, **18**, 265-305

Grant, H.L., R.W. Stewart and A. Moilliet (1962) Turbulence spectra from a tidal channel, *Journal of Fluid Mechanics*, **12**, 241-263

Haas, L.W. (1977) The effect of the Spring-neap Tidal Cycle on the Vertical Salinity Structure of the James, York and Rappahannock Rivers, Virginia, U.S.A., *Estuarine and Coastal Marine Science*, **5**, 485-496

Hansen, D.V. and M. Rattray Jr., (1965) Gravitational circulation in straits and estuaries, *Journal of Marine Research*, **23**, 104-122

Heathershaw, A.D. (1976) Measurements of Turbulence in the Irish Sea Benthic Boundary Layer, *The Benthic Boundary Layer*, I.N. McCave (ed.), Plenium Publishing Corporation, New York, pp 11-31

Heathershaw, A.D. and J.H. Simpson (1978) The sampling variability of the Reynolds stress and its relation to boundary shear stress and drag coefficient measurements, *Estuarine and Coastal Marine Science*, **6**, 263-274

Hinze, J.O. (1959) *Turbulence*, McGraw-Hill, London, 586 pp.

Howarth, M.J. (1999) Wave measurements with an ADCP, *Proceedings of the IEEE Sixth Working Conference on Current Measurement, San Diego,* 41-44

Jay, D.A. (1991) Measurements and modelling of the spatial structure of nonlinear flow around a headland, in Tidal Hydrodynamics, B.B. Parker (ed.), John Wiley, pp. 403-418

Kay D.J. and D.A. Jay (2003) Interfacial mixing in a highly stratified estuary - 1. Characteristics of mixing, *Journal Of Geophysical Research-Oceans*, **108** (C3), art. no. 3072

Kolmogorov, A.N. (1941) The local structure of turbulence in incompressible fluid for very large Reynolds numbers, *Comptes rendus (Doklady) de l'Academie des Sciences de l'URSS*, **30**, 301-305, Reprinted in Friedlander S.K. and L. Tapper (eds.) *Turbulence: Classic Papers on Statistical Theory*, Interscience (1961), New York, pp.151-155

Koseff, J.R., J.K. Holen, S.G. Monismith and J.E. Cloern (1993) The effects of vertical mixing and benthic grazing on phytoplankton populations in shallow turbid estuaries, *Journal of Marine Research*, **51**, 1-26

Kundu, P.K. (1990) *Fluid Mechanics*, Academic Press, California, 638pp.

Large, W.G. and S. Pond (1981) Open ocean momentum flux measurements in moderate to strong winds, *Journal of Physical Oceanography*, **11**, 324-336

Lerczak, J.A. and W.R. Geyer (2004) Modeling the lateral circulation in straight, stratified estuaries, *Journal of Physical Oceanography*, (in press)

Lhermitte, R. (1968) Turbulent air motion as observed by Doppler radar, *Proceedings of the 13th Weather Radar Conference*, American Meteorological Society, Boston, 498-503

Lhermitte, R. (1983) Doppler sonar observation of tidal flow, *Journal of Geophysical Research*, **88**, 725-742

Lohrmann, A., B. Hackett and L.P. Røed (1990) High resolution measurements of turbulence, velocity and stress using a pulse-to-pulse coherent sonar, *Journal of Atmospheric and Oceanic Technology*, **7**, 19-37

Long, R.R. (2003) Do Tidal-Channel Turbulence Measurements Support $k^{-5/3}$?, *Environmental Fluid Mechanics*, **3**, 109-207

Lu, Y. and R.G. Lueck (1999a) Using a broadband ADCP in a tidal channel, Part I: Mean flow and shear, *Journal of Atmospheric and Oceanic Technology*, **16**, 1556-1567

Lu, Y. and R.G. Lueck (1999b) Using a broadband ADCP in a tidal channel, Part II: Turbulence, *Journal of Atmospheric and Oceanic Technology*, **16**, 1568-1579

Lu, Y., R.G. Lueck and D. Huang (2000) Turbulence characteristics in a tidal channel, *Journal of Physical Oceanography*, **30**, 855-867

Lueck, R.G., W.R. Crawford and T.R. Osborn (1983) Turbulent dissipation over the continental slope off Vancouver Island, *Journal of Physical Oceanography*, **13**, 1809-1818

Miles, J.W. (1961) On the stability of heterogeneous shear flows, *Journal of Fluid Mechanics*, **10**, 496-508

Monismith, S.G., J.R. Burau and M.T. Stacey (1996) Stratification dynamics and gravitational circulation in northern San Francisco Bay, in *San Francisco Bay: The Ecosystem*, J.T. Hollibaugh (ed.), American Association for the Advancement of Science, San Francisco,

Mood, A.M., F.A. Graybill and D.C. Boes (1974) Introduction to the theory of statistics, 3rd edition, McGraw Hill, New York, 564pp.

Moore, C.M., D. Suggett, P.M. Holligan, J. Sharples, E.R. Abraham, M.I. Lucas, T.P.Rippeth, N.R. Fisher, J.H. Simpson and D.J. Hydes (2003) Physical controls on phytoplankton physiology and production at a shelf sea front: a fast repetition-rate fluorometer based field study, *Marine Ecology Progress Series*, **259**, 29-45

Munk, W.H. and E.R. Anderson (1948) Notes on a theory of the thermocline, *Journal of Marine Research*, **7**, 276-295

Munk, W.H. and C.Wunsch (1998) Abyssal recipes II, energetics of tidal and wind mixing, *Deep Sea Research I*, **45**, 1977-2010

Nezu, I. and H. Nakagawa (1993) *Turbulence in Open Channel Flows*, A.A. Balkema, Brookfield, Vt., 281 pp.

Ozmidov, R.V. (1965) On the turbulent exchange in a stably stratified flow, Atmospheric and Oceanic Physics, **1**, 853-860 (English edition translated by the Americal Geophysical Union, pages 493-497)

Pacanowski, R.C. and S.G.H. Philander (1981) Parameterization of vertical mixing in numerical models of tropical oceans, *Journal of Physical Oceanography*, **11**, 1443-1451

Peters, H. (1997) Observations of stratified turbulent mixing in an estuary: Neap-to-spring variations during high river flow, *Estuarine, Coastal and Shelf Science*, **45**, 69-88

Peters, H., and R. Bokhorst (2001) Microstructure observations of turbulent mixing in a partially mixed estuary. Part II: Salt flux and stress, *Journal of Physical Oceanography,* **31**, 1105-1119

Phillips, O.M. (1966) *The Dynamics of the Upper Ocean*, Cambridge University Press, 261pp.

Pritchard, D.W. (1967) Observations of Circulation in Coastal Plain Estuaries, in *Estuaries*, G.H. Lauff (ed.), American Association for the Advancement of Science, Washington D.C., 37-44

Pugh, D.T. (1987) *Tides, Surges and Mean Sea-Level*, John Wiley, England, 472pp.

Raudkivi, A.J. and R.A. Callander (1975) *Advanced Fluid Mechanics*, Edward Arnold, London, 325pp.

R.D. Instruments (1996) *Acoustic Doppler Current Profiler Principles of Operation: A Practical Primer*, second edition for Broadband ADCPs, RDI, San Diego, California, 54pp.

R.D. Instruments (2002) Application note FSA014 (March 2002): High Resolution Water Profiling Water Mode 12, RDI, San Diego, California, 6pp.

Rippeth, T.P., N.R. Fisher and J.H. Simpson (2001) The Cycle of Turbulent Dissipation in the Presence of Tidal Straining, *Journal of Physical Oceanography*, **31**, 2458-2471

Rippeth, T.P., E.Williams and J.H. Simpson (2002) Reynolds Stress and Turbulent Kinetic Energy Production in a Tidal Channel, *Journal of Physical Oceanography*, **32**, 1242-1251

Rippeth, T.P., J.H. Simpson, E.Williams and M.E. Inall (2003) Measurement of the rates of production and dissipation of Turbulent Kinetic Energy in an energetic tidal flow: Red Wharf Bay revisited, *Journal of Physical Oceanography*, **33**, 1889-1901

Rottger, J. and M.F. Larsen (1990) UHF/VHF Radar Techniques for Atmospheric Research and Wind Profiler Applications, *Radar in Meteorology,* David Atlas, Ed., American Meteorology Society, 235-281

Scotti, R.S. and G.M. Corcos (1972) An experiment on the stability of small disturbances in a stratified free shear layer, *Journal of Fluid Mechanics*, **52**, 499-528

Scully, M.E. and C.T. Friedrichs (2003) The influence of asymmetries in overlying stratification on near-bed turbulence and sediment suspension in a partially mixed estuary, *Ocean Dynamics*, **53**, 208-219

Sharples, J., J.H. Simpson and J. Brubaker (1994) Observations and Modelling of Periodic Stratification in the Upper York River Estuary, Virginia, *Estuarine, Coastal and Shelf Science*, **38**, 301-312

Sharples, J., C.M. Moore, T.P. Rippeth, P.M. Holligan, D.J. Hydes, N.R. Fisher and J.H. Simpson (2001) Phytoplankton distribution and survival in the thermocline, *Limnology and Oceanography*, **43**, 486-496

Simpson, J.H. (1997) Tidal Processes in Shelf Seas, *The Sea*, Vol. 10, *The Global Coastal Ocean: Processes and Methods*, K.H. Brink and A.R. Robinson (eds.), Wiley, New York, Chapter 5, pp.113-150

Simpson, J.H. (1998) The Celtic Seas, Coastal Segment (19,E), *The Sea*, Vol. 11, A.R. Robinson and K.H. Brink (eds.), Wiley, New York, Chapter 23, pp.659-698
Simpson, J.H. and J.R. Hunter (1974) Fronts in the Irish Sea, *Nature*, **250**, 404-406

Simpson, J.H. and D. Bowers (1981) Models of stratification and frontal movement in shelf seas, *Deep-Sea Research*, **28**, 727-738

Simpson, J.H. and J. R. Hunter (1974) Fronts in the Irish Sea, *Nature*, **250**, 404-406

Simpson, J.H. and A.J. Souza (1995) Semi-diurnal switching of stratification in the Rhine ROFI, *Journal of Geophysical Research*, **100**, 7037-7044

Simpson, J.H., C.M. Allen and N.C.G. Morris (1978) Fronts on the Continental Shelf, *Journal of Geophysical Research*, **83**, 4607-4614

Simpson, J.H., J. Brown, J.P. Matthews and G. Allen (1990) Tidal straining, density currents and stirring in the control of estuarine circulation, *Estuaries*, **13**, 125-132

Simpson, J.H., W.R. Crawford, T.P. Rippeth, A.R. Campbell and J.V.S. Cheok (1996) The vertical structure of turbulent dissipation in shelf seas, *Journal of Physical Oceanography*, **26**, 1579-1590

Simpson, J.H., T.P. Rippeth and A.R. Campbell (2000) The phase lag of turbulent dissipation in tidal flow, *Interactions between Estuaries, Coastal Seas and Shelf Seas*, T. Yanagi (ed.), Terra Scientific Publishing Company, Tokyo, pp 57-67

Simpson J.H., R.Vennell and A.J. Souza (2001) The salt fluxes in a tidally-energetic estuary, *Estuarine Coastal and Shelf Science* **52,** 131-142

Smith, S.D. (1980) Wind stress and heat flux over the ocean in gale-force winds, *Journal of Physical Oceanography*, **10**, 709-726

Soulsby, R.L. (1980) Selecting record lengths and digitization rate for near-bed turbulence measurements, *Journal of Physical Oceanography*, **10**, 208-219

Soulsby, R.L. (1983) The bottom boundary layer of shelf seas, *Physical Oceanography of Coastal and Shelf Seas*, B. Johns (ed.), Elsevier Oceanography Series, Vol. 35, Elsevier, Amsterdam, pp189-266

Stacey, M.T., S.G. Monismith and J.R. Burau (1999a) Measurements of Reynolds stress profiles in unstratified tidal flow, *Journal of Geophysical Research*, **104**, 10933-10949

Stacey, M.T., S.G. Monismith and J.R. Burau (1999b) Observations of turbulence in a partially stratified estuary, *Journal of Physical Oceanography*, **29**, 1950-1970

Stacey, M.T., J.R. Burau and S.G. Monismith (2001) Creation of residual flows in a partially stratified estuary, *Journal of Geophysical Research*, **106**, 17013-17037

Sutton, O.G. (1953) *Micrometeorology*, McGraw-Hill Book Company, Inc., New York, 333pp.

Taylor, G.I. (1931) Effect of variation in density on the stability of superposed streams of fluid, *Proceedings of the Royal Society, A,* **132**, 499-523, Reprinted in G.K. Batchelor (ed.) *The Scientific Papers of G.I. Taylor, Volume 2: Meteorology, Oceanography and Turbulent Flow* (1960), Cambridge University Press, pp. 219-239

Taylor, G.I. (1935) Statistical theory of turbulence, Part 1, *Proceedings of the Royal Society, A,* **151**, 421-444, Reprinted in G.K. Batchelor (ed.) *The Scientific Papers of G.I. Taylor, Volume 2: Meteorology, Oceanography and Turbulent Flow* (1960), Cambridge University Press, pp. 288-306

Tennekes, H. and J.L. Lumley (1972) *A First Course in Turbulence*, The MIT Press, Cambridge, Massachusetts, 300 pp.

Tritton, D.J. (1977) *Physical Fluid Dynamics*, Van Nostrand Reinhold, England, 362pp.

Tropea, C., (1983) A note concerning the use of a one-component LDA to measure shear stress terms, *Experiments In Fluids I*, **10**, 209-210

Trowbridge, J.H. (1998) On a technique for measurement of turbulent shear stress in the presence of surface waves, *Journal of Atmospheric and Oceanic Technology*, **15**, 290-298

Trowbridge, J.H., W.R. Geyer, M.M. Bowen and A.J. Williams III (1999) Near-bottom turbulence measurements in a partially mixed estuary: turbulent energy balance, velocity structure and along-channel momentum balance, *Journal of Physical Oceanography*, **29**, 3056-3072

Turner, J.S. (1973) *Buoyancy effects in fluids*, Cambridge University Press, England, 368pp.

Uncles, R.J. (2002) Estuarine Physical Processes Research: Some Recent Studies and Progress, *Estuarine, Coastal and Shelf Science*, **55**, 829-856

van Haren, H., N. Oakey and C. Garrett (1994), Measurements of internal wave band eddy fluxes above a sloping bottom, *Journal of Marine Research*, **52**, 909-946

Vincent, R.A. and I.M. Reid (1983) HF Doppler measurements of mesospheric gravity wave momentum fluxes, *Journal of the Atmospheric Sciences*, **40**, 1321-1333

Visbeck, M. and J. Fischer (1995) Sea surface conditions remotely sensed by upward-looking ADCPs, *Journal of Atmospheric and Oceanic Technology*, **12**, 141-149

Voulgaris, G. and J.H. Trowbridge (1998) Evaluation of the Acoustic Doppler Velocimeter (ADV) for Turbulence Measurements, *Journal of Atmospheric and Oceanic Technology*, **15**, 272-289

Wang, S.L., C.T.A. Chen, G.H. Hong and C.S. Chung (2000) Carbon Dioxide and related parameters in the East China Sea, *Continental Shelf Research*, **20**, 525-544

Williams, E. and J.H. Simpson (2004) Uncertainties in estimates of Reynolds stress and TKE production rate using the ADCP variance method, *Journal of Atmospheric and Oceanic Technology*, **21**, 347-357

Appendix 1: Derivation of the Turbulent Kinetic Energy (TKE) equation

This derivation is included, since a straightforward derivation which includes buoyancy effects was not readily found in the available literature.

The continuity equation is:

$$\frac{\partial \rho}{\partial t} + \frac{\partial (\rho u_i)}{\partial x_i} = 0 \tag{1}$$

For a fluid which has a constant density over the averaging period, this simplifies to:

$$\frac{\partial u_i}{\partial x_i} = 0 \tag{2}$$

The Navier-Stokes equation, neglecting rotational effects is:

$$\rho\left(\frac{\partial u_i}{\partial t} + u_j \frac{\partial u_i}{\partial x_j}\right) = -\frac{\partial p}{\partial x_i} - \rho g \delta_{i3} + \mu \frac{\partial^2 u_i}{\partial x_j \partial x_j} \tag{3}$$

where u_i is the velocity vector, p is the pressure, μ is the molecular viscosity of the fluid and δ_{ij} is the Kronecker delta: $\delta_{ij} = 1$ for $i = j$; $\delta_{ij} = 0$ for i ≠ j.

The left hand side of equation (3) represents the momentum change of the fluid. The first term on the right hand side is a pressure term, the second term represents changes due to external forces (gravitational or buoyancy effects) and the third represents the viscous forces. The following derivation, up as far as equation (9) follows that of Tritton (1977), but includes the buoyancy term, which he neglects. The buoyancy term is important in this study since density effects play a part in both main study sites.

Each velocity can be separated into a mean and fluctuating part, using the Reynolds decomposition, in which the mean is calculated over some time interval. So the velocities can be written: $u_i = \overline{u}_i + u_i'$, where $u_i, \overline{u}_i, u_i'$ are the total, mean and fluctuating velocities in the x_i direction. Decomposing the velocity, pressure and density into a mean and fluctuating part, and dividing by a reference density ρ_0:

$$\frac{(\overline{\rho}+\rho')}{\rho_0}\left(\frac{\partial(\overline{u}_i+u_i')}{\partial t}+(\overline{u}_j+u_j')\frac{\partial}{\partial x_j}(\overline{u}_i+u_i')\right)$$

$$=-\frac{1}{\rho_0}\frac{\partial}{\partial x_i}(\overline{p}+p')-\delta_{i3}(\overline{\rho}+\rho')\frac{g}{\rho_0}+\nu\frac{\partial^2}{\partial x_j\partial x_j}(\overline{u}_i+u_i') \qquad (4)$$

where $\nu=\frac{\mu}{\rho_0}=$ kinematic molecular viscosity.

Applying the Boussinesq approximation, which states that small density fluctuations can be neglected in terms of their effect on inertia but variations in the weight (or buoyancy) of the fluid may be important (Phillips, 1966), gives:

$$\frac{\partial(\overline{u}_i+u_i')}{\partial t}+(\overline{u}_j+u_j')\frac{\partial}{\partial x_j}(\overline{u}_i+u_i')$$

$$=-\frac{1}{\rho_0}\frac{\partial}{\partial x_i}(\overline{p}+p')-\delta_{i3}(\overline{\rho}+\rho')\frac{g}{\rho_0}+\nu\frac{\partial^2}{\partial x_j\partial x_j}(\overline{u}_i+u_i') \qquad (5)$$

Taking a time average of (5) gives:

$$\frac{\partial\overline{u}_i}{\partial t}+\overline{u}_j\frac{\partial\overline{u}_i}{\partial x_j}+\overline{u_j'\frac{\partial u_i'}{\partial x_j}}=-\frac{1}{\rho_0}\frac{\partial\overline{p}}{\partial x_i}-\frac{\overline{\rho}}{\rho_0}g\delta_{i3}+\nu\frac{\partial^2\overline{u}_i}{\partial x_j\partial x_j} \qquad (6)$$

Equation (6) can also be written, taking the third term on the left hand side over to the right hand side and applying the continuity equation (2):

$$\frac{\partial\overline{u}_i}{\partial t}+\overline{u}_j\frac{\partial\overline{u}_i}{\partial x_j}=-\frac{1}{\rho_0}\frac{\partial\overline{p}}{\partial x_i}-\frac{\overline{\rho}}{\rho_0}g\delta_{i3}+\nu\frac{\partial^2\overline{u}_i}{\partial x_j\partial x_j}-\frac{\partial\overline{u_i'u_j'}}{\partial x_j} \qquad (7)$$

A non-zero value of the time average of the product of the two fluctuations $\overline{u_i'u_j'}$, contained in the last term of equation (7), implies a correlation between them. If the correlations are multiplied by the density of the fluid, ρ, it is apparent that in physical terms they represent a momentum flux: the rate at which momentum is exchanged from one layer of fluid to the adjacent layer. Using a dimensional argument, the dimensions of the terms $-\rho\overline{u_i'u_j'}$ are $\frac{M}{L^3}\frac{L^2}{T^2}=\frac{M}{LT^2}$. These are the dimensions of a stress (force per unit area), so the physical behaviour of these terms is that of a stress,

called the Reynolds stress. The term $\overline{u_i' u_j'}$ therefore represents a frictional stress on the mean flow which is present in turbulent flow, and augments the viscous stress.

Subtracting (6) from (5) and multiplying by u_i' gives:

$$u_i' \frac{\partial u_i'}{\partial t} + u_i' \overline{u}_j \frac{\partial u_i'}{\partial x_j} + u_i' u_j' \frac{\partial \overline{u}_i}{\partial x_j} + u_i' u_j' \frac{\partial u_i'}{\partial x_j} - u_i' \overline{u_j' \frac{\partial u_i'}{\partial x_j}} = -\frac{u_i'}{\rho_0} \frac{\partial p'}{\partial x_i} - \frac{\rho'}{\rho_0} u_3' g + \nu u_i' \frac{\partial^2 u_i'}{\partial x_j \partial x_j} \tag{8}$$

Note that the buoyancy term is only non-zero for $i = 3$.

Taking a time average:

$$\frac{1}{2}\frac{\partial \left(\overline{u_i'^2}\right)}{\partial t} + \frac{1}{2}\overline{u}_j \frac{\partial \left(\overline{u_i'^2}\right)}{\partial x_j} + \overline{u_i' u_j'} \frac{\partial \overline{u}_i}{\partial x_j} + \frac{1}{2}\frac{\partial \left(\overline{u_i'^2 u_j'}\right)}{\partial x_j} = -\frac{1}{\rho_0}\frac{\partial \left(\overline{p' u_i'}\right)}{\partial x_i} - \frac{\overline{\rho' u'}_3}{\rho_0} g + \nu \overline{u_i' \frac{\partial^2 u_i'}{\partial x_j \partial x_j}} \tag{9}$$

The final term can be decomposed as follows (Raudkivi and Callander, 1975):

$$\begin{aligned}
\overline{u_i' \frac{\partial^2 u_i'}{\partial x_j \partial x_j}} &= \overline{u_i' \frac{\partial^2 u_i'}{\partial x_j \partial x_j}} + \overline{u_i' \frac{\partial}{\partial x_i}\left(\frac{\partial u_j'}{\partial x_j}\right)} \quad \left(\text{since } \overline{\frac{\partial u_j'}{\partial x_j}} = 0 \text{ from (2)}\right) \\
&= \overline{u_i' \frac{\partial^2 u_i'}{\partial x_j \partial x_j}} + \overline{u_i' \frac{\partial}{\partial x_j}\left(\frac{\partial u_j'}{\partial x_i}\right)} \\
&= \overline{\frac{\partial}{\partial x_j}\left(u_i' \frac{\partial u_i'}{\partial x_j}\right)} - \overline{\left(\frac{\partial u_i'}{\partial x_j}\right)^2} + \overline{\frac{\partial}{\partial x_j}\left(u_i' \frac{\partial u_j'}{\partial x_i}\right)} - \overline{\frac{\partial u_i'}{\partial x_j}\frac{\partial u_j'}{\partial x_i}} \\
&= \overline{\frac{\partial}{\partial x_j}\left(u_i'\left(\frac{\partial u_i'}{\partial x_j} + \frac{\partial u_j'}{\partial x_i}\right)\right)} - \overline{\frac{\partial u_i'}{\partial x_j}\left(\frac{\partial u_j'}{\partial x_i} + \frac{\partial u_i'}{\partial x_j}\right)}
\end{aligned} \tag{10}$$

The turbulent kinetic energy per unit mass is $\overline{q^2}/2 = \overline{u_i' u_i'}/2 = \overline{u_i'^2}/2$, so $\overline{u_i'^2}$ can be replaced by $\overline{q^2}$. Hence (9) becomes:

$$\begin{aligned}
&\frac{1}{2}\frac{\partial \left(\overline{q^2}\right)}{\partial t} + \frac{1}{2}\overline{u}_i \frac{\partial \left(\overline{q^2}\right)}{\partial x_i} \\
&= -\frac{\partial}{\partial x_i}\frac{\overline{u_i' p'}}{\rho_0} - \frac{\partial}{\partial x_i}\frac{\overline{u_i' q^2}}{2} + \nu \overline{\frac{\partial}{\partial x_j}\left(u_i'\left(\frac{\partial u_i'}{\partial x_j} + \frac{\partial u_j'}{\partial x_i}\right)\right)} - \overline{u_i' u_j'}\frac{\partial \overline{u}_j}{\partial x_i} - \frac{\overline{\rho' u'}_3}{\rho_0} g - \nu \overline{\frac{\partial u_i'}{\partial x_j}\left(\frac{\partial u_j'}{\partial x_i} + \frac{\partial u_i'}{\partial x_j}\right)}
\end{aligned} \tag{11}$$

The first three terms on the right hand side represent the advection or transport of energy. The first two represent the transport by the turbulence itself, while the third term represents the transfer of energy by viscous stresses and is usually small compared to the other terms (Kundu,1990). The transfer terms all become zero when integrated over the whole flow (Tritton, 1977). The fourth term on the right hand side represents the rate at which kinetic energy is transferred from the mean flow to the turbulence, that is, the rate of production of TKE by the action of shear stresses on the shear in the mean flow. In isotropic turbulence, the mean value of the correlation $-\overline{u_i' u_j'}$ is zero, since a positive value of u_i' may be associated with either a positive or negative value of u_j' (Kundu, 1990). Therefore turbulence is always anisotropic at the production scales. The fifth term represents the production or destruction of TKE due to buoyancy effects: convection and mixing. The last term on the right hand side represents the viscous dissipation of energy to heat.

At the small dissipation scales, it is assumed that the turbulence is very nearly isotropic; although true isotropic turbulence cannot exist in real flows (Hinze, 1959). The dissipation term can be written:

$$\varepsilon = \overline{\left(\frac{\partial u_i'}{\partial x_j} \frac{\partial u_j'}{\partial x_i} + \left(\frac{\partial u_i'}{\partial x_j} \right)^2 \right)} \tag{12}$$

It can be shown that the first term on the right hand side of equation (12) is zero in isotropic turbulence, (Raudkivi and Callander, 1975):

$$\frac{\partial^2 \left(\overline{u_i' u_j'} \right)}{\partial x_i \partial x_j} = \frac{\partial}{\partial x_i} \left(\frac{\partial \left(\overline{u_i' u_j'} \right)}{\partial x_j} \right) = \frac{\partial}{\partial x_i} \left(\overline{u_i' \frac{\partial u_j'}{\partial x_j}} + \overline{u_j' \frac{\partial u_i'}{\partial x_j}} \right) = \frac{\partial}{\partial x_i} \left(\overline{u_j' \frac{\partial u_i'}{\partial x_j}} \right)$$

$$\frac{\partial}{\partial x_i} \left(\overline{u_j' \frac{\partial u_i'}{\partial x_j}} \right) = \overline{u_j' \frac{\partial^2 u_i'}{\partial x_i \partial x_j}} + \overline{\frac{\partial u_i'}{\partial x_j} \frac{\partial u_j'}{\partial x_i}} = \overline{\frac{\partial u_i'}{\partial x_j} \frac{\partial u_j'}{\partial x_i}}$$

Hence, since $\frac{\partial^2 \left(\overline{u_i' u_j'} \right)}{\partial x_i \partial x_j} = 0$ in isotropic turbulence, $\overline{\frac{\partial u_i'}{\partial x_j} \frac{\partial u_j'}{\partial x_i}} = 0$.

This results in the simplified form for ε in isotropic turbulence:

$$\varepsilon = \nu \overline{\left(\frac{\partial u_i'}{\partial x_j} \right)^2} \tag{13}$$

In this study, transport effects are assumed negligible, and so the simplified form of the turbulent kinetic energy equation will be used:

$$\frac{1}{2} \frac{\partial \left(\overline{q^2} \right)}{\partial t} = -\overline{u_i' u_j'} \frac{\partial \overline{u}_j}{\partial x_i} - \frac{\overline{\rho' u'}_3}{\overline{\rho}} g - \nu \overline{\left(\frac{\partial u_i'}{\partial x_j} \right)^2} \tag{14}$$

Appendix 2: Uncertainties in velocity estimates

(This appendix consists of a summary from RDI, 1996)

The WorkHorse Broadband ADCP manufactured by RD Instruments uses an autocorrelation method to determine the Doppler shift. This involves the comparison of the return signal of a pulse to itself at a later time, which allows calculation of the frequency of the return pulse.

Thus:

$$F_D = \frac{2VF_0}{C} = \frac{\psi}{2\pi T_L} \tag{15}$$

where: F_D = Doppler shifted frequency; F_0 = frequency of transmitted signal; V = velocity of reflectors; C = speed of sound; ψ = phase shift over time T_L

Hence the velocity and standard deviation of the reflectors are given by:

$$V = \frac{\psi\ C}{4\pi F_0 T_L} \tag{16}$$

$$\sigma_N = \frac{\sigma_\psi\ C}{4\pi F_0 T_L} \tag{17}$$

The lower bound of phase variance is given by (RDI, 1996):

$$\sigma_\psi{}^2 = \frac{R^{-2} - 1}{2} \tag{18}$$

where R = correlation at lag T_L

Hence:

$$\sigma_N = \frac{\left(R^{-2} - 1\right)^{\frac{1}{2}} C}{\sqrt{2}\left(4\pi F_0 T_L\right)} \tag{19}$$

The ambiguity velocity V_a is defined as the velocity at which $\psi = \pi$, so setting $\psi = \pi$ in (16) gives:

$$V_a = \frac{C}{4F_0T_L} \tag{20}$$

and (19) becomes:

$$\sigma_N = \frac{\left(R^{-2}-1\right)^{\frac{1}{2}}V_a}{\sqrt{2\pi}} \tag{21}$$

The number of independent measurements in a depth cell is:

$$m = \frac{D}{T_P} \tag{22}$$

where D = depth cell length; T_P = pulse length, defined by: $T_P = 2C\cos\theta/F_0$; and θ = inclination of beams with the vertical

The standard deviation is reduced in proportion to the square root of the number of independent measurements, hence (21) becomes:

$$\sigma_N = \frac{\left(R^{-2}-1\right)^{\frac{1}{2}}V_a}{\sqrt{2\pi}m^{\frac{1}{2}}} \tag{23}$$

Substituting in (23) for m and T_P gives:

$$\sigma_N = \frac{V_a}{\pi}\left(\frac{\left(R^{-2}-1\right)C\cos\theta}{DF_0}\right)^{\frac{1}{2}} \tag{24}$$

Hence the standard deviation of any velocity measurement can be calculated. The method by which the parameter R is calculated is not disclosed by RDI, but the horizontal standard deviation of the velocity measurements can be obtained from a table of values supplied by RDI. A relationship between the horizontal and along-beam standard deviations can be obtained using equation (24) and the formula for the calculation of the horizontal standard deviation:

$$\sigma_H = \frac{1.5V_a\left(R^{-2}-1\right)^{\frac{1}{2}}}{2m^{\frac{1}{2}}\pi\sin\theta} = \frac{1.5V_a}{2\pi\sin\theta}\left(\frac{\left(R^{-2}-1\right)2C\cos\theta}{DF_0}\right)^{\frac{1}{2}} \tag{25}$$

This is simply equation (24) corrected for a system of 2 beams inclined at an angle of θ to the vertical. It includes an empirically determined correction factor of 1.5 which arises from limitations of the signal processing and the non-independence of the code element measurements. This correction factor should also be included in equation (24) for the along-beam standard deviation.

Hence:

$$\frac{\sigma_N}{\sigma_H} = \sqrt{2}\sin\theta \qquad (26)$$

This ratio has a value of 0.484 for an ADCP in which the beams are inclined at an angle of 20° to the vertical.

Appendix 3: Error analysis for Reynolds stress estimates

The error in an individual ADCP estimate of velocity is considered to be Gaussian white noise (Stacey *et al.*, 1999a). The measured signal from beam i can be denoted by:

$$b_i = \chi_i + b_N \tag{27}$$

where b_N is Gaussian white noise and χ_i is the actual velocity along beam i.

The mean velocity $\overline{\chi}_i$ along beam i using M samples over the averaging period for means and variances is estimated as:

$$\overline{\chi}_{i(est)} = \overline{b}_i = \frac{1}{M}\sum_{m=1}^{M} b_i(m) \tag{28}$$

and the variance along beam i, $\overline{\chi_i'^2}$, is estimated as:

$$\overline{\chi_i'^2}_{(est)} = \overline{b_i'^2} = \frac{1}{M}\sum_{m=1}^{M} b_i'^2(m) = \frac{1}{M}\sum_{m=1}^{M}\left(b_i(m) - \overline{b}_i\right)^2 \tag{29}$$

Hence the estimator of the Reynolds stress becomes:

$$\overline{u'w'}_{(est)} = \frac{1}{4\cos\theta\sin\theta}\left[\overline{b_1'^2} - \overline{b_2'^2}\right] \tag{30}$$

(using a right-handed co-ordinate system and an upward-looking ADCP)

Stacey *et al.* (1999a) show that the estimator of the Reynolds stress is unbiased by the Doppler noise, since:

$$E\left(\overline{u'w'}\right)_{(est)} = \frac{1}{4\cos\theta\sin\theta}\left[\left(\overline{\chi_1'^2}\right) - \left(\overline{\chi_2'^2}\right)\right] = \overline{u'w'} \tag{31}$$

The variance of the estimate of Reynolds stress is given by (Stacey *et al.*, 1999a):

$$Var\left(\overline{u'w'}\right)_{(est)} = \frac{1}{16\sin^2\theta\cos^2\theta}\left[Var\left(\overline{b_1'^2}\right) + Var\left(\overline{b_2'^2}\right) - 2Cov\left(\overline{b_1'^2}, \overline{b_2'^2}\right)\right] \tag{32}$$

This simplifies to:

$$Var\left(\overline{u'w'}\right)_{(est)} = \frac{1}{8\sin^2\theta\cos^2\theta} Var\left(\overline{b_i'^2}\right) \tag{33}$$

if it is assumed that the noise variance is the same in all beams and the covariance is negligible. This has been found to be the case (Stacey *et al.*, 1999a); all beams were

shown to have similar noise characteristics and turbulence statistics and the covariance between beams was more than an order of magnitude smaller than the variance of individual beams.

The value of $Var\left(\overline{b_i'^2}\right)$ is estimated using equation (29) as follows:

$$\begin{aligned} Var\left(\overline{b_i'^2}\right) &= Var\left(\frac{1}{M}\sum_{m=1}^{M} b_i'^2(m)\right) \\ &= \frac{1}{M^2} Var \sum_{m=1}^{M} b_i'^2(m) \\ &= \frac{1}{M^2}\sum_{m=1}^{M} Var\left(b_i'^2(m)\right) \\ &= \frac{1}{M} Var\left(b_i'^2\right) \end{aligned} \tag{34}$$

Hence (33) becomes:

$$Var\left(\overline{u'w'}\right)_{(est)} = \frac{1}{8M\sin^2\theta\cos^2\theta} Var\left(b_i'^2\right) \tag{35}$$

The variance of the square of the along-beam velocity fluctuations is given by:

$$\begin{aligned} Var\left(b_i'^2\right) &= \frac{1}{M}\sum_{1}^{M}\left(b_i'^2 - \overline{b_i'^2}\right)^2 \\ &= \frac{1}{M}\sum_{1}^{M} b_i'^4 - \frac{2}{M}\sum_{1}^{M} b_i'^2\overline{b_i'^2} + \frac{1}{M}\sum_{1}^{M}\left(\overline{b_i'^2}\right)^2 \\ &= \mu_4 - \frac{2}{M} M\left(\overline{b_i'^2}\right)^2 + \left(\overline{b_i'^2}\right)^2 \\ &= \mu_4 - {\mu_2}^2 \end{aligned} \tag{36}$$

where μ_2 and μ_4 are the second and fourth moments respectively. The second moment is the variance of the quantity under consideration (i.e. $\overline{b_i'^2}$); the fourth moment of a variable x is defined as:

$$\mu_4 = \frac{1}{M}\sum_{r=1}^{M}(x_r - \bar{x})^4 = \frac{1}{M}\sum_{r=1}^{M} {x_r}^4 \quad \text{for } \bar{x} = 0 \tag{37}$$

For a Gaussian distribution, $\mu_4 = 3\mu_2^{\ 2}$ and equation (36) becomes:

$$Var\left(b_i'^2\right) = 2\mu_2^{\ 2} \tag{38}$$

Hence, substituting in equation (34):

$$Var\left(\overline{b_i'^2}\right) = \frac{2\mu_2^{\ 2}}{M} \tag{39}$$

Therefore equation (33) can be written:

$$Var\left(\overline{u'w'}\right)_{(est)} = \frac{\mu_2^{\ 2}}{4M\sin^2\theta\cos^2\theta} = \frac{\mu_2^{\ 2}}{M\sin^2 2\theta} \tag{40}$$

Using a value for the autocorrelation function of 3 as before, the variance in the Reynolds stress estimates can be written:

$$Var\left(\overline{u'w'}\right)_{(est)} = \frac{3}{M\sin^2 2\theta}\left(\overline{b_i'^2}\right)^2 \tag{41}$$

In order to reduce the error in the Reynolds stress estimates, the ping rate can be increased. If the true value of the Reynolds stress is zero, then the noise in the stress estimate is given by equation (41):

$$Var\left(\overline{u'w'}\right) = \frac{3}{M\sin^2 2\theta}\left(\sigma_N^{\ 2}\right)^2 \tag{42}$$

If the ping rate is increased by a factor n, whilst still averaging over the same period for the Reynolds stress estimates, the error becomes:

$$Var\left(\overline{u'w'}\right) = \frac{3}{Mn\sin^2 2\theta}\left(\sigma_N^{\ 2}\right)^2 \tag{43}$$

If initial averaging is done of the n pings, before calculating the Reynolds stresses, then the noise in the velocity measurements is reduced by a factor of n. Hence:

$$Var\left(\overline{u'w'}\right) = \frac{3}{M\sin^2 2\theta}\left(\frac{\sigma_N^{\ 2}}{n}\right)^2 \tag{44}$$

Thus by increasing the ping rate by a factor of n, the variance in the Reynolds stress estimates is decreased by the same factor. For minimum noise, the ensemble time should be no greater than the auto-correlation time scale of the turbulence, with the maximum possible number of pings averaged over that time period.

Appendix 4: The variance of the Reynolds stress estimates

From equation (32) in Appendix 3, the variance of the Reynolds stress is:

$$\sigma_R^{\,2} = \frac{1}{16\sin^2\theta\cos^2\theta} Var\left(\frac{1}{M}\sum_{m=1}^{M} b_2'^2(m) - \frac{1}{M}\sum_{m=1}^{M} b_1'^2(m)\right)$$

$$= \frac{1}{16M^2\sin^2\theta\cos^2\theta} Var\left(\sum_{m=1}^{M} b_2'^2(m) - \sum_{m=1}^{M} b_1'^2(m)\right)$$

Writing in a covariance form:

$$\sigma_R^{\,2} = \frac{1}{16M^2\sin^2\theta\cos^2\theta}\left[Cov\left(\left(\sum_{m=1}^{M} b_2'^2(m) - \sum_{m=1}^{M} b_1'^2(m)\right),\left(\sum_{m=1}^{M} b_2'^2(m) - \sum_{m=1}^{M} b_1'^2(m)\right)\right)\right]$$

Using the additive rule for covariances:

$$\sigma_R^{\,2} = \frac{\sum_{m=1}^{M}\sum_{n=1}^{M}\left[Cov\left(b_1'^2(m), b_1'^2(n)\right) + Cov\left(b_2'^2(m), b_2'^2(n)\right) - 2Cov\left(b_1'^2(m), b_2'^2(n)\right)\right]}{16M^2\sin^2\theta\cos^2\theta}$$

Rearranging into variances and covariances:

$$\sigma_R^{\,2} = \frac{\sum_{i=1}^{2}\sum_{m=1}^{M} Var\left(b_i'^2(m)\right) + 2\sum_{i=1}^{2}\sum_{m=1}^{M-1}\sum_{n=m+1}^{M} Cov\left(b_i'^2(m), b_i'^2(n)\right) - 2\sum_{m=1}^{M}\sum_{n=1}^{M} Cov\left(b_1'^2(m), b_2'^2(n)\right)}{16M^2\sin^2\theta\cos^2\theta}$$

Appendix 5: The variance of a product

The variance of a product xy is derived as follows (Mood *et al*, 1974):

$$Var(xy) = E\left[(xy)^2\right] - [E(xy)]^2$$

The mean value of the product, $E(xy)$ is given by:

$$E(xy) = \bar{x}\ \bar{y} + Cov(x, y)$$

Squaring this, we get:

$$[E(xy)]^2 = \bar{x}^2\bar{y}^2 + 2\bar{x}\ \bar{y}Cov(x, y) + [Cov(x, y)]^2$$

The mean value of the product squared is given by:

$$E\left[(xy)^2\right] = E\left[(x' + \bar{x})^2(y' + \bar{y})^2\right]$$

Expanding:

$$E\left[(xy)^2\right] = E\left(x'^2y'^2\right) + \bar{y}^2Var(x) + \bar{x}^2Var(y) + \bar{x}^2\bar{y}^2 + 2\bar{y}\left(\overline{x'^2y'}\right) + 2\bar{x}\left(\overline{x'y'^2}\right) + 4\bar{x}\ \bar{y}Cov(x, y)$$

Hence:

$$Var(xy) = \bar{y}^2Var(x) + \bar{x}^2Var(y) + E\left(x'^2y'^2\right) - [Cov(x, y)]^2 + 2\bar{x}\ \bar{y}Cov(x, y) + 2\bar{y}\left(\overline{x'^2y'}\right) + 2\bar{x}\left(\overline{x'y'^2}\right)$$

If x and y are independent, then only the first three terms are non-zero and:

$$Var(xy) = \bar{y}^2Var(x) + \bar{x}^2Var(y) + Var(x)Var(y)$$

For two variables which are not independent, but have zero mean, only the third and fourth terms remain:

$$Var(xy) = E\left(x'^2y'^2\right) - [Cov(x, y)]^2$$

The two parameters of interest, $-\overline{u'w'}$ and $\partial u/\partial z$, are calculated from the velocities in different depth cells of the ADCP, so in the case of the ADCP noise levels at zero flow, these two quantities are expected to be uncorrelated, so we can use the simplified equation using the variances to estimate the uncertainty due to instrument noise:

$$Var(xy) = Var(x)Var(y).$$

Using the product of the variances as an estimator of $E\left(x'^2 y'^2\right)$ will tend to underestimate the value of $E\left(x'^2 y'^2\right)$ if the two quantities are not independent. However, for two strongly correlated quantities, the covariance term $[Cov(xy)]^2$ is of the same order as the product of the variances which will counteract this effect by reducing the estimate of $Var(xy)$.

Appendix 6: Errors due to tilt in the ADCP

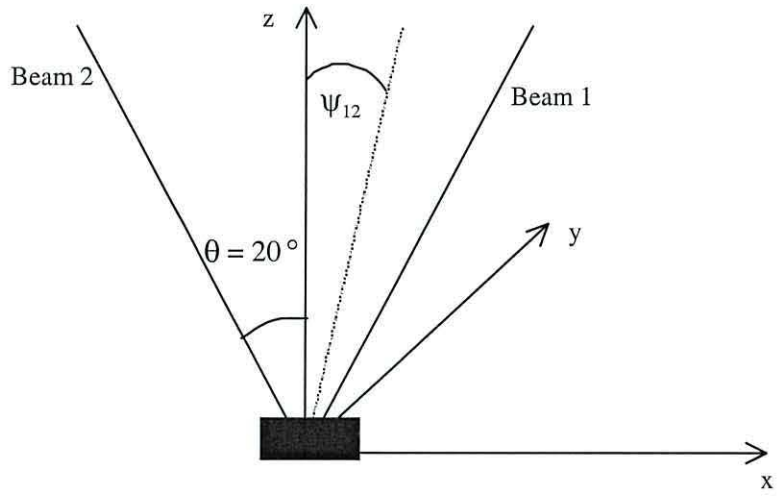

Figure A1: Schematic of ADCP showing tilt angle ψ_{12}. The positive y-axis is into the page.

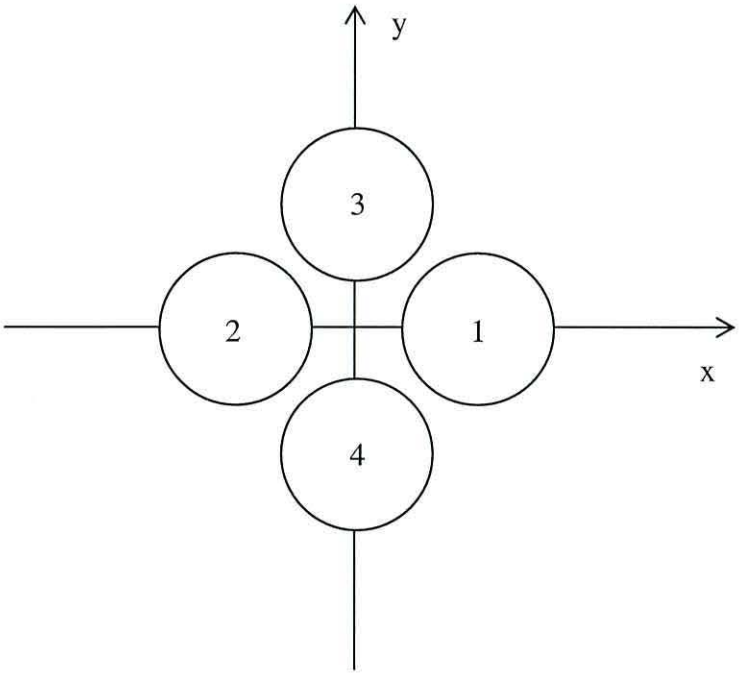

Figure A2: Beam configuration in ADCP head. Pitch (ψ_{34}) is tilt in the plane of beams 3 and 4; roll (ψ_{12}) is tilt in the plane of beams 1 and 2. Pitch is positive for anticlockwise rotation about the x-axis (the 1-2 axis), i.e. when beam 3 is higher than beam 4. Roll is positive for anticlockwise rotation about the y-axis (the 3-4 axis), i.e. when beam 2 is higher than beam 1.

Using a right-handed co-ordinate system, with positive rotations defined as in an anti-clockwise direction, as shown in Figure 1, the transformation matrix can be defined. We start with the transformation from a fixed system to a tilted system. First rotate an angle ψ_{12} about the y-axis. This is denoted by the following transformation matrix:

$$Y = \begin{pmatrix} \cos\psi_{12} & 0 & -\sin\psi_{12} \\ 0 & 1 & 0 \\ \sin\psi_{12} & 0 & \cos\psi_{12} \end{pmatrix} \tag{45}$$

Then rotate an angle ψ_{34} about the tilted x-axis:

$$X = \begin{pmatrix} 1 & 0 & 0 \\ 0 & \cos\psi_{34} & \sin\psi_{34} \\ 0 & -\sin\psi_{34} & \cos\psi_{34} \end{pmatrix} \tag{46}$$

The angle ψ_{34} is defined by:

$$\sin\psi_{34} = \frac{\sin\psi'_{34}}{\cos\psi_{12}} \tag{47}$$

where ψ'_{34} = rotation about the fixed x-axis (in beam 3-4 plane; ADCP pitch)

For small tilt angles, $\cos\psi_{12} \approx 1$ and $\psi'_{34} \approx \psi_{34}$.

Combining these transformations gives:

$$A = XY = \begin{pmatrix} \cos\psi_{12} & 0 & -\sin\psi_{12} \\ \sin\psi_{12}\sin\psi_{34} & \cos\psi_{34} & \cos\psi_{12}\sin\psi_{34} \\ \sin\psi_{12}\cos\psi_{34} & -\sin\psi_{34} & \cos\psi_{12}\cos\psi_{34} \end{pmatrix} \tag{48}$$

This matrix can be simplified if it is assumed that for small tilt angles, that is, less than about 0.014 radians (~8°), $\sin\psi_{12} \approx \psi_{12}$ radians, $\sin\psi_{34} \approx \psi_{34}$ radians and $\cos\psi_{12} \approx \cos\psi_{34} \approx 1$. Also, $\sin\psi_{12}\sin\psi_{34} \approx 0$.

$$A=\begin{pmatrix} 1 & 0 & -\psi_{12} \\ 0 & 1 & \psi_{34} \\ \psi_{12} & -\psi_{34} & 1 \end{pmatrix} \tag{49}$$

The velocity vectors (u_i, v_i, w_i) at any point along beam i can be rotated using matrix A into orthogonal components in the tilted co-ordinate system (u_{iT}, v_{iT}, w_{iT}):

$$\begin{pmatrix} u_{iT} \\ v_{iT} \\ w_{iT} \end{pmatrix}=\begin{pmatrix} 1 & 0 & -\psi_{12} \\ 0 & 1 & \psi_{34} \\ \psi_{12} & -\psi_{34} & 1 \end{pmatrix}\begin{pmatrix} u_i \\ v_i \\ w_i \end{pmatrix}=\begin{pmatrix} u_i-\psi_{12}w_i \\ v_i+\psi_{34}w_i \\ \psi_{12}u_i-\psi_{34}v_i+w_i \end{pmatrix} \tag{50}$$

The measured along beam velocities in the tilted system in terms of the velocity vectors in the tilted system are:

$$b_1=-u_{1T}\sin\theta-w_{1T}\cos\theta$$
$$b_2=u_{2T}\sin\theta-w_{2T}\cos\theta$$
$$b_3=-v_{3T}\sin\theta-w_{3T}\cos\theta$$
$$b_4=v_{4T}\sin\theta-w_{4T}\cos\theta \tag{51}$$

Writing these in terms of the velocity components in the fixed co-ordinate system by substitution of the relationships given in equation (50) in to equation (51):

$$b_1=u_1\left(-\sin\theta-\psi_{12}\cos\theta\right)+v_1\psi_{34}\cos\theta+w_1\left(\psi_{12}\sin\theta-\cos\theta\right)$$
$$b_2=u_2\left(\sin\theta-\psi_{12}\cos\theta\right)+v_2\psi_{34}\cos\theta+w_2\left(-\psi_{12}\sin\theta-\cos\theta\right)$$
$$b_3=-u_3\psi_{12}\cos\theta+v_3\left(-\sin\theta+\psi_{34}\cos\theta\right)+w_3\left(-\psi_{34}\sin\theta-\cos\theta\right)$$
$$b_4=-u_4\psi_{12}\cos\theta+v_4\left(\sin\theta+\psi_{34}\cos\theta\right)+w_4\left(\psi_{34}\sin\theta-\cos\theta\right) \tag{52}$$

Similar equations are obtained for the along-beam velocity fluctuations, b_i', and their associated components u_i', v_i' and w_i'. Hence by squaring and subtracting pairs of equations, again ignoring terms involving the product of two small tilt angles, the equations for the Reynolds stresses can be written to include the errors due to tilt.

$$b_1^{\,2} = u_1^{\,2}\left(\sin^2\theta + 2\psi_{12}\sin\theta\cos\theta\right) + w_1^{\,2}\left(-2\psi_{12}\sin\theta\cos\theta + \cos^2\theta\right)$$
$$-2u_1v_1\psi_{34}\sin\theta\cos\theta + 2u_1w_1\left(\sin\theta\cos\theta - \psi_{12}\sin^2\theta + \psi_{12}\cos^2\theta\right) - 2v_1w_1\psi_{34}\cos^2\theta$$

$$b_2^{\,2} = u_2^{\,2}\left(\sin^2\theta - 2\psi_{12}\sin\theta\cos\theta\right) + w_2^{\,2}\left(2\psi_{12}\sin\theta\cos\theta + \cos^2\theta\right)$$
$$+2u_2v_2\psi_{34}\sin\theta\cos\theta + 2u_2w_2\left(-\sin\theta\cos\theta - \psi_{12}\sin^2\theta + \psi_{12}\cos^2\theta\right) - 2v_2w_2\psi_{34}\cos^2\theta$$

$$b_3^{\,2} = v_3^{\,2}\left(\sin^2\theta - 2\psi_{34}\sin\theta\cos\theta\right) + w_3^{\,2}\left(2\psi_{34}\sin\theta\cos\theta + \cos^2\theta\right)$$
$$+2u_3v_3\psi_{12}\sin\theta\cos\theta + 2u_3w_3\psi_{12}\cos^2\theta + 2v_3w_3\left(\sin\theta\cos\theta + \psi_{34}\sin^2\theta - \psi_{34}\cos^2\theta\right)$$

$$b_4^{\,2} = v_4^{\,2}\left(\sin^2\theta + 2\psi_{34}\sin\theta\cos\theta\right) + w_4^{\,2}\left(-2\psi_{34}\sin\theta\cos\theta + \cos^2\theta\right)$$
$$-2u_4v_4\psi_{12}\sin\theta\cos\theta + 2u_4w_4\psi_{12}\cos^2\theta + 2v_4w_4\left(-\sin\theta\cos\theta + \psi_{34}\sin^2\theta - \psi_{34}\cos^2\theta\right)$$

This produces the same result for errors in the Reynolds stress estimates as those given by Lu and Lueck (1999b) using the matrix given by Lohrmann *et al.* (1990). These are:

$$-\overline{u'w'} = \frac{\overline{b_2'^{\,2}} - \overline{b_1'^{\,2}}}{2\sin 2\theta} + \psi_{12}\left(\overline{u'^2} - \overline{w'^2}\right) - \psi_{34}\overline{u'v'}$$
$$-\overline{v'w'} = \frac{\overline{b_4'^{\,2}} - \overline{b_3'^{\,2}}}{2\sin 2\theta} - \psi_{34}\left(\overline{v'^2} - \overline{w'^2}\right) + \psi_{12}\overline{u'v'} \qquad (53)$$